

**Excited State Dynamics of Photoswitches: Molecular Motors, Photoacids and
Vitamin B₁₂**

by

Theodore E. Wiley

A dissertation submitted in partial fulfillment of
the requirements for the degree of
Doctor of Philosophy
(Chemistry)
in The University of Michigan
2017

Doctoral Committee:

Professor Roseanne J. Sension, Chair
Professor Eitan Geva
Professor Kevin J. Kubarych
Associate Professor Vanessa Sih

Theodore E. Wiley

tewiley@umich.edu

ORCID iD: 0000-0002-9765-2333

© Theodore E. Wiley 2017

To my wife and best friend McKenna, my mother Gail, and my father Hunt

ACKNOWLEDGEMENTS

Thank you McKenna. It's hard to say where I would be if we had not met, but I'm pretty sure I wouldn't have pursued a Ph.D. without you with me. You cheered me through the good times and the tough times and I'm grateful. You inspired me to become the best version of myself!

Thank you Mom and Dad. You taught me how to work hard, the value of earning what you have, and the value of education. Mom, I admire your devotion to teaching and education and you continue to inspire me to learn more and improve as a teacher. Dad, our conversations about biology and genetics got me thinking about science at a young age. Now that I'm older, I still get a kick out of the nerdy discussions we have. I love you guys. You're awesome!

Thank you Professor Roseanne Sension. Thank you for your strong support and willingness to let me try new things. Your high expectations pushed me out of my comfort zone often. But, when has a person ever improved while staying inside their comfort zone? Thank you for the opportunity to do research! Thank you Professor Ken Spears. I lucked out and got two advisers for the price of one!

Finally, thanks to my lab mates, friends, and collaborators: Dr. Brenden Arruda, Dr. Broc Smith, Nick Miller, Danielle Sofferman, Professor Yi Liao, Dr. Laura Kiefer, Dr. John King, Cody Aldaz, Dr. Shawn Eddy. I appreciate the friendly discussions, training and opportunity to train, and laughs we have shared.

This work was supported in part by grants from the National Science Foundation NSF-CHE 1150660 and NSF-CHE 1464584.

TABLE OF CONTENTS

DEDICATION.....	ii
ACKNOWLEDGEMENTS.....	iii
LIST OF FIGURES.....	vi
LIST OF TABLES.....	xvi
ABSTRACT.....	xvii
CHAPTER	
1. INTRODUCTION TO PHOTOSWITCHING MATERIALS.....	1
Molecular motors.....	3
Photochromic photoacids.....	12
Hydroxocobalamin and aquocobalamin.....	16
Notes on Chapter 1.....	22
2. EXPERIMENTAL METHODS.....	29
Titanium:sapphire oscillator.....	29
Chirped pulse amplification.....	30
Transient absorption.....	33
Synthesis and sample preparation.....	41
Notes on Chapter 2.....	46
3. FIRST GENERATION MOLECULAR MOTOR.....	48
Sample handling.....	50
P-cis transient absorption.....	52
P-trans transient absorption.....	60
M-trans transient absorption.....	67
Density functional theory calculations.....	69
Discussion.....	71
Conclusions.....	78

Notes on Chapter 3.....	80
4. PUMP-REPUMP OF THE MOLECULAR MOTOR.....	83
Sample handling.....	86
P-cis.....	87
P-trans.....	99
Discussion.....	109
Conclusions.....	112
Notes on Chapter 4.....	115
5. PHOTOCROMIC PHOTOACIDS.....	117
Sample handling.....	119
Computation methods.....	120
Phenylhydroxy-MCH in aqueous buffer.....	122
Indazole-MCH in aqueous buffer.....	126
Phenylhydroxy-MCH in DMSO.....	130
Indazole-MCH in DMSO.....	134
Phenylhydroxy-MC ⁻	137
Density functional theory calculations.....	139
Discussion.....	143
Conclusions.....	151
Notes on Chapter 5.....	153
6. HYDROXOCOBALAMIN AND AQUOCOBALAMIN.....	156
Hydroxocobalamin photochemistry.....	157
Comparison with theory.....	168
Aquocobalamin photochemistry.....	171
Polarization studies.....	173
Solvent dependence.....	175
Conclusions.....	176
Notes on Chapter 6.....	178
7. CONCLUSIONS AND FUTURE DIRECTIONS.....	180
Molecular motors.....	180
Photochromic photoacids.....	182
Hydroxocobalamin and aquocobalamin.....	183
Notes on Chapter 7.....	185

LIST OF FIGURES

- Figure 1.1** Schemes of photoswitching cycle of the molecules presented in this thesis. (a) Rotary cycle of the molecular motor investigated in chapters three and four, (b) Photoswitching cycle of the photochromic photoacids based on spiropyran investigated in chapter five, (c) photocatalytic cycle of hydroxyl radical formation by hydroxocobalamin and aquocobalamin investigated in chapter six4
- Figure 1.2.** Relevant structures of first-generation molecular motor under investigation. (a) 3-dimensional structures in their rotary cycle. (b) Newman projections of structures which demonstrate the helical nature of the molecule5
- Figure 1.3.** Synthetic evolution of the molecular motor. (a) Original first-generation molecular motor, relying on six membered fusing rings. The half-life of the unstable cis isomer at room temperature is 439 hours, (b) Improved first-generation molecular motor, relying on five membered fusing rings. This is the molecule studied in chapters three and four. The half-life of the unstable cis isomer is 43 minutes. (c) Second-generation molecular motor relying on a fluorene as the stator, the half life of the unstable conformation is 190 seconds7
- Figure 1.4.** UV-vis spectra of (a) phenylhydroxy photoacid and (b) indazole photoacid in their merocyanine and spiropyran forms. The merocyanine forms are given by the red spectra, and the spiropyran forms are given by the light blue spectra. The deprotonated Phenylhydroxy-MC⁻ merocyanine (a) spectrum is in dark blue.13
- Figure 1.5.** trans-phenylhydroxy-MCH conformers, similar conformers are possible for indazole-MCH as well. R group is propyl-sulfate in TA experiments, R group is CH₃ in DFT calculations.....14
- Figure 1.6.** Proposed scheme of photoswitching by trans-phenylhydroxy-merocyanine (MCH) to phenylhydroxy-spiropyran (SP). This scheme is adapted from “Long-Lived Photoacid Based upon a Photochromic Reaction” by Liao et al.⁷⁹15
- Figure 1.7.** (a) UV-vis spectra of cyanocobalamin (red), hydroxocobalamin (light blue), adenosylcobalamin (dark blue), cob(II)alamin (green), and (b) the corresponding structures.....18
- Figure 2.1.** Schematic of the oscillator. (1) first curved mirror, (2) titanium:sapphire crystal, angle of incidence is Brewster’s angle, (3) second curved mirror, (4) cavity folding mirror, (5) first cavity dispersion compensating prism, (6) second cavity dispersion compensating prism, (7) high reflector, and (8) output coupler.29

Figure 2.2. Simple diagrams of (a) stretcher and (b) compressor. For the stretcher (a), (1) $f = 500$ mm curved mirror, (2) diffraction grating, (3) flat folding mirror, and (4) pick-off mirror. For the compressor (b), (1) diffraction grating 1, (2) diffraction grating 2, (3) hollow retro mirror, (4) pick-off mirror.31

Figure 2.3. Schematic of the eight-pass amplifier. (1) Oscillator injection mirror, (2) folding mirror, (3) mask, (4) $f = 300$ mm pump laser lens, (5) $f = 500$ mm curved mirror, (6) ti:sapph gain medium, (7) $f = 500$ mm pump retro mirror, (8) $f = 500$ mm curved mirror, and (9) amplified pulse pick-off mirror.32

Figure 2.4. Schematic of the TA setup. (1) Optical chopper, (2) SHG BBO crystal, (3) THG BBO crystal, (4) $f = 250$ mm pump focusing lens, (5) $f = 90$ mm quartz achromatic lens, (6) computer controlled delay line, (7) $f = 100$ mm lens, (8) 5 mm thick CaF_2 window, (9) either KG3 filter or nickel sulfate filter, (10) $f = 500$ mm curved aluminum mirror.34

Figure 2.5. Schematic of the two synchronized pump and repump choppers. The pump chopper operates at 500 Hz, the repump chopper operates at 250 Hz, and the unchopped probe functions at 1 kHz. The three needed TA signals are acquired every four shots of the probe. Thus, the reference (pump OFF) for each signal is acquired first, then pump ON, then repump ON, the pump and repump ON.....40

Figure 2.6. Synthesis scheme for McMurry coupling to form both the cis and trans molecular motor isomers.....41

Figure 3.1. (a) Steady state UV-vis spectra of P-Cis (solid red) and P-trans (solid blue) in heptane. Normalized steady state fluorescence spectra of P-Cis (dash red) and P-trans (dash blue) in heptane. Black arrows mark the excitation wavelengths used TA experiments. (b) Comparison of P-cis (red) and M-cis (purple) steady state UV-vis spectra. (c) Comparison of P-trans (light blue) and M-trans (dark blue) UV-vis spectra..... 49

Figure 3.2. TA spectra of P-cis molecular motor excited with 404 nm. Early time spectra (a) at 0.5 ps (green), 1.0 ps (blue), 2.0 ps (purple), 6.0 ps (yellow) and 10 ps (red). Later time spectra (b) at 25 ps (red), 60 ps (yellow), 90 ps (purple), 130 ps (blue), and 300 ps (green).....53

Figure 3.3. TA spectra of the P-cis molecular motor excited with 269 nm. Early time spectra (a) at 0.5 ps (green), 1.0 ps (blue), 2.0 ps (purple), 6.0 ps (yellow) and 10 ps (red). Later time spectra (b) at 25 ps (red), 60 ps (yellow), 90 ps (purple), 130 ps (blue), and 300 ps (green).....54

Figure 3.4. Comparison of steady state TA spectrum (dark blue) to P-cis (red), M-trans (light blue) UV-vis spectra, and the difference between M-trans and P-cis (grey dash). Steady state TA spectrum was scaled by a factor $\alpha = 43,000$55

Figure 3.5. Kinetic lineouts from P-cis in heptane using either 404 nm as the pump (a and b) or 269 nm as the pump (c and d). Early times in the top panels (a and c) and late times in the bottom panels (b and d). 370 nm (light blue) tracks the GSB, 420 nm (dark blue) tracks the SE and the photoproduct, 475 nm (purple) tracks SE and the intermediate state, and 700 nm (red) tracks the early ESA.....	57
Figure 3.6. Decay associated difference spectra (DADS) of P-cis in heptane after 404 nm excitation. DADS are the amplitudes at every wavelength of each decay term in the global fit.....	58
Figure 3.7. Anisotropy of P-cis in heptane SADS assuming a sequential kinetic model after excitation with 404 nm (a-d) or 269 nm (e-h).	60
Figure 3.8. TA spectra of P-trans in heptane and excitation with 368 nm. Early times (a) 0.5 ps (green), 1.5 ps (blue), 3.0 ps (purple), 5.0 ps (yellow), 7.0 ps (red), and 10 ps (dark blue). Later times (b) 10 ps (dark blue), 20 ps (red), 30 ps (yellow), 50 ps (purple), and 300 ps (light blue).....	61
Figure 3.9. TA spectra of P-trans in heptane and excitation with 269 nm. Early times (a) 0.5 ps (green), 1.5 ps (blue), 3.0 ps (purple), 5.0 ps (yellow), 7.0 ps (red), and 10 ps (dark blue). Later times (b) 10 ps (dark blue), 20 ps (red), 30 ps (yellow), 50 ps (purple), and 300 ps (light blue)	62
Figure 3.10. Comparison of steady state TA spectrum to P-trans and M-cis. Steady state TA spectrum was scaled by a factor $\alpha = 220,000$	63
Figure 3.11. Kinetic lineouts from the P-trans in heptane TA data using either 368 nm as the pump (a and b) or 269 nm as the pump (c and d). Early times in the top panels (a and c) and late times in the bottom panels (b and d). 345 or 368 nm (light blue) tracks the GSB, 400 nm (dark blue) tracks the SE and the photoproduct, 450 nm (purple) tracks SE on and the intermediate state, and 600 nm (red) tracks the early ESA.....	64
Figure 3.12. Anisotropy of P-trans in heptane SADS assuming a sequential kinetic model after excitation with 368 nm (a-d) or 269 nm (e-h).....	66
Figure 3.13. TA spectra of M-trans excited with 404 nm in heptane. (a) Early time spectra at 0.5 ps (green), 1.5 ps (blue), 2.0 ps (purple), 4.0 ps (yellow) and 10 ps (red). (b) Later time spectra at 10 ps (red), 25 ps (yellow), 50 ps (purple), 80 ps (blue), and 250 ps (green).....	68
Figure 3.14. Kinetic lineouts from the M-trans in heptane TA data using 404 nm as the pump. Early times (a) and late times in the bottom panel (b). 390 nm (light blue) tracks the ground state bleach, 450 nm (dark blue) tracks the intermediate state, 550 nm (purple) tracks SE and the intermediate state, and 640 nm (red) tracks the early ESA.....	68

Figure 3.15. Kinetic lineouts of P-cis after being with <i>parallel</i> pump polarization 404 nm. 483 nm (light blue), 487 nm (dark blue), 495 nm (purple), 525 nm (red). SE signal continues for \geq 10 ps.....	72
Figure 3.16. Decay associated difference spectra of P-trans dissolved in heptane and excited with 269 nm. Note the broad featureless amplitude associated with the 45 ps component. This is likely an artifact of using 269 nm, either coming from the solvent or multi-photon ionization of the sample.....	76
Figure 3.17. UV-vis spectra of P-trans (light blue), M-trans (dark blue dash), and 4.5% M-trans (dark blue). (Inset) Zooming in demonstrates the agreement between the shoulder of the P-trans (light blue) and the scaled amount of M-trans (dark blue).....	77
Figure 3.18. Comparison of M-trans UV-vis (teal blue), and M-trans steady state fluorescence excited by 405 nm (yellow), to the first SADS spectrum (red) from a global analysis of TA data on M-trans.....	78
Figure 4.1. Relative populations of the excited states and photoproducts of (a) P-cis and (b) P-trans after excitation by 269 nm. The black arrows indicate various delays for the 404 nm repump pulse.....	84
Figure 4.2. 1 ps PDP TA spectra of the P-cis molecular motor. Pump pulse was 269 nm and the dump pulse was 404 nm. (a) PDP spectra at early times: 0.5 ps (green), 1.0 ps (blue), 2.0 ps (purple), 6.0 ps (yellow), 10 ps (red). (b) PDPP spectra at later times: 10 ps (red), 25 ps (dark blue), 60 ps (yellow), 90 ps (purple), 130 ps (royal blue), 300 ps (green).....	88
Figure 4.3. Results of global analysis of P-cis 1 ps PDP data. (a) DADS and (b) SADS. Lifetimes from global analysis are 0.45 ps (red), 11 ps (green), 92 ps (blue) and \gg 300 ps (yellow).....	89
Figure 4.4. Kinetic lineouts (red), fits (black dash) and residuals (grey dash) of the P-cis 1ps PDP data. (a) 370 nm lineout tracking the depleted GSB, (b) 420 nm lineout tracking the depletion of the photoproduct, (c) 475 nm lineout tracking the depletion of SE and intermediate excited states, and (d) 700 nm lineout tracking the depletion of the initial excited state.....	90
Figure 4.5. PrPP TA spectra after 10 ps repump of P-cis with 404 nm. (a) PrPP spectra at early times: 0.5 ps (green), 1.0 ps (blue), 3.0 ps (purple), 6.0 ps (yellow), 14 ps (red), M-trans UV-vis (grey dash). (b) PrPP spectra at later times: 14 ps (red), 25 ps (yellow), 55 ps (purple), 75 ps (blue), 250 ps (green), M-trans UV-vis (grey dash).....	92
Figure 4.6. Global fitting results after 10 ps repump of P-cis with 404 nm pulses. (a) DADS and (b) SADS (assuming a sequential kinetic model.) The SADS appear to inverted forms of the M-trans SADS spectra.....	93

Figure 4.7. Kinetic lineouts from the global analysis of the 10 ps delayed 404 nm repump experiment on P-cis. The data are integrated over the three main spectral features to provide reasonable signal to noise. Data given in red, fits are black dashed lines and residuals are grey dashed lines. (a) the bleach of the M-trans GSB 370-395 nm, (b) bleach of repumped ESA 430 – 460 nm, and (c) the bleach of the ESA 630 – 660 nm.....94

Figure 4.8. PrPP TA spectra of M-trans. (a) Spectra at early times: 0.5 ps (green), 1.0 ps (blue), 2.0 ps (purple), 4.0 ps (yellow), 10 ps (red), and inverted M-trans UV-vis spectra for comparison to the ground state bleach (grey dash). (b) Spectra at later times: 10 ps (red), 25 ps (yellow), 50 ps (purple), 80 ps (blue) and 250 ps (green), inverted M-trans UV-vis spectra for comparison to the ground state bleach (grey dash).....96

Figure 4.9. Global analysis results of the M-trans PrPP data, acquired by repumping P-cis at 300 ps after initial excitation. (a) Decay associated difference spectra DADS and (b) species associated difference spectra of the M-trans conformer, 2.3 ps component's amplitude (red) and 37 ps component's amplitude (green). A 3rd time independent component (blue) was used to account for any baseline issues. The SADS assume a sequential kinetic model.....97

Figure 4.10. Kinetic lineouts of the M-trans PrPP data. (a) GSB signal integrated from 380 to 400 nm, (b) ESA signal integrated from 440 to 460 nm, (c) SE signal integrated from 520 to 600 nm, and (d) ESA signal integrated from 640 to 660 nm. Dashed black lines are the fits of the data and the grey lines are the residuals.....98

Figure 4.11. PDP spectra of P-trans. The excitation pulse was 269 nm and dump pulse was 404 nm, delayed by 1 ps. (a) PDPP spectra at early times, 0.5 ps (green), 1.5 ps (blue), 3.0 ps (purple), 5.0 ps (yellow), and 10 ps (red). (b) PDPP spectra at later times, 10 ps (red), 20 ps (yellow), 30 ps (purple), 50 ps (blue), and 300 ps (green).....100

Figure 4.12. Results of global analysis of P-trans PDP data. (a) DADS and (b) SADS, assuming a sequential model. The lifetimes obtained from fitting the data are $\tau_1 = 3.5$ ps, $\tau_2 = 11$ ps, $\tau_3 = 48$ ps, and $\tau_4 \gg 300$ ps.....101

Figure 4.13. P-trans PDP kinetic lineouts (red), fits (black dash), and residuals (grey dash). (a) 345 nm tracks the GSB and depletion of photoproduct signal, (b) 400 nm tracks depletion of SE at early times and depletion of photoproduct at later times, (c) 450 nm tracks the GSB of the intermediate excited state "C", and (d) 750 nm tracks the bleach of the initial excited states "A" and "B.".....102

Figure 4.14. P-trans 8 ps PrPP spectra. (a) early times, 0.5 ps (green), 1.75 ps (blue), 3.0 ps (purple), 6.0 ps (yellow), and 14 ps (red). (b) Spectra at later times, 14 ps (red), 20 ps (yellow), 100 ps (blue), and 300 ps (green). M-cis UV-vis (grey dash).....104

Figure 4.15. PrPP spectra of the M-cis conformer, acquired by repumping P-trans with 404 nm, 300 ps after excitation. (a) Spectra at early times: 0.75 ps (green), 1.0 ps (blue), 3.0 ps (purple), 5.0 ps (yellow), 10 ps (red), and grey dash is an inverted UV-vis spectrum of M-cis. (b) Spectra at later times: 10 ps (red), 15 ps (yellow), 20 ps (purple), 40 ps (blue), and 250 ps (green), and grey dash is M-cis UV-vis.....106

Figure 4.16. PrPP spectra of the M-cis conformer, acquired by repumping P-trans with 404 nm, 65 ps after excitation. (a) Spectra at early times: 0.75 ps (green), 1.0 ps (blue), 3.0 ps (purple), 5.0 ps (yellow), 10 ps (red), and grey dash is an inverted UV-vis spectrum of M-cis. (b) Spectra at later times: 10 ps (red), 15 ps (yellow), 20 ps (purple), 40 ps (blue), and 250 ps (green), and grey dash is M-cis UV-vis.....107

Figure 4.17. Global analysis results of PrPP data acquired by repumping M-cis with 404 nm. (a) DADS and (b) SADS assuming a sequential kinetic model.....108

Figure 4.18. Kinetic lineouts of the M-cis PrPP data. (a) signal integrated over the ESA signal from 430 to 525 nm, (b) signal integrated over the ESA signal from 750 to 800 nm. Data shown in red, fits in black dash, and grey dash is residuals.....109

Figure 4.19. Comparison of P-trans photoproduct difference spectrum (blue) from TA and -28*M-cis photoproduct difference spectrum (green) from PrPP.....110

Figure 4.20. Scheme depicting the excited state dynamics of P-trans and M-cis. (*left hand side*) Excitation of P-trans with 269 nm produces a highly excited state, which quickly relaxes to the “A” state. Excitation of P-trans with 368 nm populates the “A” state, which relaxes from the Franck Condon region on a 500 fs timescale forming the “B” state. The “B” state relaxes to the “C” state on a 3.6 ps timescale, and the “C” reaches a conical intersection (CI) branching between P-trans and M-cis on a 12 ps timescale. (*right hand side*) Excitation of M-trans populates a bright state, which relaxes to form a dark state on a 1.2 timescale. The dark state reaches the same CI branching between P-trans and M-cis a on a 20 ps timescale.....111

Figure 4.21. Scheme depicting the excited state dynamics of P-cis and M-trans. (*left hand side*) Excitation of P-cis with 269 nm produces a highly excited state, which relaxes to the “A” state quickly. “A” is a bright state, which decays to “B” another bright state, on a 0.9 ps timescale. “B” relaxes to a dark state “C” on a 17 ps timescale. At “C” there is branching between two pathways with separate conical intersections CI 1 and CI 2 with two rates k_a and k_b , whose sum is $1/(71 \text{ ps})$. CI 1 leads to recovery of P-cis while CI 2 leads to formation of M-trans with unit quantum yield. (*right hand side*) A small population of M-trans exists in equilibrium with P-trans in solution. M-trans absorbs 404 nm while P-trans does not. Excitation by 404 nm puts M-trans in a bright excited state with a lifetime of 2.3 ps. This state forms a dark excited state with a 40 ps lifetime reaching CI 2 to form M-trans with unit quantum yield.....113

Figure 5.1. (a) Phenylhydroxy-MCH UV-vis in aqueous solution buffered at 5 (red, solid) and DMSO (red, dash), phenylhydroxy-MC⁻ in aqueous solution buffered at pH 10 (dark blue), and phenylhydroxy-SP in aqueous solution buffer at pH 5 (light blue, solid) and DMSO (light blue, dash). (b) Indazole-MCH UV-vis in aqueous solution buffered at pH 7.4 (red, solid) and DMSO (red, dash), and indazole-SP in aqueous solution buffered at pH 7.4 (light blue, solid) and DMSO (light blue, dashed). TA pump wavelengths marked with black arrows.....118

Figure 5.2. (a) TA spectra of phenylhydroxy-MCH at 0.5 ps (green), 0.7 ps (blue), 0.9 ps (purple), 1.1 ps (yellow), 1.5 ps (red), and scaled UV-vis of phenylhydroxy-MCH (grey dash). (a) TA spectra of phenylhydroxy-MCH at 1.5 ps (red), 3.0 ps (yellow), 8.0 ps (purple), 20 ps (blue) and 50 ps (green), scaled UV-vis of phenylhydroxy-MCH (grey dash).123

Figure 5.3 (a) Decay associated difference spectra (DADS) of phenylhydroxy-MCH in citrate buffer, (b) Species associated difference spectra (SADS) of phenylhydroxy-MCH assuming a sequential model.....125

Figure 5.4. Kinetic lineouts of phenylhydroxy-MCH in 11 mM pH 5.5 citrate buffer after 404 nm excitation, data in color, fit is black dash, residuals in grey. 450 nm in blue, 500 nm in purple, 550 nm in red. (a) Early times from 0 to 50 ps, (b) all times from 0 to 3500 ps.....126

Figure 5.5. (a) TA spectra of indazole-MCH at 350 fs (green), 500 fs (blue), 750 fs (purple), 1.0 ps (yellow) and 2.0 ps (red), scaled UV-vis of indazole-MCH (grey dash). (b) TA spectra of indazole-MCH at 2.0 ps (red), 5.0 ps (yellow), 20 ps (purple), 60 ps (blue) and averaged from 1 – 3.5 ns (green), scaled UV-vis of indazole-MCH (grey dash). Spectra are a result of combining two datasets, one using a visible probe (~350 – 800 nm) and one using a UV probe (~270 – 600 nm). The UV continuum dataset was scaled by 0.22 to match the intensities of the visible dataset.....127

Figure 5.6. Kinetic lineouts of indazole-MCH at select wavelengths in PBS after excitation with 404 nm. Colorful traces are the measured data, dashed lines are the fits, and the grey lines are residuals. 440 nm tracks the GSB in blue, 525 nm tracks the ESA in purple, 585 nm track the SE in red. (a) Early times from 0 to 50 ps, (b) all time delays from 0 to 3500 ps.....129

Figure 5.7 (a) Decay associated difference spectra (DADS) of indazole-MCH in PBS, (b) Species associated difference spectra (SADS) of indazole-MCH assuming a sequential model.....130

Figure 5.8. TA spectra of phenylhydroxy-MCH in DMSO at early times (a) 0.8 ps (green), 1.5 ps (blue), 4.0 ps (purple), 10 ps (red). Longer times (b) 10 ps (red), 30 ps (yellow), 60 ps (purple), 100 ps (blue) and 2000 ps (green). Scaled UV-vis of phenylhydroxy-MCH (grey dash).....131

Figure 5.9. TA lineouts of the phenylhydroxy-MCH dissolved in DMSO at selected wavelengths at (a) early times and (b) longer times. 290 nm (light blue) tracks early ESA and later photoproduct absorption in light blue, 435 nm (dark blue) tracks early ESA and GSB, 500 nm (purple) tracks ESA, and 600 nm (red) tracks SE.....133

- Figure 5.10** (a) Decay associated difference spectra (DADS) of phenylhydroxy-MCH in DMSO, (b) Species associated difference spectra (SADS) of phenylhydroxy-MCH assuming a sequential model.....134
- Figure 5.11.** (a) TA spectra of indazole-MCH in DMSO at 0.2 ps (red), 0.35 ps (yellow), 0.75 ps (purple), 2.0 ps (blue), 5.0 ps (green). (b) 5.0 ps (green), 50 ps (blue), 100 ps (purple), 210 ps (yellow) and 2000 ps (red), and scaled UV-vis (grey dash). INSET: 3000 ps spectrum.....135
- Figure 5.12.** TA lineouts, fits and residuals at select wavelengths of indazole-MCH in DMSO after excitation with 404 nm. 420 and 450 nm (light blue and dark blue, respectively) track the GSB, 490 nm (purple) tracks ESA, 575 nm (red) tracks SE. (a) Early time delays and (b) longer time delays.....136
- Figure 5.13** (a) Decay associated difference spectra (DADS) of indazole-MCH in DMSO, (b) Species associated difference spectra (SADS) of indazole-MCH assuming a sequential model.....137
- Figure 5.14.** (a) TA spectra of phenylhydroxy-MC⁻ in buffer excited with 530 nm at 200 fs (green), 300 fs (blue), 500 fs (purple), 700 fs (yellow), 1.0 ps (red), and scaled UV-vis (grey dash). (b) TA spectra at 1.0 ps (red), 3.0 ps (yellow), 8.0 ps (purple), 20 ps (blue), 500 ps (green), and scaled UV-vis (grey dash). INSET: difference spectra averaged from 250 to 3400 ps (green), baseline signal (blue), scaled UV-vis (grey dash).....139
- Figure 5.15.** Structures from DFT optimizations, R = CH₃.....140
- Figure 5.16.** Comparison of 3500 ns TA spectrum (green) of *trans*-phenylhydroxy-MCH in citrate buffer excited with 404 nm to the steady state difference spectra (black dash) between phenylhydroxy-SP (black) and *trans*-phenylhydroxy-MCH (grey).....143
- Figure 5.17.** (a) Comparison of UV-vis of *trans*-phenylhydroxy-MCH in buffer to simulated spectra of *trans* conformation using 0.2 eV Gaussian functions centered at vertical transition energies calculated by TD-DFT. TTT is red, TTC is green, CTT is blue and CTC is magenta. (b) Simulated *cis*-phenylhydroxy-MC⁻ spectra, CCC conformer is red, TCT conformer is green, and CCT conformer is blue.....144
- Figure 5.18.** Simulated difference spectrum between *cis*-phenylhydroxy-MC⁻ and *trans*-phenylhydroxy-MCH (red and blue) in comparison to 3.5 ns TA spectrum of phenylhydroxy-MCH in citrate buffer (black).....146
- Figure 5.19.** Comparison of 3500 ns TA spectrum (green) of *trans*-phenylhydroxy-MCH in DMSO excited with 404 nm to the steady state difference spectra (black dash) between phenylhydroxy-SP (black) and *trans*-phenylhydroxy-MCH (grey).....148
- Figure 5.20.** Results of transition state search between CCC-phenylhydroxy-MC⁻ and phenylhydroxy-SP using growing string method. The activation energy is 4.5 kcal/mol when a hydrogen bond is present, relative to 2.3 kcal/mole when there is no hydrogen bond present...149

Figure 5.21. Indazole-MCH in (a) PBS or (b) DMSO. 3500 ns TA spectrum (green), <i>trans</i> -indazole-MCH UV-vis (grey), indazole-SP UV-vis (black), SP-MCH (black dash).....	150
Figure 6.1. (a) Molecular structure of hydroxocobalamin (HOCbl), and (b) truncated structure of hydroxocobalamin used in TDDFT calculations.....	156
Figure 6.2 (a) Photolysis of HOCbl using an unfiltered mercury pen lamp. (b) The final spectrum is consistent with the cob(II)alamin spectrum obtained following excitation of alkylcobalamins (red dashed line), indicating that the photolysis has gone to completion.....	157
Figure 6.3. (a) Contour plot of the transient absorption data following excitation at 269 nm. (b) Contour plot of the transient absorption data following excitation at 404 nm.....	159
Figure 6.4. Fits to the transient absorption data following excitation at 269 nm at select time delays. Although there may be a small residual photoproduct yield following 269 nm excitation (<1.5%), overall the transient data are similar for both excitation wavelengths.....	160
Figure 6.5. Select kinetic traces and fits following excitation at 269 nm.....	161
Figure 6.6. Comparison of time traces at 540 nm following 269 nm excitation and 404 nm excitation. The inset compares the residual difference spectrum at time delays >100 ps with the steady state difference spectrum for photolysis to cob(II)alamin. These data set an upper limit of <1% photolysis yield following 404 nm excitation and $1.5\% \pm 0.5\%$ photolysis yield following 269 nm excitation.....	162
Figure 6.7. Excited state spectra estimated from the SADS for the (a) S_n state and the (b) S_1 state. The excited population is ca. 8% following 404 nm excitation and 13% following 269 nm excitation.....	163
Figure 6.8. (a) Potential energy surfaces for the ground and two lowest singlet states of the Im-[Co ^{III} (corrin)]-OH ⁺ model complex generated as vertical excitations and plotted as a function of axial bond lengths (expressed in Å). (b) Vertical projections of the S1 potential energy surface. (c) Vertical projections of the S2 potential energy surface.....	164
Figure 6.9. . Potential energy curves of the ground and lowest singlet excited states of the Im-[Co ^{III} (corrin)]-OH ⁺ model complex along the Co-C bond stretch computed at the ground state optimized geometry. (Figure reproduced from ref 1 supplemental information Fig. S9).....	166
Figure 6.10. Potential energy surface for the S_1 electronic state of the Im-[Co ^{III} (corrin)]-OH ⁺ model complex in the optimized geometry of the excited state plotted as a function of axial bond lengths. (Figure reproduced from ref. 1 Supplemental Information Figure S10).....	167
Figure 6.11. Comparison of Co-R and Co-N _{Im} bond lengths for Im-[Co ^{III} (corrin)]-OH ⁺ and Im-[Co ^{III} (corrin)]-CN ⁺ model complexes (red – in S_0 optimized geometries, blue - in S_1 optimized geometries, grey – experimental S_0 data).....	168

Figure 6.12. Scheme of potential energy curves involved in in the process of the deactivation and dissociation.....	169
Figure 6.13. UVvis spectra of HOCbl and H ₂ OCbl. The γ band for HOCbl is centered at 355 nm and 351 nm for H ₂ OCbl. The $\alpha\beta$ band for HOCbl is red-shifted with respect to H ₂ OCbl.....	170
Figure 6.14. Transient absorption spectra of OH ₂ Cbl excited with 560 nm.....	171
Figure 6.15. (a) HOCbl spectra: ground state (black), estimates of S _n (red dash) and S ₁ states (blue dash), and SADS of S _n (solid red) and S ₁ (solid blue), (b) H ₂ OCbl spectra: ground state (black), estimates of S _n (red dash) and S ₁ states (blue dash), and SADS of S _n (solid red) and S ₁ (solid blue).....	173
Figure 6.16. (a) Hydroxocobalamin S ₁ SADS spectrum (blue) and the anisotropy of that species (grey), (b) Aquocobalamin S ₁ SADS spectrum (blue) and the anisotropy of that species (grey).....	174
Figure 6.17. Normalized kinetic lineouts of the $\alpha\beta$ band (a) HOCbl integrated from 530 to 550 nm and (b) H ₂ OCbl integrated from 515 to 545 nm. Green is in a 1:1 buffer:ethanol mixture, blue is in buffer.....	176

LIST OF TABLES

Table 3.1. Typical time-points and step sizes used in a TA experiment.....	51
Table 3.2. Rate constants obtained from global fits of P-cis TA data in heptane and 2-butanol, using 404 or 269 nm as pump wavelengths.....	56
Table 3.3. Rate constants obtained from global fits of the P-trans TA data in heptane and 2-butanol, using either 368 or 269 nm as pump wavelengths.....	65
Table 3.4. M-trans global fitting results in heptane and 2-butanol, excitation wavelength is 404 nm.....	68
Table 3.5. Thermodynamic properties of all four conformations of the molecular motor. Quantities were obtained by frequency calculations in DFT, using PBE0/6-31G**.....	70
Table 3.6. Vertical excitation energies of all four conformations of the molecular motor calculated using TDDFT with PBE0/6-31G** and are compared to the measured peaks in the UV-vis spectra. (<i>f</i> is the oscillator strength of the transition). Top value in each cell is calculated in vacuum, middle value is calculated with PCM in dielectric constant = 1.92 and refractive index = 1.39 (heptane) and bottom value is calculated with PCM in dielectric constant = 17.26 and refractive index = 1.40 (2-butanol).....	71
Table 3.7. Activation energies for thermal helix inversion for both molecular isomers. Second column contains reported activation energies.....	71
Table 5.1. Global fitting results of Phenylhydroxy-MCH and indazole-MCH in aqueous citrate buffer and anhydrous DMSO.....	124
Table 5.2. Free energies obtained from DFT frequency calculations, using B3LYP/6-311G** in a polarizable continuum ($n = 80.4$, water).....	141
Table 5.3. Vertical excitation maxima and intensities for relevant structures calculated with TDDFT, PCM ($n = 80.4$), B3LYP/6-311G**.....	142

ABSTRACT

The photochemistry and photophysics of three types of photoswitchable compounds have been investigated. Chiral overcrowded alkenes, which undergo unidirectional photoisomerization are examples of light driven molecular-scale motors. Photochromic photoacids based on the reversible light induced ring-closure and ring-opening of spiropyran and merocyanine release a proton causing a large drop in pH upon switching from the ring-open merocyanine to the ring-closed spiropyran form. Hydroxocobalamin and aquocobalamin, derivatives of vitamin B₁₂, act as light activated hydroxyl radical catalysts under aerobic conditions in solution. Ultrafast UV-vis transient absorption spectroscopy has been used to investigate the details of excited state dynamics and photoproducts involved in the photochemistry of these molecules.

Light driven molecular motors undergo 360° of internal rotation about their central carbon-carbon double bond in four steps: P-cis → M-trans → P-trans → M-cis, etc. The cis to trans and trans to cis steps are photoisomerizations, while the “M” to “P” steps are thermal conformational changes. Transient absorption spectroscopy and pump-repump probe (PrPP) spectroscopy were used to probe the excited state behavior of all four conformations of the molecular motor. We have found evidence for unintended backward isomerization in the M-cis conformation, previously thought to be insensitive to photoexcitation.

Spiropyran and merocyanine can reversibly interchange upon absorption of light. Merocyanine is a planar π conjugated molecule with visible absorption bands. Spiropyran possesses a central “spiro” carbon breaking the conjugation between both sides of the molecule,

and therefore has absorption bands in the UV. The indazole and phenol based versions of merocyanine/spiropyran investigated here display a large pKa difference between the merocyanine and spiropyran forms. As a result, light activated ring closure of merocyanine to form spiropyran is accompanied by a drop in pH of ~ 2 units. Transient absorption in aqueous solution and a polar aprotic solvent (DMSO) uncovered solvent effects in the photochemical formation of spiropyran. In the phenol-based merocyanine, water appears to extend the lifetime of the cis-merocyanine precursors to spiropyran.

Hydroxocobalamin (HOCbl) and aquocobalamin (H_2OCbl) are derivatives of vitamin B_{12} that have long been thought to be photostable. However, recent transient absorption studies and anaerobic photolysis experiments have demonstrated otherwise. Transient absorption experiments exciting with 269 nm light show homolytic bond cleavage to form hydroxyl radicals and cob(II)alamin with $\sim 1.5\%$ quantum yield. In addition, anaerobic photolysis with wavelengths ≤ 300 nm demonstrates homolysis as well. As a result, HOCbl and H_2OCbl are potential hydroxyl radical photocatalysts.

Chapter 1

Introduction to photoswitching materials

Nature is an abundant source of inspiration for chemists. Natural systems interact ingeniously with the environment to transform energy – light energy, chemical energy, electrical potential – into useful work. Living systems consist of molecular-scale “machines” harmoniously performing their microscopic functions manifesting as macroscopic life. All the macromolecules in a cell work together, the cells in a specific tissue or organ work together, and all of the tissues of a living organism together. Zooming out from this microscopic picture, a view of macroscopic life comes into focus.

Human beings discovered how to build machines such as motors and pumps at the beginning of the industrial revolution. Humanities’ relatively recent discovery pales in comparison to how long ago single celled organisms developed motors and pumps. Over the years, scientists have delighted in discovering incredibly intricate molecular machines orchestrating life on the cellular level. ATP synthase is a molecular scale rotary pump driven by electrochemical gradients across the mitochondrial membrane, which synthesizes the cellular currency of energy for all life adenosine tri-phosphate (ATP)¹⁻³. Molecular walkers such as dynein and kinesin “walk” up and down the cytoskeletons of our cells, powered by the hydrolysis of ATP, transporting cargo throughout the cell^{4,5}. The bacterial flagellar motor is a rotary motor imbedded in bacterial membranes, which is powered by chemical energy and allows bacteria to move along chemical gradients⁶. The molecular machinery of cells demonstrate that it is possible to build smaller and smaller machines⁷⁻⁹.

The previous examples of molecular scale machines rely on chemical energy, but light is a useful source of energy for powering molecular machines as well. Light has many easily controllable attributes, such as wavelength, intensity, phase, and timing. This gives the designers of light driven molecular devices a high degree of control over their machines. And of course, nature thought of it first. One only needs to open their eyes and experience vision to appreciate a light driven molecular scale machine. The retinal molecules contained in your eyes photoisomerize upon absorption of light inducing a signaling cascade which manifests as vision^{10,11}.

Pulsed lasers provide invaluable tools for studying and controlling light driven molecular devices. Pulsed lasers deliver incredible intensities of light over a wide range of wavelengths in ultrashort pulses. Ultrafast spectroscopy probes timescales in the femtosecond (fs, 10^{-15} second) to picosecond (ps, 10^{-12} second) range, which is the timescale of many photochemical processes such as bond isomerization and bond photolysis¹². This technique reveals key details about how a molecule absorbs light and converts that energy into useful work. The research presented here relies heavily upon ultrafast spectroscopy to uncover mechanistic details about the functioning of light driven molecular-scale devices.

Overview of work presented. The research presented here covers three photo-switchable molecular systems intended for use in molecular scale machines and devices. Chapters three and four encompass light driven molecular motors based on chiral overcrowded alkenes. Chapter five deals with photochromic photoacids based on the spiropyran/merocyanine (SP/MC) system. Chapter six discusses light activated hydroxyl radical reagents based on vitamin B₁₂ derivatives, hydroxocobalamin (HOCbl) and aquocobalamin (H₂OCbl). The line drawing structures of these molecules and simple schemes for their photochemical mechanisms are shown in Figure 1.1. In

all of these cases, time-resolved ultraviolet and visible transient absorption (UV-vis TA) spectroscopy covering the femtosecond to nanosecond (ns, 10^{-9} second) timescales is used to track the evolution of excited electronic states and formation of photoproducts. UV-vis TA is uniquely suited to measure the spectra of transient species, which are difficult to capture in a standard chemistry lab setting.

Molecular motors. Professor Ben Feringa and co-workers developed light-driven rotary motors based on the cis/trans and trans/cis isomerization of chiral overcrowded alkenes in the 1990's¹³⁻¹⁵. Similar to most alkenes – ethylene, stilbene, azobenzene – undergoing cis/trans photoisomerization, π - π^* excitation of the central carbon-carbon double bond induces twisting of the carbon-carbon bond to a perpendicular geometry. Pyramidalization of one of the carbons from a planar (sp^2) geometry to a pyramidal (sp^3) geometry allows the molecule to access a conical intersection with the ground state, completing the cis/trans isomerization. Unlike the less crowded systems known to undergo cis/trans isomerization¹⁶⁻²¹, chiral overcrowded alkenes developed by Feringa et al. undergo unidirectional photoisomerization. Symmetric molecules like ethylene, trans-stilbene, and trans-azobenzene, have no preference for isomerization in one direction over another because of their symmetry. The unidirectional photoisomerization observed in chiral overcrowded alkenes is an immensely useful property utilized in applications ranging from light activated metastable pharmaceuticals²², photo-switchable hydrophobic surfaces²³, and even providing the motive force for light driven nano-cars and nano-submarines²⁴⁻²⁷.

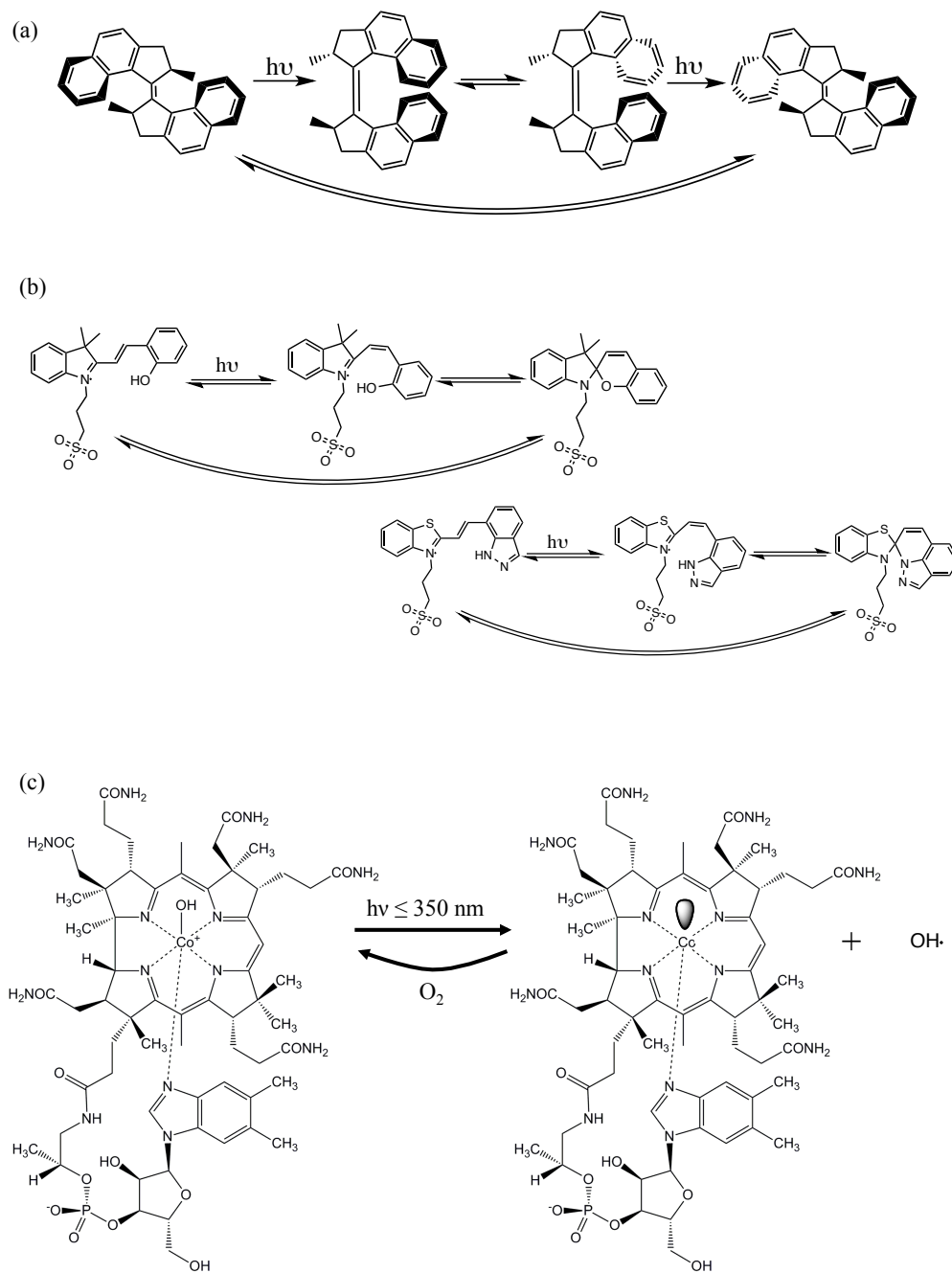


Figure 1.1 Schemes of photoswitching cycle of the molecules presented in this thesis. (a) Rotary cycle of the molecular motor investigated in chapters three and four, (b) photoswitching cycle of the photochromic photoacids based on spiropyran investigated in chapter five, (c) photocatalytic cycle of hydroxyl radical formation by hydroxocobalamin and aquocobalamin investigated in chapter six.

The key insight Professor Feringa brought to the field was steric crowding on the periphery of the chromophore induces the molecule to take on a helical shape, as depicted by the 3-D structures and Newman projections in Figure 1.2. As a result, the excited state potential energy surface governing the direction of photoisomerization becomes asymmetric²⁸ along the central carbon-carbon twisting coordinate. The asymmetric molecular motor isomerizes in only one direction, like the rotor of a motor^{13,14,29}. The early work in this field relied on low temperature photolysis and circular dichroism studies to prove unidirectional photoisomerization was occurring¹³⁻¹⁵. Several synthetic, spectroscopic, and theoretical investigations have been undertaken to determine the details of the rotary cycle of these novel light-driven molecular motors.

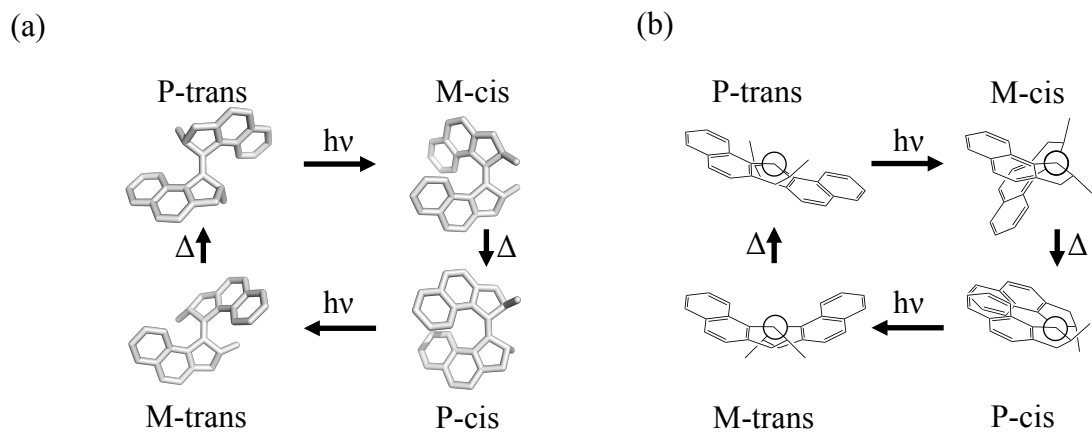


Figure 1.2. Relevant structures of first-generation molecular motor under investigation. (a) 3-dimensional structures in their rotary cycle. (b) Newman projections of structures, which demonstrate the helical nature of the molecule.

The “first-generation” molecular motors are synthetic modifications to stiff stilbene, which incorporate a methyl group on one side of the strain imposing cyclohexane ring of stiff stilbene and naphthyl rings on the other side as shown in Figures 1.2 and 1.3. The first-generation

molecular motors consist of two identical sub-units on either side of the central carbon-carbon double bond, existing as either cis or trans isomers. In the case of the cis isomer, the naphthyl groups interact with each other via steric repulsion and take on a gauche-like configuration, where the naphthyl groups on either side of the carbon-carbon double bond have an angle of much less than 120° . In the case of the trans isomer, a methyl group interacts with the aromatic rings on the opposite side of the double bond, again adopting a gauche configuration as shown in Figure 1.2. The molecular motor adopts a helical geometry, which could have right-handed (P) or left-handed (M) helicity. The chirality of the molecule dictates whether P or M helicity is more stable. In the case of the molecules studied herein, the P-type helicity conformers are more thermodynamically stable and dominate the population at equilibrium³⁰.

The molecular motor undergoes one 360° rotary cycle in four steps as shown in Figure 1.2. Early studies using low temperature photolysis and circular dichroism uncovered two important details leading to these conclusions¹⁴. Low temperature photolysis of the P-cis or P-trans only produces M-trans or M-cis, respectively. Heating of M-trans or M-cis forms P-trans or P-cis, respectively. These findings support a four-step cycle such as this: P-trans (photoisomerization) \rightarrow M-cis (helix inversion) \rightarrow P-cis (photoisomerization) \rightarrow M-trans (helix inversion) \rightarrow P-trans ... etc., as shown in Figure 1.2. This model suggests the rotary cycle of the molecular motor is unidirectional. In other words, P-trans never forms P-cis as its photoproduct and vice versa. Unidirectional rotation results from the steric interactions between the two sides of the central carbon-carbon double bond, which make the molecular motor helical.

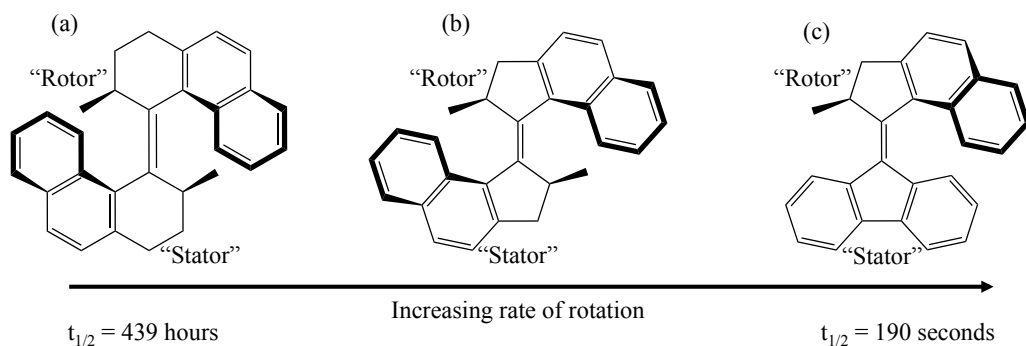


Figure 1.3. Synthetic evolution of the molecular motor. (a) Original first-generation molecular motor, relying on six membered fusing rings. The half life of the unstable cis isomer at room temperature is 439 hours^{14,31}, (b) Improved first-generation molecular motor, relying on five membered fusing rings. This is the molecule studied in chapters three and four. The half life of the unstable cis isomer is 43 minutes^{30,31}. (c) Second-generation molecular motor relying on a fluorene as the stator, the half life of the unstable conformation is 190 seconds³¹.

The barrier for thermal helix inversion governs the rate-limiting step of the rotary cycle. One of the main foci of this field of research is to increase the overall rate of rotation in the molecular motor. The primary approach to achieve rate increase is reduction of the amount of steric hindrance by synthetic modification. Thermal helix inversion activation energy decreases by alleviating the steric hindrance between the crowding functional groups of the molecule. For example, the originally reported molecular motor's M-trans to P-trans thermal helix inversion barrier was 109 kJ/mol³², while recently reported thermal helix inversion barriers are as low as 35.8 kJ/mol³³. Such decreases led to a 10^{12} fold increase in the rate of rotation at room temperature!

Pursuit of smaller and smaller thermal helix inversion barriers created a wide array of unique molecular motors, including the so-called "second-generation" molecular motor. The second-generation molecular motor is asymmetric across the carbon-carbon double bond, using a fluorene "stator" and an indene "rotor" as shown in Figure 1.3. Second-generation molecular

motors benefit from the same size thermal helix inversion barrier on either side of the stator, and fewer possible UV-vis absorption spectra. These benefits make the second-generation molecular motor a more useful molecular device and easier to systematically improve. Synthetic chemists need only concern themselves with one thermal helix inversion barrier, rather than two as with the first-generation molecular motor. It is important to keep in mind, however, the rate-limiting step in the rotary cycle of molecular motors is a *necessary* design flaw needed to induce unidirectional rotation. One can imagine as synthetic efforts continue to reduce the thermal helix inversion barrier; eventually the molecular motor will lose its helicity and its preference for unidirectional rotation. Therefore, efforts to minimize the thermal helix inversion barrier will eventually lose their benefits. As the benefits of ground state synthetic modifications diminish, research is now focusing on the excited states. There is the possibility of further innovation by investigating the photoisomerization step in the rotary cycle of the molecular motor.

The excited state dynamics of the molecular motor have gone largely unnoticed until recently. This is because alkene isomerization takes place on the fs to ps timescales, many orders of magnitude faster than thermal helix inversion. The photoisomerization is nowhere near the rate-limiting step of these devices. Ultrafast fluorescence up-conversion^{34,35}, UV-vis TA³⁵⁻³⁸, and UV-pump IR probe³⁸ TA have studied the excited state dynamics of some second-generation molecular motors. Taken together, these studies demonstrate photoisomerization of the second-generation molecular motor can be understood along the lines of typical alkene photoisomerization involving ultrafast twisting motion about the central carbon-carbon bond and pyramidalization of one of those carbons to return to the ground state via a conical intersection^{16-18,39-48}.

UV-vis TA spectroscopy was carried out on a second-generation molecular motor in hexane excited by 360 nm in 2009 by Augulis et al.³⁶ The authors' analysis revealed two lifetimes, 1.7 ps and 12-16 ps, in the data. The 1.7 ps lifetime corresponds to the decay of an excited state absorption and stimulated emission. The 12 – 16 ps lifetime corresponds to the formation of photoproducts, which persist for hundreds of picoseconds after excitation. The authors interpret these results in terms of a single excited electronic state with a barrier crossing. The initial excited state crosses a barrier with a timescale of 1.7 ps. Afterwards, the molecules form metastable products via conical intersection, relaxing on a 12 – 16 ps timescale.

Fluorescence up-conversion studies were carried out on a second-generation molecular motor in dichloromethane and cyclohexane by Conyard et al.³⁴ In this work, the authors probed the dynamics of the bright excited state in the photoisomerization of the molecular motor. The fluorescence (455 – 576 nm) decays with two timescales, ranging from 110 – 310 fs and 0.87 – 1.3 ps. The blue side of the fluorescence decays much faster than the red side. The steady state fluorescence spectrum of the molecule is incredibly weak ($\Phi \approx 10^{-4}$) and broadened on the red side. Taken together, the authors concluded a large amount of structural relaxation happens in the excited state during the first ~ 100 fs after excitation. The authors detected two oscillatory features in the time resolved emission profiles with frequencies of 130 and 180 cm^{-1} . They go on to speculate π - π^* excitation leads to rapid decay from the Franck-Condon region by twisting of the central double bond and pyramidalization of one of the carbons, returning to the ground state on a ~ 1 ps timescale. However, this study was not sensitive to dark excited states, all they measured was the decay of fluorescence.

More recently, Conyard et al.^{35,37} and Amirjalayer et al.³⁸ conducted pump probe spectroscopy on a second-generation molecular motor, examining the effect of substitutions on

the molecule and the role of solvent in the excited state dynamics. These investigations reveal an additional dark excited state produced after the decay of the initial bright state. Conyard et al. showed electron donating and withdrawing groups on either side of the bridging carbon-carbon double bond could modulate the lifetime of the dark state³⁷. Amirjalayer et al. used 400 nm pump/IR probe spectroscopy and found the existence of a dark state whose lifetime is ~ 12 ps³⁸. Prior to the formation of this dark state, broad electronic transitions in the mid-infrared (~ 1500 cm⁻¹) were observed which decay on a ~ 1.5 ps timescale. This timescale was assigned to the timescale for formation of the dark state. These recent TA studies indicate the presence of two excited states involved in the photoisomerization of the second-generation molecular motor.

Theoretical calculations examining the excited state potential energy surfaces and conical intersections involved in the photochemistry have been carried out as well^{28,49-57}. These studies focus on the excited state potential energy surfaces along the twisting and pyramidalization coordinates. A wide variety of methods have been employed, including complete active space self consistent field theory (CASSCF) and complete active space second order perturbation theory (CASPT2), time dependent density functional theory (TDDFT) and state averaged spin restricted Kohn Sham theory (SA-REKS), and molecular dynamics (MD). These studies stress the importance of the twisting and pyramidalization coordinates as well as the role of two excited electronic states in the photochemical pathway.

In a 2012 study by Morukuma et al.²⁸, CASSCF and CASPT2 calculations were performed to analyze the excited state minimal energy path (MEP) of a series of sterically crowded alkenes, ranging from stilbene, to stiff stilbene, and a first-generation molecular motor. The MEP of the first-generation molecular motor is asymmetric with respect to central carbon-carbon twisting motion and very steep for twisting in one direction. This study demonstrates the effect of steric

crowding on the profile of the excited state potential energy surfaces. In 2016, Morukuma et al.⁵² used CASSCF and spin flip TDDFT (SFDFT) to locate minimal energy conical intersections for first and second-generation molecular motors, once again showing the importance of pyramidalization in the nonadiabatic decay of the excited state to the ground state.

In 2009 through 2011, Filatov et al. carried out MD simulations on the excited states of a second-generation molecular motors using DFT and SA-REKS^{49,50}, multireference methods, and surface hopping⁵¹. These investigations identified two conical intersections between the ground and excited state that are reached through twisting and pyramidalization of the central double bond. The MD simulations found the average excited state lifetime was ~ 1.4 ps with a quantum yield of $\Phi = 0.92$ for forward rotation (stable to unstable) and $\Phi = 0.4$ for reverse rotation (unstable to stable)⁵⁰. In both investigations, the authors stressed the importance of twisting and pyramidalization as the relevant reaction coordinates. Notably, these investigations fail to account for the longer timescales observed in TA measurements^{35–38}, as well as the results presented in this dissertation.

A first-generation molecular motor, (E and Z) dimethyl-tetrahydro-bi(cyclopenta[α]naphthalenyldiene), or “P-cis” and “P-trans” as shown in Figure 1.2b, was chosen as the subject of chapters three and four of dissertation for a number of reasons. Foremost, all four conformations (P-cis, M-cis, P-trans, and M-trans) have distinct UV-vis absorption spectra making them ideal for pump-repump probe (PrPP) and pump-dump probe studies featured in chapter four. In contrast, the second-generation molecular motor only has two unique UV-vis absorption spectra, making clockwise or counter-clockwise isomerization indistinguishable by TA spectroscopy. Also, this particular molecular motor has absorptions at 400 nm as shown in chapter 3 Figure 3.1, which is a convenient wavelength to

produce in the lab. Finally, it is easily synthesized based on a small number of well-established techniques reported in the literature^{30,58-60}. The TA studies in chapter three serve as a useful basis for understanding the PrPP and PDP experiments carried out in chapter four.

Photochromic photoacids. Photochromic molecules undergo reversible changes in their UV-vis absorption spectrum after light exposure⁶¹. This property is utilized in a diverse range of technologies from optical data storage, DNA photoswitching⁶²⁻⁶⁵, and optical control of functionalized surfaces⁶⁶⁻⁶⁸. The spiropyran/merocyanine (SP/MC) system is one of the most extensively studied and useful examples of a photochromic system⁶⁹⁻⁷⁸. In SP/MC systems, reversible switching mediated by light or heat causes the planar merocyanine (MC) to undergo ring closure forming spiropyran (SP) and vice versa. Recently, Liao et al. built on the SP/MC theme by incorporating acidic functional groups on the molecule⁷⁹⁻⁸² as well as attaching a propyl-sulfate moiety to make the molecules water soluble as shown in Figure 1.4. These new molecules experience a two unit pH drop after irradiation and reversibly revert to their less acidic MC configuration on a roughly one minute timescale. Therefore, they are “metastable” photoacids.

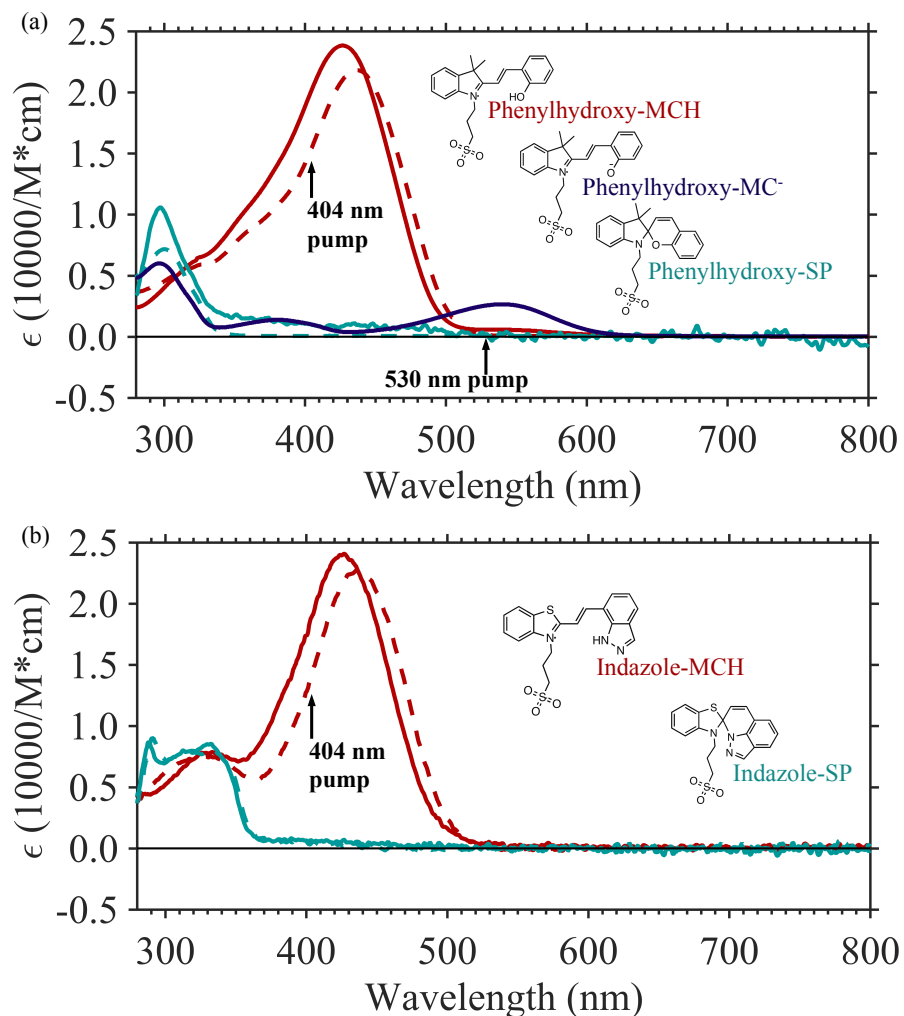


Figure 1.4. UV-vis spectra of (a) phenylhydroxy photoacid and (b) indazole photoacid in their merocyanine and spiropyran forms. The merocyanine forms are given by the red spectra, and the spiropyran forms are given by the light blue spectra. The deprotonated Phenylhydroxy-MC⁻ merocyanine (a) spectrum is in dark blue.

Conjugation lies at the heart of photochromism in SP/MC systems. The MC form consists of two aromatic groups, indoline and phenol as given in Figure 1.4a and benzothiazole and indazole in the case of Figure 1.4b. The aromatic groups are connected by a central carbon-carbon double bond allowing for delocalization of the π electrons and visible light absorption. The SP

ring-closed form has an sp^3 central carbon, which breaks the conjugation between the two sides of the molecule resulting in a blue shift of the absorption into the UV^{61,70,73,83}.

The equilibrium stability and photochemistry of SP/MC systems are governed by substitutions and solvent polarity^{71,73,75,76,78,81,83,84}. In the case of 6,8-dinitro-benzopyran indoline (6,8-dinitro-BIPS) is predominantly in the MC form in solution at room temperature. In contrast, 6-nitro-benzopyran indoline (6-nitro-BIPS) is predominantly in the SP form in solution at room temperature. 6,8-dinitro-BIPS ring opening proceeds only through singlet states^{72,74,76,84–88}. 6-nitro-BIPS will ring-open upon irradiation, but the MC form has no quantum yield for ring closure⁷⁶. In the case of un-substituted spiropyran, the equilibrium is shifted toward SP and the ring opening involves only singlet states⁸⁵.

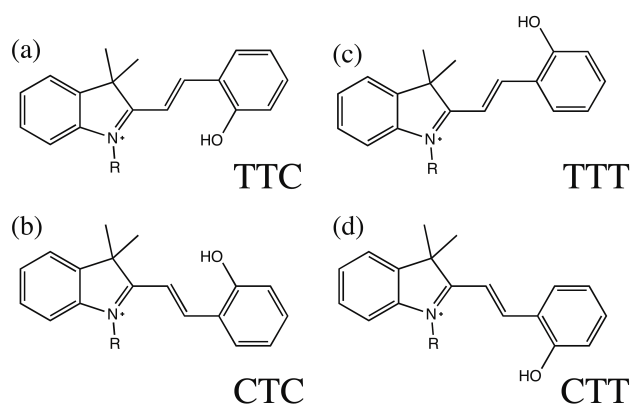


Figure 1.5. trans-phenylhydroxy-MCH conformers, similar conformers are possible for indazole-MCH as well. R group is propyl-sulfate in TA experiments, R group is CH_3 in DFT calculations.

There are four conformations of trans-MC in the ground state as shown in Figure 1.5, corresponding to rotation of functional groups on either side of the trans central carbon-carbon bond. The dominant species in most cases are TTC and TTT^{72,75,76,83,84}. The cis-MC conformers are not stable and exist as intermediates in the formation of SP.

Computational and spectroscopic studies show at least two *trans*-MC species present in solution at room temperature^{72,75,76,83,84}.

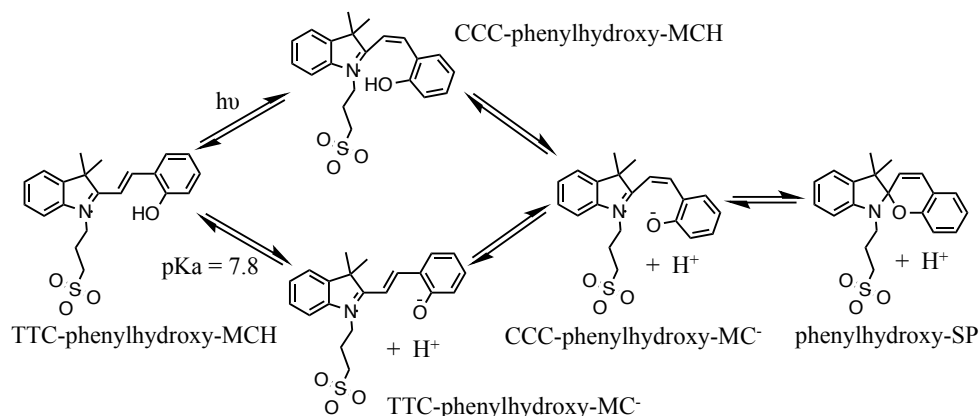


Figure 1.6. Proposed scheme of photoswitching by *trans*-phenylhydroxy-merocyanine (MCH) to phenylhydroxy-spiropyran (SP). This scheme is adapted from “Long-Lived Photoacid Based upon a Photochromic Reaction” by Liao et al.⁷⁹

Professor Yi Liao’s group synthesized the MC molecules studied in this work. Their work demonstrates SP/MC photoacids’ ability to catalyze esterification reactions and modulate the volume of pH sensitive polymers⁷⁹. Also, the group proposed their utility for studies of proton transfer processes in biological assays⁸². These photochromic photoacids are novel modifications of the SP/MC system because they are water-soluble and the SP form releases a proton after ring-closure, decreasing the pH two units. Figure 1.6 depicts the scheme put forth by Liao et al. for the photoswitching mechanism of phenylhydroxy-MCH/SP⁷⁹. The *trans*-phenylhydroxy-MCH species dominates the solution at room temperature. Irradiation of the phenylhydroxy-MCH with visible light produces phenylhydroxy-SP in steady state photolysis^{79–82}. Phenylhydroxy-SP is formed by ring closure of phenylhydroxy-MCH, and afterwards phenylhydroxy-SP ring-opens in the dark to reform phenylhydroxy-MCH with a

half-life of ~ 70 seconds in water at room temperature. This points to a pathway on the ground state connecting *trans*-phenylhydroxy-MCH to phenylhydroxy-SP. In addition, the phenylhydroxy-MCH has a pKa of 5.5 and exists in a protonated acid state or a deprotonated conjugate base state depending on the pH. Recently, Liao et al. developed a metastable photoacid functioning at physiological pH 7.4 by replacing the phenol with a less acidic indazole functional group⁸². Little is known about the photoswitching mechanism of such water-soluble SP/MC systems⁷⁷.

In chapter five, the excited state dynamics and photoproducts formed in the photoactivated ring closure of phenylhydroxy-MCH/SP and indazole-MCH/SP were investigated by a combination of femtosecond UV-vis TA spectroscopy and density functional theory (DFT). The key findings show that photoexcitation of indazole-MCH in phosphate buffered saline (PBS) or dimethylsulfoxide (DMSO) produces a long-lived photoproduct on a ~ 30 ps timescale, consistent with formation of indazole-SP. Steady state photolysis of phenylhydroxy-MCH in pH 5.5 citrate buffer or DMSO promptly produces phenylhydroxy-SP. However, TA results for the phenylhydroxy-MCH are solvent dependent. In pH 5.5 citrate buffer, photoproducts with red-shifted absorption form on a ~ 10 ps timescale and persist for $\gg 3.5$ ns. Time dependent DFT (TDDFT) calculations support the assignment of this long-lived species to deprotonated *cis* phenylhydroxy-MC⁻. In DMSO, the phenylhydroxy-MCH forms a long-lived photoproduct on a ~ 50 ps timescale which persists for $\gg 3.5$ ns, consistent with the formation of either a protonated *cis* isomer or phenylhydroxy-SP.

Hydroxocobalamin and aquocobalamin. Vitamin B₁₂ is a cobalt-centered corrin ring with a dimethylbenzimidazole lower axial ligand and a variable upper axial ligand as shown in Figure 1.1. There are many derivatives of vitamin B₁₂ each with different chemical and

photochemical properties largely governed by the nature of the upper axial ligand. The vitamin B₁₂ derivatives can be divided into two categories: alkylcobalamins, whose upper axial ligand is an alkyl group, and non-alkylcobalamins, whose upper axial ligand is a non-alkyl group. The alkylcobalamins, methylcobalamin (MeCbl) and adenosylcobalamin (AdoCbl) are the enzymatically active forms, functioning as co-factors to a wide array of enzymes⁸⁹⁻⁹³. Many alkylcobalamins undergo Co-C homolysis to form cob(II)alamins and alkyl radicals after photoexcitation⁹⁴⁻⁹⁸. In contrast, the non-alkylcobalamins, such as cyanocobalamin (CNCbl), hydroxocobalamin (HOCbl), aquocobalamin (H₂OCbl) are biologically inert and less photolabile^{96,98-101}.

Although there are a wide number of B₁₂ derivatives, their UV-vis spectra have similar features. This is because the UV-vis spectra are dominated by π - π^* transitions of the corrin ring¹⁰²⁻¹⁰⁷. The π system of non-planar ring interacts with the cobalt axial ligands. Therefore, the UV-vis spectra of various B₁₂ derivatives are sensitive to the nature of the axial ligands. Three general spectral features characterize the UV-vis spectra: the $\alpha\beta$ band (~ 525 nm), the DE band (~ 400 nm), and the γ band (~ 350 nm). Non-alkylcobalamins such as CNCbl, HOCbl, and H₂OCbl display “typical” UV-vis spectra, with narrow γ band transitions. Alkyl-cobalamins such as AdoCbl and MeCbl display “unique” UV-vis spectra with broad γ band transitions composed of at least three peaks as shown in Figure 1.6. Cob(II)alamin, the radical product of cobalt/upper ligand homolysis, has an $\alpha\beta$ band which is centered at 475 nm^{89,91,94,95,97,101,108,109}. The UV-vis spectra of these molecules are sensitive to ligation and oxidation state, making UV-vis an excellent technique for studying cobalamin photochemistry.

Many B₁₂ dependent enzymes have been studied extensively. For example, Glutamate mutase uses adenosylcobalamin as its co-factor to catalyze radical rearrangement

reactions^{89,92,93,97,101}. Methionine synthase uses methylcobalamin as its co-factor and catalyzes methyl transfer reactions^{89,101}. Previous ultrafast studies in our lab investigated the effect of the enzyme environment on the photochemistry of AdoCbl in glutamate mutase⁹⁷. More recently, CarH has attracted interest because it behaves as a photoswitch regulating the expression of carotenoid synthesis genes. CarH utilizes the photolability of its co-factor AdoCbl to function as a photoswitch¹¹⁰.

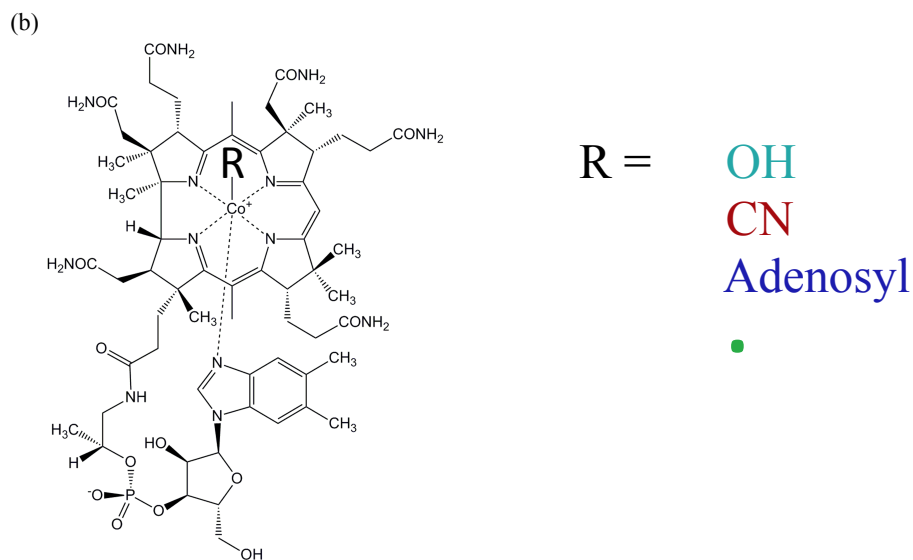
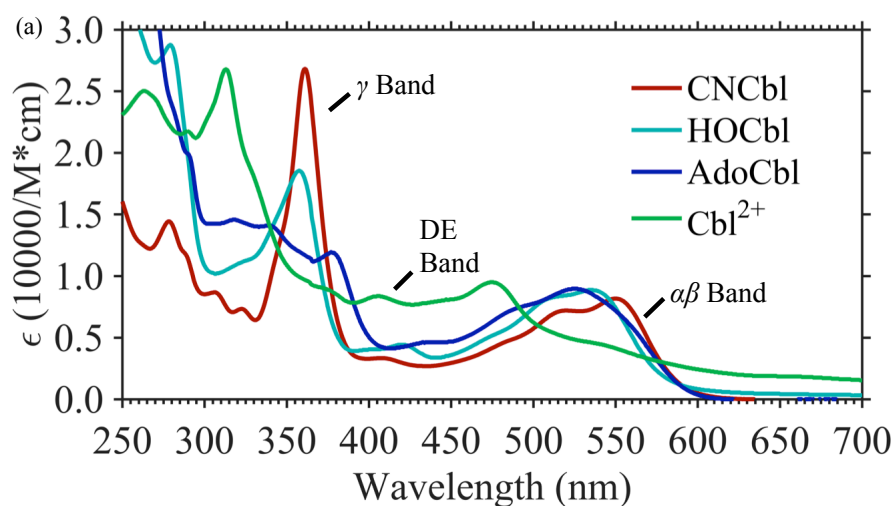


Figure 1.7. (a) UV-vis spectra of cyanocobalamin (red), hydroxocobalamin (light blue), adenosylcobalamin (dark blue), cob(II)alamin (green), and (b) the corresponding structures

Recently, work by Miller et al.¹¹¹ targeted novel cobalamin derivatives, phenylethylcobalamin (PhEtyCbl) and 4-ethylphenylcobalamin (EtPhCbl), as potential light activated drug delivery agents. These derivatives are metabolically inert “antivitamins”, being transported through the body without being utilized as enzymatic co-factors^{112,113}. In principle, the ligand of the antivitamin can be released by photolysis, delivering drugs to targeted areas in the body where the antivitamin has accumulated. Exposing only the desired tissues to light would control the release of the drug to only diseased areas. These studies challenge the alkyl- versus non-alkylcobalamin photostability paradigm⁹⁸, as the antivitamin PhEtyCbl is photostable. TA data indicates PhEtyCbl decays to its ground state on a ~ 60 ps timescale by crossing a ~ 13 kJ/mol barrier to internally convert to the ground state. These studies are laying the ground-work for using cobalamin derivatives as photoswitchable drug delivery molecules.

Other groups suggest HOCbl and H₂OCbl are possible photocatalytic reagent delivery molecules^{114–116}. In 2011, Shell et al.¹¹⁴ demonstrated HOCbl and H₂OCbl’s ability to uncoil supercoiled DNA under aerobic conditions after light exposure, likely due to hydroxyl radical damage. This is a surprising result, since several reports^{96,98,109,117} show HOCbl and H₂OCbl are photostable after irradiation with 400 or 530 nm. Our lab carried out TA on HOCbl with 269 nm excitation and anaerobic photolysis to determine that HOCbl and H₂OCbl undergo homolytic bond cleavage to form Cob(II)alamin with $\sim 1\%$ quantum yield¹⁰⁰. This supports the Shell et al. finding that HOCbl and H₂OCbl can be used as a photocatalytic source of hydroxyl radicals under aerobic UV irradiation.

Thesis Outline

Chapter two - Methods. This chapter describes the techniques employed over the course of this dissertation. It starts with a detailed description of the ti:sapph laser used for the time-resolved measurements. TA and pump-repump setups are described in detail. Steady state spectroscopy techniques such as UV-vis absorption, steady state fluorescence, and low temperature photolysis and supporting techniques are described as well. The chapter ends with synthesis procedures and sample preparation of the molecular motors, photochromic photoacids, and cobalamins.

Chapter three – Transient absorption of molecular motors. This chapter encompasses an UV-vis TA study of the cis and trans isomer of a first-generation molecular motor. The molecular motor was excited with multiple wavelengths (269, 368 and 404 nm) and the anisotropy of the excited states was measured by varying the relative polarization between the pump and probe. DFT calculations and steady state spectroscopy were used to support spectral assignments made in the TA studies. This chapter lays the foundation for design and understanding of the pump-repump probe and pump-dump probe experiments on the molecular motor presented in chapter four.

Chapter four – Pump-repump probe transient absorption of molecular motors. This chapter involves re-excitation of excited states of the molecular motors with a secondary “repump” or “dump” pulse. The time delay between the pump and secondary pulse is chosen to intercept the excited state population at critical times during the course of their excited state evolution. The pump pulse in these experiments is 269 nm and the repump pulse is 404 nm.

Chapter five – Photochromic photoacids. This chapter focuses on the TA spectroscopy of novel water soluble photochromic photoacids based spiropyran and merocyanine. Water has an

unusual effect on the photoproducts produced after excitation of the phenylhydroxy photoacid. When the molecules are dissolved in anhydrous DMSO, different dynamics and photoproducts are observed. The indazole photoproduct spectrum is less sensitive to solvent. TDDFT calculations assisted in assignments of photoproducts.

Chapter six – Hydroxo- and aquocobalamin photochemistry and anisotropy. This chapter discusses the results of work published in “Photostability of Hydroxocobalamin: Ultrafast Excited State Dynamics and Computational Studies” which show a non-alkylcobalamin can be photolabile to wavelengths less than ~ 300 nm. In addition, that article clarifies previously published data about the excited state lifetimes of HOCbl. The hydroxyl group has a pKa of eight and exists as a mixture in pure water. Previous TA studies carried out in pure water have been measurements of mixtures HOCbl and H₂OCbl. This research was carried out in pH 10.5 or pH 5.5 buffers to favor $> 99\%$ of HOCbl or H₂OCbl. Different excited state lifetimes were observed for HOCbl and H₂OCbl. In addition, the relative polarizations of the pump pulses were manipulated to analyze the anisotropy of the molecules.

Chapter seven – Conclusions and future directions. This chapter will summarize the key conclusions of the dissertation and discuss future investigations of possible interest.

Notes to Chapter 1

- (1) Walker, J. E.; Saraste, M.; Runswick, M. J.; Gay, N. J. *EMBO J.* **1982**, *1* (8), 945–951.
- (2) Noji, H.; Yasuda, R.; Yoshida, M.; Kinoshita, K. *Nature*. **1997**, *386* (6622), 299–302.
- (3) Boyer, P. D. *Annu. Rev. Biochem.* **1997**, *66*, 717–749.
- (4) Vale, R. D. *Cell* **2003**, *112* (4), 467–480.
- (5) Hirokawa, N. *Science*. **1998**, *279* (5350), 519–526.
- (6) Wadhams, G. H.; Armitage, J. P. *Nat. Rev. Mol. Cell Biol.* **2004**, *5* (12), 1024–1037.
- (7) Astumian, R.; Bier, M. *Phys. Rev. Lett.* **1994**, *72* (11), 1766–1769.
- (8) Astumian, R. D. *Science*. **1997**, *276* (5314), 917–922.
- (9) Astumian, R. D. *Nat. Nanotechnology*. **2012**, *7* (11), 684–688.
- (10) Pollard, W. T.; Mathies, R. A.; Lin, S. W.; Ames, J. B. **1991**, *1* (120), 491–518.
- (11) Haupts, U.; Tittor, J.; Oesterhelt, D. *Annu. Rev. Biophys. Biomol. Struct.* **1999**, *28*, 367–399.
- (12) Zewail, A. H. *J. Phys. Chem. A* **2000**, *104* (24), 5660–5694.
- (13) Harada, N.; Koumura, N.; Feringa, B. L. *J. Am. Chem. Soc.* **1997**, *119* (31), 7256–7264.
- (14) Koumura, N.; Zijlstra, R. W.; van Delden, R. A.; Harada, N.; Feringa, B. L. *Nature* **1999**, *401* (6749), 152–155.
- (15) Koumura, N.; Geertsema, E. M.; Meetsma, A.; Feringa, B. L. *J. Am. Chem. Soc.* **2000**, *122* (48), 12005–12006.
- (16) Quenneville, J.; Martinez, T. J. *J. Phys. Chem. A* **2003**, *107*, 829–837.
- (17) Repinec, S. T.; Sension, R. J.; Szarka, A. Z.; Hochstrasser, R. M. *J. Phys. Chem.* **1991**, *95* (8), 10380–10385.

- (18) Sension, R. J.; Repinec, S. T.; Hochstrasser, R. M.; Szarka, A. Z. *J. Phys. Chem.* **1991**, *95* (25), 10380–10385.
- (19) Chang, C. W.; Lu, Y. C.; Wang, T. Te; Diao, E. W. G. *J. Am. Chem. Soc.* **2004**, *126* (32), 10109–10118.
- (20) Bandara, H. M. D.; Burdette, S. C. *Chem. Soc. Rev.* **2012**, *41* (5), 1809–1825.
- (21) Cembran, A.; Bernardi, F.; Garavelli, M.; Gagliardi, L.; Orlandi, G. *J. Am. Chem. Soc.* **2004**, *126* (10), 3234–3243.
- (22) Velema, W. A.; Szymanski, W.; Feringa, B. L. *J. Am. Chem. Soc.* **2014**, *136* (6), 2178–2191.
- (23) London, G.; Chen, K. Y.; Carroll, G. T.; Feringa, B. L. *Chem. Eur. J.* **2013**, *19* (32), 10690–10697.
- (24) Chiang, P. T.; Mielke, J.; Godoy, J.; Guerrero, J. M.; Alemany, L. B.; Villagómez, C. J.; Saywell, A.; Grill, L.; Tour, J. M. *ACS Nano* **2012**, *6* (1), 592–597.
- (25) Chu, P. L. E.; Wang, L. Y.; Khatua, S.; Kolomeisky, A. B.; Link, S.; Tour, J. M. *ACS Nano* **2013**, *7* (1), 35–41.
- (26) Garcia-Lopez, V.; Jeffet, J.; Kuwahara, S.; Martin, A. A.; Ebenstein, Y.; Tour, J. M. *Org. Lett.* **2016**, *18* (10), 2343–2346.
- (27) Saywell, A.; Bakker, A.; Mielke, J.; Kumagai, T.; Wolf, M.; García-López, V.; Chiang, P. T.; Tour, J. M.; Grill, L. *ACS Nano* **2016**, *10* (12), 10945–10952.
- (28) Liu, F.; Morokuma, K. *J. Am. Chem. Soc.* **2012**, *134* (10), 4864–4876.
- (29) Browne, W. R.; Feringa, B. L. *Mol. Switch. Second Ed.* **2011**, *1*, 121–179.
- (30) Ter Wiel, M. K. J.; Van Delden, R. A.; Meetsma, A.; Feringa, B. L. *J. Am. Chem. Soc.* **2003**, *125* (49), 15076–15086.
- (31) Klok, M.; Browne, W. R.; Feringa, B. L. *Phys. Chem. Chem. Phys.* **2009**, *11* (40), 9124–9131.
- (32) Pollard, M. M.; Klok, M.; Pijper, D.; Feringa, B. L. *Adv. Func. Mat.* **2007**, *17* (5), 718–729.
- (33) Klok, M.; Boyle, N.; Pryce, M. T.; Meetsma, A.; Browne, W. R.; Feringa, B. L. *J. Am. Chem. Soc.* **2008**, *130* (32), 10484–10485.

- (34) Conyard, J.; Addison, K.; Heisler, I. A.; Cnossen, A.; Browne, W. R.; Feringa, B. L.; Meech, S. R. *Nat. Chem.* **2012**, *4* (7), 547–551.
- (35) Conyard, J.; Stacko, P.; Chen, J.; McDonagh, S.; Hall, C. R.; Laptanok, S. P.; Browne, W. R.; Feringa, B. L.; Meech, S. R. *J. Phys. Chem. A* **2017**, *121* (10), 2138–2150.
- (36) Augulis, R.; Klok, M.; Feringa, B. L.; Van Loosdrecht, P. H. M. *Phys. Status Solidi Curr. Top. Solid State Phys.* **2009**, *6* (1), 181–184.
- (37) Conyard, J.; Cnossen, A.; Browne, W. R.; Feringa, B. L.; Meech, S. R. *J. Am. Chem. Soc.* **2014**, *136* (27), 9692–9700.
- (38) Amirjalayer, S.; Cnossen, A.; Browne, W. R.; Feringa, B. L.; Buma, W. J.; Woutersen, S. *J. Phys. Chem. A* **2016**, *120* (43), 8606–8612.
- (39) Fuß, W.; Lochbrunner, S.; Müller, A. M.; Schikarski, T.; Schmid, W. E.; Trushin, S. A. *Chem. Phys.* **1998**, *232* (1–2), 161–174.
- (40) Fuß, W.; Kosmidis, C.; Schmid, W. E.; Trushin, S. A. *Angew. Chemie - Int. Ed.* **2004**, *43* (32), 4178–4182.
- (41) Fuß, W.; Kosmidis, C.; Schmid, W. E.; Trushin, S. A. *Chem. Phys. Lett.* **2004**, *385* (5–6), 423–430.
- (42) Liu, R. S. H. *Acc. Chem. Res.* **2001**, *34* (7), 555–562.
- (43) Yarkony, D. R. *Rev. Mod. Phys.* **1996**, *68* (4), 985–1013.
- (44) Yarkony, D. R. *J. Phys. Chem. A* **2001**, *105* (26), 6277–6293.
- (45) Levine, B. G.; Martínez, T. J. *Annu. Rev. Phys. Chem.* **2007**, *58*, 613–634.
- (46) Kovalenko, S. A.; Dobryakov, A. L.; Ioffe, I.; Ernsting, N. P. *Chem. Phys. Lett.* **2010**, *493* (4–6), 255–258.
- (47) Dobryakov, A. L.; Ioffe, I.; Granovsky, A. A.; Ernsting, N. P.; Kovalenko, S. A. *J. Chem. Phys.* **2012**, *137* (24).
- (48) Quick, M.; Berndt, F.; Dobryakov, A. L.; Ioffe, I. N.; Granovsky, A. A.; Knie, C.; Mahrwald, R.; Lenoir, D.; Ernsting, N. P.; Kovalenko, S. A. *J. Phys. Chem. B* **2014**, *118* (5), 1389–1402.
- (49) Kazaryan, A.; Filatov, M. *J. Phys. Chem. A* **2009**, *113* (43), 11630–11634.
- (50) Kazaryan, A.; Kistemaker, J. C. M.; Schäfer, L. V.; Browne, W. R.; Feringa, B. L.; Filatov, M. *J. Phys. Chem. A* **2010**, *114* (15), 5058–5067.

- (51) Kazaryan, A.; Lan, Z.; Schäfer, L. V.; Thiel, W.; Filatov, M. *J. Chem. Theory Comput.* **2011**, 7 (7), 2189–2199.
- (52) Li, Y.; Liu, F.; Wang, B.; Su, Q.; Wang, W.; Morokuma, K. *J. Chem. Phys.* **2016**, 145 (24).
- (53) Assmann, M.; Pérez-Hernández, G.; González, L. *J. Phys. Chem. A* **2010**, 114 (34), 9342–9348.
- (54) Sanz, C. S.; Pérez-Hernández, G.; Assmann, M.; Worth, G. A.; González, L. *Chem. Phys.* **2010**, 377 (1–3), 86–95.
- (55) Pérez-Hernández, G.; González, L. *Phys. Chem. Chem. Phys.* **2010**, 12 (38), 12279–12289.
- (56) Pang, X.; Cui, X.; Hu, D.; Jiang, C.; Zhao, D.; Lan, Z.; Li, F. *J. Phys. Chem. A* **2017**, 121 (6), 1240–1249.
- (57) Torras, J.; Rodríguez-Ropero, F.; Bertran, O.; Alemán, C. *J. Phys. Chem. C* **2009**, 113 (9), 3574–3580.
- (58) Mcmurry, J. E. *Chem. Rev.* **1989**, 89 (0), 1513–1524.
- (59) Takeda, A.; Tsubouchi, A. In *Houben-Weyl methods of molecular transformations*. Georg Thieme: Stuttgart, Germany; 2009; Vol. 47a, pp 247–325.
- (60) Oelgemöller, M.; Frank, R.; Lemmen, P.; Lenoir, D.; Lex, J.; Inoue, Y. *Tetrahedron* **2012**, 68 (21), 4048–4056.
- (61) Bouas-Laurent, H.; Dürr, H. In *Photochromism : Molecules and systems*; Elsevier; 2003.
- (62) Andersson, J.; Li, S. M.; Lincoln, P.; Andréasson, J. In *Chemistry of Nucleic Acid Components*; 2008; Vol. 10, pp 305–306.
- (63) Andersson, J.; Li, S.; Lincoln, P.; Andréasson, J. *J. Am. Chem. Soc.* **2008**, 130 (36), 11836–11837.
- (64) Hammarson, M.; Andersson, J.; Li, S.; Lincoln, P.; Andréasson, J. *Chem. Commun.* **2010**, 46 (38), 7130–7132.
- (65) Beyer, C.; Wagenknecht, H. A. *Synlett* **2010** (9), 1371–1376.
- (66) Rosario, R.; Gust, D.; Hayes, M.; Jahnke, F.; Springer, J.; Garcia, A. A. *Langmuir* **2002**, 18 (21), 8062–8069.

- (67) Rosario, R.; Gust, D.; Garcia, A. A.; Hayes, M.; Taraci, J. L.; Clement, T.; Dailey, J. W.; Picraux, S. T. *J. Phys. Chem. B* **2004**, *108* (34), 12640–12642.
- (68) Klajn, R. *Chem. Soc. Rev.* **2014**, *43* (1), 148–184.
- (69) Tamai, N.; Miyasaka, H. *Chem. Rev.* **2000**, *100* (5), 1875–1890.
- (70) Cottone, G.; Noto, R.; Manna, G. La; Fornili, S. *Chem. Phys. Lett.* **2000**, *319*, 51–59.
- (71) Rini, M.; Holm, A. K.; Nibbering, E. T. J.; Fidder, H. *J. Am. Chem. Soc.* **2003**, *125* (10), 3028–3034.
- (72) Wohl, C. J.; Kuciauskas, D. *J. Phys. Chem. B* **2005**, *109* (47), 22186–22191.
- (73) Gomez, I.; Reguero, M.; Robb, M. A. *J. Phys. Chem. A* **2006**, *110* (11), 3986–3991.
- (74) Buback, J.; Kullmann, M.; Langhojer, F.; Nuernberger, P.; Schmidt, R.; Würthner, F.; Brixner, T. *J. Am. Chem. Soc.* **2010**, *132* (46), 16510–16519.
- (75) Buback, J.; Nuernberger, P.; Kullmann, M.; Langhojer, F.; Schmidt, R.; Würthner, F.; Brixner, T. *J. Phys. Chem. A* **2011**, *115* (16), 3924–3935.
- (76) Nuernberger, P.; Ruetzel, S.; Brixner, T. *Angew. Chemie - Int. Ed.* **2015**, *54* (39), 11368–11386.
- (77) Kohl-Landgraf, J.; Braun, M.; Özçoban, C.; Gonçalves, D. P. N.; Heckel, A.; Wachtveitl, J. *J. Am. Chem. Soc.* **2012**, *134* (34), 14070–14077.
- (78) Hammarson, M.; Nilsson, J. R.; Li, S.; Beke-Somfai, T.; Andréasson, J. *J. Phys. Chem. B* **2013**, *117* (43), 13561–13571.
- (79) Shi, Z.; Peng, P.; Strohecker, D.; Liao, Y. *J. Am. Chem. Soc.* **2011**, *133* (37), 14699–14703.
- (80) Johns, V. K.; Wang, Z.; Li, X.; Liao, Y. *J. Phys. Chem. A* **2013**, *117* (49), 13101–13104.
- (81) Johns, V. K.; Peng, P.; Dejesus, J.; Wang, Z.; Liao, Y. *Chem. - A Eur. J.* **2014**, *20* (3), 689–692.
- (82) Abeyrathna, N.; Liao, Y. *J. Am. Chem. Soc.* **2015**, *137* (35), 11282–11284.
- (83) Cottone, G.; Noto, R.; La Manna, G. *Chem. Phys. Lett.* **2004**, *388* (1–3), 218–222.
- (84) Hobley, J.; Pfeifer-Fukumura, U.; Bletz, M.; Asahi, T.; Masuhara, H.; Fukumura, H. *J. Phys. Chem. A* **2002**, *106* (10), 2265–2270.

- (85) Ernstring, N. P.; Arthen-Engeland, T. *J. Phys. Chem.* **1991**, *95* (14), 5502–5509.
- (86) Kalisky, Y.; Williams, D. J. *Chem. Phys. Lett.* **1982**, *86* (1), 91–94.
- (87) Kalisky, Y.; Orłowski, T. E.; Williams, D. J. *J. Phys. Chem.* **1983**, *87* (26), 5333–5338.
- (88) Ruetzel, S.; Diekmann, M.; Nuernberger, P.; Walter, C.; Engels, B.; Brixner, T. *J. Chem. Phys.* **2014**, *140* (22).
- (89) Banerjee, R.; Ragsdale, S. W. *Annu. Rev. Biochem.* **2003**, *72* (1), 209–247.
- (90) Frey, P. A.; Hegeman, A. D. In *Enzymatic Reaction Mechanisms*; Oxford University Press; 2007; Vol. 1.
- (91) Kräutler, B. *Biochem. Soc. Trans.* **2005**, *33* (Pt 4), 806–810.
- (92) Holloway, D. E.; Marsh, E. N. *J. Biol. Chem.* **1994**, *269* (32), 20425–20430.
- (93) Cheng, M. C.; Marsh, E. N. G. *Biochemistry* **2005**, *44* (7), 2686–2691.
- (94) Walker, L. A.; Jarrett, J. T.; Anderson, N. A.; Pullen, S. H.; Matthews, R. G.; Sension, R. *J. Am. Chem. Soc.* **1998**, *120* (29), 7286–7292.
- (95) Shiang, J. J.; Walker, L. A.; Anderson, N. A.; Cole, A. G.; Sension, R. *J. Phys. Chem. B* **1999**, *103* (47), 10532–10539.
- (96) Shiang, J. J.; Cole, A. G.; Sension, R. J.; Hang, K.; Weng, Y.; Trommel, J. S.; Marzilli, L. G.; Lian, T.; Arbor, A. *J. Am. Chem. Soc.* **2006**, *128* (3), 801–808.
- (97) Sension, R. J.; Harris, D. A.; Stickrath, A.; Cole, A. G.; Fox, C. C.; Marsh, E. N. G. *J. Phys. Chem. B* **2005**, *109* (38), 18146–18152.
- (98) Rury, A. S.; Wiley, T. E.; Sension, R. J. *Acc. Chem. Res.* **2015**, *48* (3), 860–867.
- (99) Wiley, T. E.; Arruda, B. C.; Miller, N. A.; Lenard, M.; Sension, R. J. *Chinese Chem. Lett.* **2015**, *26* (4), 439–443.
- (100) Wiley, T. E.; Miller, W. R.; Miller, N. A.; Sension, R. J.; Lodowski, P.; Jaworska, M.; Kozłowski, P. M. *J. Phys. Chem. Lett.* **2016**, *7* (1), 143–147.
- (101) Banerjee, R. *ACS Chem. Biol.* **2006**, *1* (3), 149–159.
- (102) Fugate, R. D.; Chin, C.; Song, P. *Biochim. Biophys. Acta* **1976**, *421* (1), 1–11.
- (103) Stich, T. A.; Buan, N. R.; Brunold, T. C. *J. Am. Chem. Soc.* **2003**, *125* (19), 5897–5914.

- (104) Kornobis, K.; Kumar, N.; Lodowski, P.; Jaworska, M.; Piecuch, P.; Lutz, J. J.; Wong, B. M.; Kozlowski, P. M. *J. Comput. Chem.* **2013**, *34* (12), 987–1004.
- (105) Lodowski, P.; Jaworska, M.; Kornobis, K.; Andruni, T.; Kozlowski, P. M. *J. Phys. Chem. B* **2011**, *115* (45), 13304–13319.
- (106) Lodowski, P.; Jaworska, M.; Andruniów, T.; Garabato, B. D.; Kozlowski, P. M. *Phys. Chem. Chem. Phys.* **2014**, *16* (35), 18675.
- (107) Solheim, H.; Kornobis, K.; Ruud, K.; Kozlowski, P. M. *J. Phys. Chem. B* **2011**, *115* (4), 737–748.
- (108) Buckel, W.; Golding, B. T. *Annu. Rev. Microbiol.* **2006**, 27–49.
- (109) Harris, D. A.; Stickrath, A. B.; Carroll, E. C.; Sension, R. J. *J. Am. Chem. Soc.* **2007**, *129* (24), 7578–7585.
- (110) Kutta, R. J.; Hardman, S. J. O.; Johannissen, L. O.; Bellina, B.; Messiha, H. L.; Ortiz-Guerrero, J. M.; Elías-Arnanz, M.; Padmanabhan, S.; Barran, P.; Scrutton, N. S.; Jones, A. R. *Nat. Commun.* **2015**, *6*, 7907.
- (111) Miller, N. A.; Wiley, T. E.; Spears, K. G.; Ruetz, M.; Kieninger, C.; Kräutler, B.; Sension, R. J. *J. Am. Chem. Soc.* **2016**, *138* (43), 14250–14256.
- (112) Ruetz, M.; Gherasim, C.; Gruber, K.; Fedosov, S.; Banerjee, R.; Kräutler, B. *Angew. Chemie - Int. Ed.* **2013**, *52* (9), 2606–2610.
- (113) Ruetz, M.; Salchner, R.; Wurst, K.; Fedosov, S.; Kräutler, B. *Angew. Chemie - Int. Ed.* **2013**, *52* (43), 11406–11409.
- (114) Shell, T. A.; Lawrence, D. S. *J. Am. Chem. Soc.* **2011**, *133* (7), 2148–2150.
- (115) Shell, T. A.; Lawrence, D. S. *Acc. Chem. Res.* **2015**, *48* (11), 2866–2874.
- (116) Rodgers, Z. L.; Hughes, R. M.; Doherty, L. M.; Shell, J. R.; Molesky, B. P.; Brugh, A. M.; Forbes, M. D. E.; Moran, A. M.; Lawrence, D. S. *J. Am. Chem. Soc.* **2015**, *137* (9), 3372–3378.
- (117) Jones, A. R.; Russell, H. J.; Greetham, G. M.; Towrie, M.; Hay, S.; Scrutton, N. S. *J. Phys. Chem. A* **2012**, *116* (23), 5586–5594.

Chapter 2

Experimental Methods

All of the experiments described here make use of a homebuilt femtosecond laser system to do UV-vis transient absorption (TA) spectroscopy. This chapter begins by discussing the details of the laser system and the TA system. From there more specific details concerning individual experiments will be given.

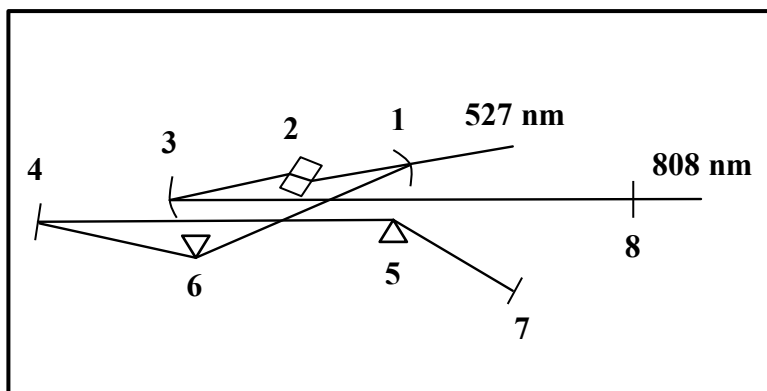


Figure 2.1. Schematic of the oscillator. (1) First curved mirror, (2) titanium:sapphire crystal, angle of incidence is Brewster's angle, (3) second curved mirror, (4) cavity folding mirror, (5) first cavity dispersion compensating prism, (6) second cavity dispersion compensating prism, (7) high reflector, and (8) output coupler.

Titanium:sapphire oscillator. In order to achieve the time resolution required by ultrafast experiments, a titanium:sapphire (ti:sapph) based solid-state laser (“the oscillator”) produces laser pulses with 20 – 30 femtosecond (fs) durations as shown in Figure 2.1. The oscillator was built from a K&M labs kit. The gain medium is pumped by the 527 nm output of a continuous wave Spectra Physics™ Millennia III laser. The ti:sapph has a broad emission spectrum centered

at ~ 800 nm, which is the key for generating fs pulses¹. The oscillator cavity is slightly detuned in the vertical axis of the cavity while in continuous wave operation to favor higher intensity modes, inducing a Kerr lens²⁻⁵. The numerous frequencies produced by the ti:sapph are brought into phase with each other by a slight disturbance of the cavity. As a result, constructive interference between the modes leads to extremely high intensities for a very brief period of time, followed by essentially zero intensity until the next pulse. Pulses emerge from the cavity with a period τ

$$\tau = \frac{2l}{c}$$

Equation 2.1

where l is the cavity length (~ 1.6 meters) and c is the speed of light (2.99×10^8 m/s). In other words, pulses emerge from the cavity after they have completed a round trip through the cavity^{3,6}. The bandwidth of the oscillator is ~ 35 nm and centered at ~ 808 nm. One can estimate the duration of these pulses using the time-bandwidth product for a Gaussian pulse,

$$\Delta\tau\Delta\omega = 0.44$$

Equation 2.2

where $\Delta\tau$ is the duration of the pulse and $\Delta\omega$ is the bandwidth of the pulse in frequency. This relationship results from the Fourier transform relationship between frequency and time of a Gaussian pulse. The duration of the pulses is ~ 25 fs if they are assumed to be Gaussian and transform limited.

Although the pulses produced by the oscillator are high intensity, they are not intense enough for the non-linear processes required for our experiments. In order to increase the intensity of the pulses a common method called chirped pulse amplification (CPA) is used. The CPA system consists of three main components: a stretcher, an amplifier, and a compressor^{7,8}. The peak

intensity of the pulses is above the damage threshold of the ti:sapph gain medium in the amplifier. The strategy used in CPA is to lengthen the pulses with a stretcher thereby decreasing their peak intensity, amplify them, and then shorten the pulses with a compressor as shown in Figure 2.2.

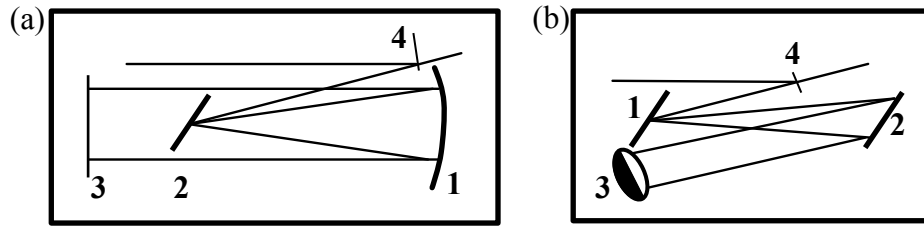


Figure 2.2. Simple diagrams of (a) stretcher and (b) compressor. For the stretcher (a), (1) $f = 500$ mm curved mirror, (2) diffraction grating, (3) flat folding mirror, and (4) pick-off mirror. For the compressor (b), (1) diffraction grating 1, (2) diffraction grating 2, (3) hollow retro mirror, (4) pick-off mirror.

The oscillator pulses are at 88 MHz but the rest of the laser system operates at 1 kHz. An electro-optic pulse picker (Quantum Technologies), consisting of a K*DP crystal in between two crossed polarizers, is used to extract one pulse per millisecond and reject the other 87,999 pulses per millisecond. The pulse picker's design is based on the static Kerr effect, where a sufficiently high voltage applied to a crystal will induce a birefringence^{3,6}. If 8 kV ($\lambda/2$ voltage) is applied to the crystal, the birefringence rotates the polarization of a pulse by 90° . The pulse picker is synchronized to the laser pulses emerging from the oscillator such that it applies the $\lambda/2$ voltage at 1 kHz kilohertz frequency for a duration of ~ 8 ns, rotating the polarization of a single pulse once a millisecond. The pulses go through the pulse picker after going through the stretcher.

The stretcher consists of a diffraction grating, a curved mirror ($f = 500$ mm), and a flat folding mirror at the focus of the curved mirror. The stretcher adds second order dispersion (“chirp”) and third order dispersion (“TOD”) to the phase of the laser pulses by creating a

wavelength dependent path length through the apparatus^{4,9}. The duration of the pulses is increased to several hundred picoseconds (ps) by adding chirp and TOD to the phase of the pulses. As a result, the peak intensity of pulses is decreased well below the damage threshold of the ti:sapph gain medium in the amplifier. This prevents damage to the gain medium during amplification.

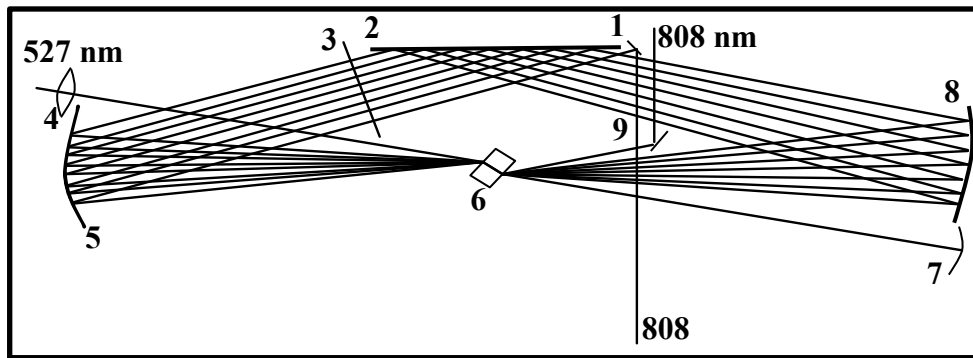


Figure 2.3. Schematic of the eight-pass amplifier. (1) Oscillator injection mirror, (2) folding mirror, (3) mask, (4) $f = 300$ mm pump laser lens, (5) $f = 500$ mm curved mirror, (6) ti:sapph gain medium, (7) $f = 500$ mm pump retro mirror, (8) $f = 500$ mm curved mirror, and (9) amplified pulse pick-off mirror.

The majority of the experiments in this work were carried out using an eight pass amplifier based on Kapetyn and Murnane's design¹⁰. The amplifier consists of a ti:sapph gain medium pumped by a Q-switched 527 nm 1 kHz 9.5 W pump laser (Quantronix Darwin), two $f = 500$ mm curved mirrors, an 11 cm flat folding mirror, and an eight holed mask as shown in Figure 2.3. The pump laser is focused by an $f = 500$ mm lens onto the ti:sapph and the stretched output of the oscillator is spatially overlapped with the pump. The oscillator output gains energy on each of the eight passes through the amplifier by stimulated emission. The ti:sapph is placed at the focus of the curved mirrors which are angled off axis by $\sim 15^\circ$ to direct the beam at the 11 cm folding mirror. The mask is inserted in the beam path to reduce amplified spontaneous

emission caused by the pump laser. After eight passes through the gain medium, the pulse energy has increased from ~ 10 nJ to ~ 1.1 mJ, and the beam is extracted from the amplifier by a pick-off mirror which is carefully set to only intersect the eighth pass. Then the beam is sent to the compressor.

The compressor's purpose is to remove the chirp and TOD induced by the stretcher and any dispersion caused by passing through various optics in the beam path. The compressor consists of two parallel diffraction gratings and a hollow retro mirror as shown in Figure 2.2. Similar to the stretcher, the compressor creates a wavelength dependent path length. Tunable amounts of dispersion can be added to the pulse by choosing the angle of incidence on the gratings and the separation between the gratings. Once the pulses are compressed, they are ready for experiments in the TA setup.

Transient absorption. TA measurements were performed using two different home built Ti:Sapphire laser systems of similar design as depicted in Figure 2.3, relying on either an eight-pass amplifier or a regenerative amplifier/two-pass post amplifier combination. TA is expressed as:

$$\Delta A(\lambda, t) = A_{pumpON} - A_{pumpOFF} = \log\left(\frac{I_{pumpON}}{I_{o,pumpON}}\right) - \log\left(\frac{I_{pumpOFF}}{I_{o,pumpOFF}}\right) = \log\left(\frac{I_{pumpON}}{I_{pumpOFF}}\right)$$

Equation 2.3

as long as one assumes that $I_{o,pumpON}$ is equal to $I_{o,pumpOFF}$. In order to measure the TA of a sample, one must have a pump pulse, a probe pulse, and a method for achieving relative time delays between the two¹¹.

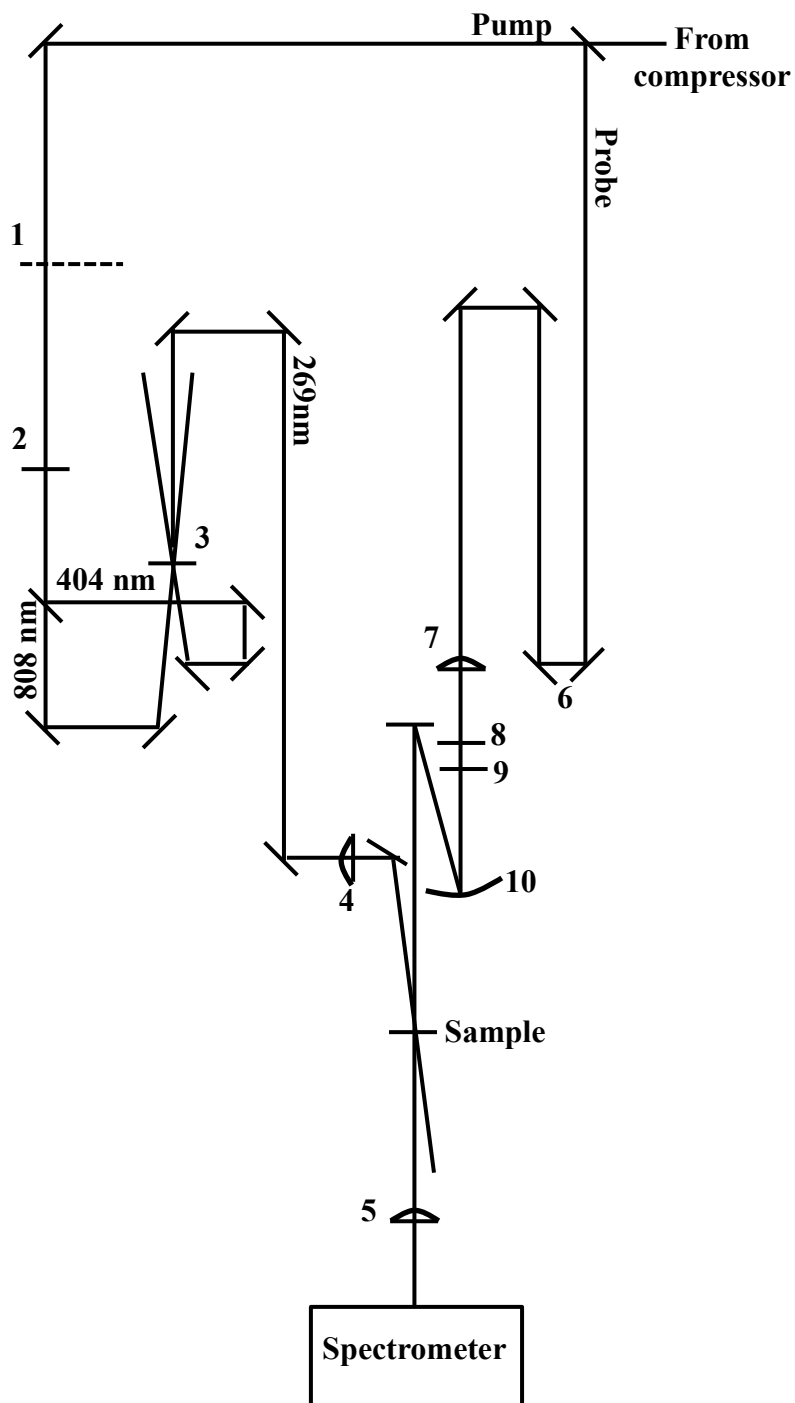


Figure 2.4. Schematic of the TA setup. (1) Optical chopper, (2) SHG BBO crystal, (3) THG BBO crystal, (4) $f = 250$ mm pump focusing lens, (5) $f = 90$ mm quartz achromatic lens, (6) computer controlled delay line, (7) $f = 100$ mm lens, (8) 5 mm thick CaF_2 window, (9) either KG3 filter or nickel sulfate filter, (10) $f = 500$ mm curved aluminum mirror.

The laser fundamental (808 nm) of the CPA system is capable of multiple non-linear optical processes, such as second and third harmonic generation, self-phase modulation, and optical parametric amplification¹². As a result, multiple pump wavelengths and probe ranges can be achieved. The second harmonic of the fundamental (404 nm) pump is generated in beta barium borate (BBO), the third harmonic (269 nm) pump is the sum-frequency of the fundamental and second harmonic in BBO, and wavelengths from 500 – 700 nm are produced in a home-built two stage noncollinear optical parametric amplifier^{13–15}. The pump pulse intensity (J/cm²) is kept at a level where 10% or less of the sample molecules in the pump focus are excited. This can be estimated by:

$$P_{ex} = \frac{\textit{photons}_{\textit{absorbed}}}{\textit{molecules}_{\textit{in focus}}}$$

Equation 2.4

where $\textit{photons}_{\textit{absorbed}}$ is the percentage of absorbed photons per pump pulse and $\textit{molecules}_{\textit{in focus}}$ is the number of molecules in the pump focus given the sample concentration and diameter of the pump beam at the sample. For isotropic measurements, the pump polarization is kept at magic angle (54.7°) with respect to the probe polarization by rotation with a half-waveplate. Every other pump pulse is blocked by a synchronized optical chopper (Thorlabs™ M1000) inserted in the beam, rotating at 500 Hz. The chopper blocks every other pump pulse, allowing differentiation between the “Pump ON” and “Pump OFF” probe pulses.

The probe utilized in all experiments is a broad-band continuum resulting from self-phase modulation occurring in a 5 mm CaF₂ window. The continuum spans from either ~ 325 – 800 nm (“visible continuum”) or ~ 270 – 600 nm (“UV continuum”) depending on whether the fundamental of the laser or the second harmonic of the laser, respectively, is employed. In both cases, the CaF₂ is continuously linearly translated in the Fourier plan of the beam at a slow

frequency, approximately 1 Hz. Continuous translation is critical for preventing optical damage to the CaF₂ window. A 1 mW beam with a 6 mm diameter is focused with an $f = 100$ mm fused silica lens into the CaF₂ window to generate the continuum. In the case of visible continuum, a KG3 filter after the CaF₂ absorbs the residual 808 nm from the continuum. In the case of UV continuum, a 1 mm path length quartz cuvette filled with saturated nickel sulfate is placed in the beam after the CaF₂ to absorb residual 404 nm. A neutral density filter ensures the probe energy is ~ 15 nJ. An $f = 500$ mm concave aluminum mirror focuses the continuum on the sample to a spot size of ~ 70 μm . The pump spot size is kept around 150 μm . The pump and probe are spatially overlapped in the sample with a 200 μm pinhole.

Relative time delays between the pump and probe are achieved by increasing the relative path length between the pump and probe. The instrument alters the length of the probe arm prior to continuum generation by using a computer controlled delay stage (NewportTM ESP300). “Time zero” is the configuration of the instrument in which the pump and probe beams have equal path lengths and arrive at the sample at the same time. Step sizes are kept between 20 and 30 fs around time zero to accurately determine the instrument response function. The probe is “chirped” such that the high frequencies in the continuum arrive at the sample ~ 1.8 ps prior to the low frequencies. As a result, fine time steps are necessary for ~ 1.8 ps around time zero. The step sizes increase exponentially with time delay. This scheme is employed to prevent the experiments from taking too long.

Several experiments in chapters three, five, and six require excitation wavelengths other than the second (404 nm) or third (269 nm) harmonic of the laser. Such experiments make use of a home built two-stage non-collinear optical parametric amplifier (NOPA). In the first stage, a 404 nm “pump” beam parametrically amplifies certain frequencies of a visible continuum by

phase matching with the continuum in a BBO crystal, crossing at an *internal* angle of $\sim 6.7^\circ$. This produces a signal pulse and an idler pulse. The first stage produces signal pulses that are $\sim 1 \mu\text{J}$. The signal pulse is then selected for further amplification in the second stage of the NOPA by a similar scheme as stage one. Stage two typically produces a signal with $\sim 7 \mu\text{J}$ per pulse. The NOPA is tunable across 500 – 700 nm. The experiments featured in chapter three, using 368 nm as the pump wavelength made use of a high power frequency doubled NOPA in the Laboratory for Ultrafast Multidimensional Optical Spectroscopy (LUMOS).

Sample delivery to the pump and probe pulses is achieved by two main methods: thin walled quartz flow cell or wire guided flow. Samples are continuously refreshed between laser shots by flowing with a peristaltic pump to prevent contamination of the signal by photoproducts produced by the previous laser pulse. 1 mm quartz flow cells (NSGTM, StarnaTM, FireflySciTM) are connected to a sample reservoir by chemically resistant tubing. The wired guided flow produces a $\sim 300 \mu\text{m}$ thick sheet of sample between two parallel $300 \mu\text{m}$ steel rods held in place TeflonTM swaglokTM at a nominal spacing of 5 mm. The wired guided flow is useful in reducing pump scatter and self phase modulation occurring in the walls of a flow cell. However, the wire guided flow requires a very concentrated sample due to its short path length and is not compatible with volatile solvents.

The probe is measured after interacting with the pump in the sample with an Avantes AvaspecFast CCD 16-bit detector operating at 1 kHz, sensitive from 195 – 950 nm. The probe is focused by a quartz achromatic lens ($f = 90 \text{ mm}$) onto a fiber optic coupled to the spectrometer. The spectrometer consists of an $f = 75 \text{ mm}$ Czerny-Turner with $50 \mu\text{m}$ entrance slit and a 1350 pixel detector. Typically, 800 probe spectra are collected per time point and averaged to create a TA (ΔA) spectrum.

$$\Delta A(\lambda, t) = \log \left(\frac{\langle I_{on} \rangle}{\langle I_{off} \rangle} \right)$$

Equation 2.5

The experiment and instrument are controlled by custom software written in LabVIEW™.

Typically, 4-10 scans are taken during an experiment for averaging. The direction of the delay stage is reversed every other scan to minimize systematic drifts occurring from improper alignment up and down the delay stage.

Time zero in the raw data is wavelength-dependent, resulting from the chirp of the probe as mentioned previously. The chirp is removed from the data by fitting its profile to a third order polynomial and interpolating the data onto a new time grid. The chirp corrected data are analyzed by a global analysis program, either written in the lab, or “Glotaran”, a open-source global fitting program^{16,17}. The data are fit to a sum of exponential decays with associated amplitudes and a time independent amplitude. The amplitudes resulting from the fit, decay associated difference spectra (DADS), can be transformed into species associated difference spectra (SADS) if one assumes a particular kinetic model. The procedure for the DADS to SADS transformation is described below.

$$\begin{aligned} \frac{dA}{dt} &= -k_1 A(t) \\ \frac{dB}{dt} &= +k_1 A(t) - k_2 B(t) \\ \frac{dC}{dt} &= +k_2 B(t) - k_3 C(t) \\ \frac{dD}{dt} &= +k_3 C(t) - k_4 D(t); k_4 \rightarrow 0 \end{aligned}$$

Where A, B, C and D are the species in a sequential kinetic model ($A \rightarrow B \rightarrow C \rightarrow D$) and k_1, k_2, k_3, k_4 , are the rates for each reaction. This system of coupled linear first order differential equations can be written in matrix form.

$$\dot{\vec{N}} = \begin{bmatrix} \dot{A} \\ \dot{B} \\ \dot{C} \\ \dot{D} \end{bmatrix}, \vec{N}(t) = \begin{bmatrix} A(t) \\ B(t) \\ C(t) \\ D(t) \end{bmatrix}, \text{ and } \mathbf{K} = \begin{bmatrix} -k_1 & 0 & 0 & 0 \\ k_1 & -k_2 & 0 & 0 \\ 0 & k_2 & -k_3 & 0 \\ 0 & 0 & k_3 & -k_4 \end{bmatrix}$$

This system of equations can be solved by diagonalizing \mathbf{K} .

$$D = C^{-1}KC$$

Where D is the eigenvalue matrix of \mathbf{K} , C is the eigenvector matrix of \mathbf{K} . The general solution to the system of equations is solved by:

$$\vec{N}(t) = Ce^{Dt}C^{-1}\vec{N}(t=0)$$

Where $N(t=0)$ is the initial conditions of the problem, usually assuming 100% population as species A initially. The species associated difference spectra (SADS) can be produced by:

$$SADS = DADS \times ((C^{-1}N(t=0))_{n,n})^{-1} \times C^{-1}$$

Where $(C^{-1}N(t=0))_{n \times n}$ has the elements of the product of C^{-1} and $N(t=0)$ on the diagonal of a square matrix.

Pump-repump. A pump-repump TA spectrometer was developed in the lab based on existing designs¹⁸⁻²¹. Pump-repump and pump-dump data ($\Delta\Delta A$) are generally expressed as double differences

$$\Delta\Delta A(\lambda, t) = \Delta A(\lambda, t)_{\text{pump\&repump}} - \Delta A(\lambda, t)_{\text{pump}} - \alpha * \Delta A(\lambda, t)_{\text{repump}}$$

Equation 2.6

This allows subtractions of background signals resulting from either the single pump pulse or single repump/dump pulse. If there is ground state absorption of the sample by the repump, a scale factor α may be necessary to account for the percent of ground state molecules excited by the pump (equation 2.4) in the $\Delta A_{\text{pump\&repump}}$ signal. These experiments require an additional

delay stage to set a relative time delay between the pump and repump. An additional chopper is necessary to expedite the data collection process. If the 500 Hz pump chopper is triggered by the output of the 250 Hz repump chopper, then enough data for a $\Delta\Delta A$ signal is acquired every four probe pulses as shown in Figure 2.5. All of the details regarding the pump, probe and spectrometer hold true for the pump-repump instrument.

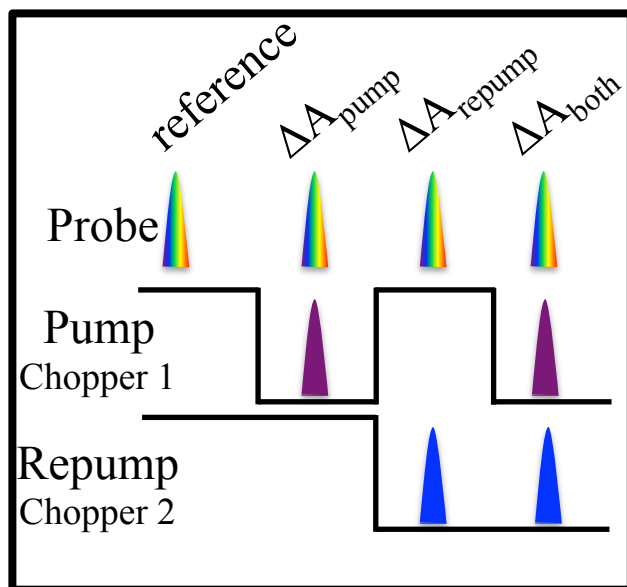


Figure 2.5. Schematic of the two synchronized pump and repump choppers. The pump chopper operates at 500 Hz, the repump chopper operates at 250 Hz, and the unchopped probe functions at 1 kHz. The three needed TA signals are acquired every four shots of the probe. Thus, the reference (pump OFF) for each signal is acquired first, then pump ON, then repump ON, the pump and repump ON.

Steady state measurements. A Shimadzu UV-2600 dual beam scanning UV-vis spectrometer was used throughout the course of this research. In addition, a Horiba Fluoromax 3 scanning spectrofluorometer was used to acquire steady state emission spectra. The fluorescence measurements used 5 nm entrance and exit slits, a 0.1 second integration time, and 1 nm step size.

Molecular motors synthesis. Synthesis of the molecular motors studied in chapters three and four was based on published procedures, using the well-known McMurry coupling^{22–25} and a pictorial scheme of the synthesis is given in Figure 2.6. Two grams of 99.6% pure

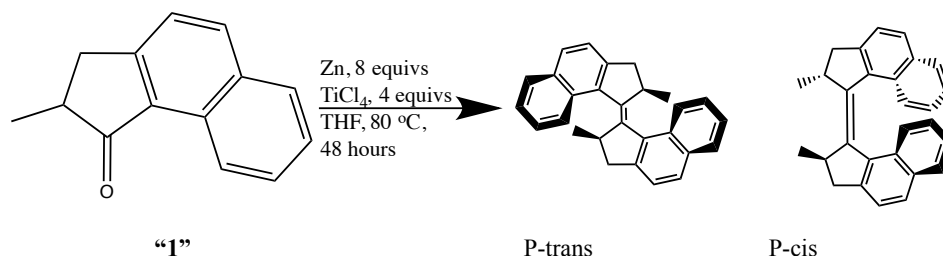


Figure 2.6. Synthesis scheme for McMurry coupling to form both the cis and trans molecular motor isomers.

2,3-dihydro-2-methyl-1H-benz(e)inden-1-one ("1") were purchased from GLSyntech and used without further purification. Zinc dust, tetrahydrofuran (THF), and titanium (IV) chloride were purchased from Sigma-Aldrich and used without further purification. Titanium (IV) chloride reacts violently with water and oxygen, so great care was taken to keep the system dry and under N₂ atmosphere. To a 0 °C, three-necked 250 mL round bottom flask (RBF), 3.2962 grams (0.05042 moles, eight equivalents) of zinc dust was added, along with a stir bar. To the middle neck of the RBF, a reflux condenser was attached. A side neck of the RBF was capped with a rubber septum, while the third neck was attached to a schlenk line. An additional schlenk line was attached to the top of the reflux condenser. The atmosphere in the RBF was evacuated and back-filled with dry nitrogen three times, and ~ 30 mL of freeze pump thawed THF were syringed into the flask to form a greyish-black slurry. Titanium (IV) chloride (2.82 mL, 0.02521 moles, four equivalents) of was syringed drop wise onto the slurry, causing egg-yolk yellow fumes to evolve from each drop. The reagent was allowed to reflux for two hours at 80 °C, turning the slurry slightly bluish-grey. A solution of 2.3 grams (0.0061 moles, one

equivalent) **1** in 20 mL FPT THF was prepared and syringed onto the reagent in a drop wise fashion. The solution was allowed to stir and reflux for 48 hour and turned completely black. The RBF was brought to room temperature and the rubber septum was removed and ~ 100 mL of saturated aqueous ammonium chloride was added to neutralize any remaining reagent. The crude was extracted three times with ethyl acetate and the organic layer was collected, dried over sodium sulfate, and crudely filtered through a small (5 x 0.5 cm) silica gel column and ethyl acetate. The solvent was removed under reduced pressure. The remaining solids weighed 1.702 grams, giving a 74% crude yield.

Thin layer chromatography on a silica plate with 10:1 heptane to ethyl acetate of the reaction crude indicated **1** was consumed completely in the reaction. The products have an R_f of 0.29. Further purification of the solids was carried out with a silica gel column and 10:1 heptane to ethyl acetate ratio as the mobile phase, yielding 1.4190 grams (62% yield). The cis isomer was recrystallized in ethyl acetate at -20 °C and the trans isomer was recrystallized through repeated recrystallizations with ethyl acetate and ethanol (1:1) at -20 °C.

In order to verify the structures of the cis and trans isomers, mass spectra were collected for each sample, giving a parent peak of 360.5 amu, the molar mass of the molecules. Nuclear magnetic resonance (NMR) spectra were collected as well and are in agreement with published NMR spectra of the two isomers^{24,26}. The UV-vis spectra of the samples were collected and are in good agreement with published spectra as seen in chapter three Figure 3.1^{24,26}. Fluorescence spectra of the samples were collected and are shown in chapter three Figure 3.1.

In order to obtain UV-vis spectra of the unstable M-cis and M-trans isomers, low temperature (-30 °C) photolysis was performed on the P-cis and P-trans molecules in heptane. The samples were kept in a sealed insulated container with fiber optics inserted into the container for

collecting UV-vis spectra. The container was filled with a dry ice/isopropanol bath to maintain a -30 °C temperature and dry nitrogen was continuously blown over the sample to prevent frost formation. The samples were exposed to the output of a 450 W Xe arc lamp for 30 second intervals until no further changes were observed in the UV-vis spectra. This process took approximately 10 minutes.

Cis and trans molecular motors samples were prepared in heptane or 2-butanol for TA measurements. Sample concentrations were chosen to produce an optical density of ~ 0.5 in a 1 mm sample cell. The sample volumes were kept around 100 – 150 mL to minimize the concentration of photoproducts building up during the course of an experiment. Over the course of a TA experiment samples are monitored by steady state UV-vis spectroscopy about once an hour to ensure minimal photoproduct accumulation.

Photoacid sample preparation. Indazole-based and phenylhydroxy-based photoacids were synthesized by Prof. Yi Liao's group according to procedures published²⁷⁻³⁰ previously and generously provided for TA experiments. Solutions were prepared by sonication of solids in 2 mL dimethylsulfoxide (DMSO) for one minute, or until fully dissolved. A Fisher Scientific "Sonic Dismembrator 550" (400W) sonicator was necessary to achieve complete dissolution into the DMSO. After dissolution in DMSO, 18 mL of aqueous buffer was added to the solution. The solutions were prepared at an OD between 0.3 and 1.0 in a 1 mm flow cell for TA experiments. An 11 mM pH 7.4 phosphate buffered saline solution was used for the indazole-based photoacid³⁰. The phenylhydroxy-based photoacid can be prepared as the acidic (protonated phenylhydroxy group) or the conjugate base (deprotonated phenylhydroxy group) by controlling the pH of the buffer, since the hydroxyl group pKa is ~ 7.8 ²⁷. The acidic form of the phenylhydroxy-based photoacid was dissolved in 10 mM pH 5.5 citrate buffer to ensure $> 99\%$ acidic species. The

conjugate base of the phenylhydroxy-based photoacid was dissolved in 10 mM pH 10 carbonate buffer to ensure > 99% conjugate base species. In addition, the indazole-based photoacids and phenylhydroxy-based photoacids were prepared in pure anhydrous DMSO. Anhydrous DMSO was purchased from Sigma-Aldrich and used without further purification. All TA measurements involving the anhydrous DMSO were kept under dry nitrogen to prevent accumulation of water.

Photoacid steady state photolysis. Photolysis experiments were carried out with a 450W Osram Xe lamp. A 10 cm cuvette filled with steam-distilled water functioned as a heat filter for the lamp, and a GG375 3 mm glass filter was used to filter wavelengths shorter than 375 nm. The lamp was focused on the sample by an $f = 250$ mm fused silica lens. UV-vis spectra were collected with either a Shimadzu UV-2600 spectrometer or an Avantes 2048 spectrometer. In water, the reverse reaction, in which the spiropyran ring opens to reform merocyanine, has a half-life of ~ 76 seconds²⁷. The Avantes 2048 spectrometer is a diode array that allows for acquisition of a spectrum in ~ 10 milliseconds. The Avantes 2048 spectrometer was used to keep reversion back to merocyanine in the data to a minimum.

Hydroxo- and Aquocobalamin sample preparation. The pKa of hydroxocobalamin (HOCbl) is eight³¹. In order to study HOCbl, 11 mM pH 10.5 carbonate buffer was used as the solvent to ensure > 99% of the sample was the deprotonated hydroxocobalamin species. In order to study aquocobalamin (H₂OCbl), 11 mM pH 5.5 phosphate buffer was used as the solvent to ensure > 99% of the sample was the protonated H₂OCbl species. In the case of steady state photolysis experiments, five molar equivalents of sodium benzoate were dissolved in the HOCbl or H₂OCbl solutions to function as a hydroxyl radical scavenger. Also, it is critical to degas the solvents with nitrogen to keep the samples anaerobic over the course of the steady state photolysis experiments. In the case of TA experiments, no radical scavenger or degassing is required.

Hydroxo- and Aquocobalamin steady state photolysis. Samples were prepared at ~ 0.2 mM and kept in a sealed and stoppered 1 mm quartz cuvette (NSG™). Multiple light sources were employed to investigate the wavelength dependence of photolysis. The 532 nm output of a YAG laser, the 253 nm line of an Hg calibration lamp, the entire spectrum of a 450 W Xe arc lamp, and a 13 mm pyrex window (≤ 290 nm cutoff) in the Xe lamp were used in photolysis experiments³². UV-vis spectra were collected at regular intervals of the photolysis experiment to measure the progress of photolysis. Photolysis experiments utilizing un-filtered UV light sources took ~ 30 minutes to go to completion, whereas experiments using filtered UV light to determine the “turn on” wavelength took ~ 12 hours owing to the low intensities of effective photons.

TA measurements of HOCbl and H₂OCbl relied on higher concentrations. Concentrations were chosen to give an optical density between 0.3 – 1.0 at the pump wavelength in either a 1 mm quartz flow cell or a ~ 0.3 mm wire guided flow. In the case of 404 nm pump experiments, the concentrations were ~ 0.5 mM (0.7 mg/mL), and carried out in a flow cell. In the case of 269 nm pump experiments, the concentrations were ~ 0.2 mM (0.3 mg/mL), and also carried out in a flow cell. In the case of pump wavelengths from 540 – 560 nm experiments, the concentrations were ~ 2.0 mM (3 mg/mL), and carried out in the wire guided flow.

Notes to Chapter 2

- (1) Moulton, P. F. *Proc. IEEE* **1992**, *80* (3), 348–364.
- (2) Seigman, A. *Lasers*, Revised ed.; University Science Books, 1986.
- (3) Silfvast, W. T. *Laser Fundamentals*, 2nd edition; Cambridge University Press, 2008.
- (4) Backus, S.; Durfee, C. G.; Murnane, M. M.; Kapteyn, H. C. *Rev. Sci. Instrum.* **1998**, *69* (3), 1207.
- (5) Christov, I. P.; Stoev, V. D.; Murnane, M. M.; Kapteyn, H. C. *Opt. Lett.* **1996**, *21* (18), 1493–1495.
- (6) Hecht, E. *Optics*, 4th edition. Addison Wesley Publishing Company, 2001.
- (7) Perry, M. D.; Mourou, G. *Science* **1994**, *264* (1), 917–924.
- (8) Rudd, J. V.; Korn, G.; Kane, S.; Squier, J.; Mourou, G. A.; Bado, P. *Opt. Lett.* **1993**, *18* (23), 2044.
- (9) Ohmae, G.; Yagi, T.; Nanri, K.; Fujioka, T. *Japanese J. Appl. Physics, Part I Regul. Pap. Short Notes Rev. Pap.* **2000**, *39* (10), 5864–5869.
- (10) Backus, S.; Peatross, J.; Huang, C. P.; Murnane, M. M.; Kapteyn, H. C. *Opt. Lett.* **1995**, *20* (19), 2000–2002.
- (11) Megerle, U.; Pugliesi, I.; Schrieffer, C.; Sailer, C. F.; Riedle, E. *Appl. Phys. B* **2009**, *96* (2–3), 215–231.
- (12) Boyd, R. W. *Nonlinear Optics*, 3rd ed.; Academic Press, 2008.
- (13) Cerullo, G.; Silvestri de, S.; De Silvestri, S. *Rev. Sci. Instrum.* **2003**, *74* (1), 1–18.
- (14) Manzoni, C.; Polli, D.; Cerullo, G. *Rev. Sci. Instrum.* **2006**, *77* (2), 23103.
- (15) Smith, B. D.; Spears, K. G.; Sension, R. J. *J. Phys. Chem. A* **2016**, *120* (33), 6575–6581.
- (16) Snellenburg, J. J.; Laptanok, S. P.; Seger, R.; Mullen, K. M.; van Stokkum, I. H. M. *J. Stat. Softw.* **2012**, *49* (3).

- (17) Van Stokkum, I. H. M.; Larsen, D. S.; Van Grondelle, R. *Biochim. Biophys. Acta - Bioenerg.* **2004**, *1657* (2–3), 82–104.
- (18) Fitzpatrick A.E., Lincoln C.N., van Wilderen L.J.G.W., van T. J. J. *J. Phys. Chem. A* **2012**, *116* (3), 1077–1088.
- (19) Papagiannakis, E.; Vengris, M.; Larsen, D. S.; Van Stokkum, I. H. M.; Hiller, R. G.; Van Grondelle, R. *J. Phys. Chem. B* **2006**, *110* (1), 512–521.
- (20) Ward, C. L.; Elles, C. G. *J. Phys. Chem. Lett.* **2012**, *3* (20), 2995–3000.
- (21) Ward, C. L.; Elles, C. G. *J. Phys. Chem. A* **2014**, *118* (43), 10011–10019.
- (22) Takeda, A.; Tsubouchi, A. In *Houben-Weyl methods of molecular transformations*. Georg Thieme: Stuttgart, Germany; 2009; Vol. 47a, pp 247–325.
- (23) Mccurry, J. E. *Chem. Rev.* **1989**, *89* (0), 1513–1524.
- (24) Ter Wiel, M. K. J.; Van Delden, R. A.; Meetsma, A.; Feringa, B. L. *J. Am. Chem. Soc.* **2003**, *125* (49), 15076–15086.
- (25) Quick, M.; Berndt, F.; Dobryakov, A. L.; Ioffe, I. N.; Granovsky, A. A.; Knie, C.; Mahrwald, R.; Lenoir, D.; Ernsting, N. P.; Kovalenko, S. A. *J. Phys. Chem. B* **2014**, *118* (5), 1389–1402.
- (26) Harada, N.; Koumura, N.; Feringa, B. L. *J. Am. Chem. Soc.* **1997**, *119* (31), 7256–7264.
- (27) Shi, Z.; Peng, P.; Strohecker, D.; Liao, Y. *J. Am. Chem. Soc.* **2011**, *133* (37), 14699–14703.
- (28) Johns, V. K.; Wang, Z.; Li, X.; Liao, Y. *J. Phys. Chem. A* **2013**, *117* (49), 13101–13104.
- (29) Johns, V. K.; Peng, P.; Dejesus, J.; Wang, Z.; Liao, Y. *Chem. - A Eur. J.* **2014**, *20* (3), 689–692.
- (30) Abeyrathna, N.; Liao, Y. *J. Am. Chem. Soc.* **2015**, *137* (35), 11282–11284.
- (31) Subedi, H.; Hassanin, H. A.; Brasch, N. E. *Inorg. Chem.* **2014**, *53* (3), 1570–1577.
- (32) Wiley, T. E.; Miller, W. R.; Miller, N. A.; Sension, R. J.; Lodowski, P.; Jaworska, M.; Kozlowski, P. M. *J. Phys. Chem. Lett.* **2016**, *7* (1), 143–147.

Chapter 3

First generation molecular motor

The subject of investigation in this chapter and Chapter four is a first generation molecular motor, (E and Z)-2,2'-dimethyl-2,2',3,3'-tetrahydro-1,1'-bi(cyclopenta[*a*]naphthalenyldiene), referred to as P-trans and P-cis hence forth. This family of molecules garnered a great deal of interest in recent years for potential applications as a light driven rotary motor for molecular-scale devices¹⁻⁵. Based on the cis/trans isomerization of alkenes, the molecular motor photoisomerizes about a central carbon-carbon double bond⁶⁻¹³. The molecular motor's overcrowding substituents impart a useful property of unidirectional isomerization to the molecule¹⁴⁻¹⁸. The substituents give the molecule a ratchet-like, or sawtooth, potential energy profile to the molecule along its internal rotation coordinate¹⁹⁻²¹. Such an asymmetric potential causes unidirectional isomerization.

Synthetic research to optimize the ground state potentials for increases in the rate of rotation has been the primary focus until recently. This resulted in molecular motors with rotary rates of 3 MHz (3×10^6 1/s)^{22,23}, quite the achievement! The ultrafast photoisomerization of the molecular motor is attracting attention, since the ground state of the molecular motor is getting closer and closer to synthetic perfection²⁴⁻²⁸. Mechanistic details of the photoisomerization of the molecular motor are necessary for further optimization.

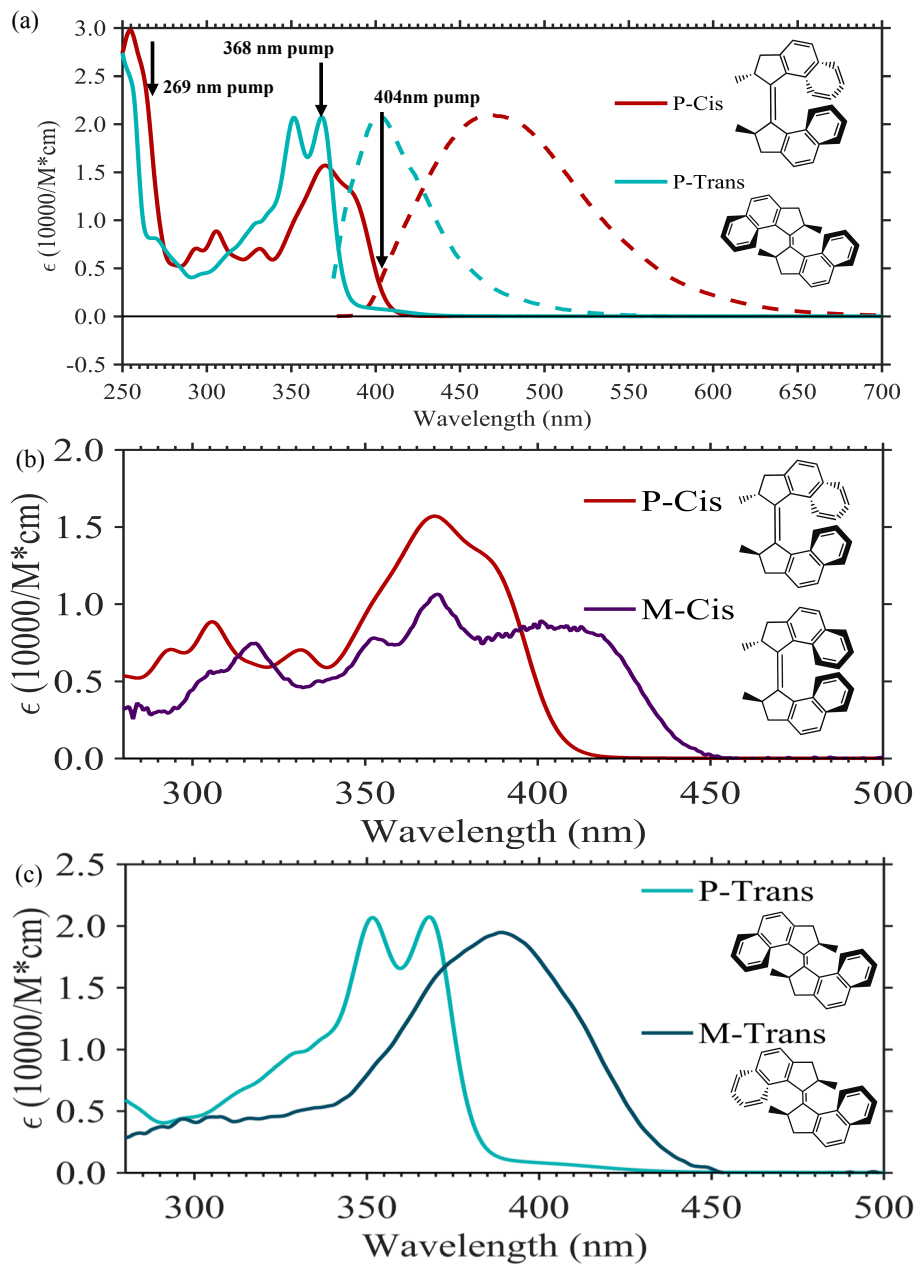


Figure 3.1. (a) Steady state UV-vis spectra of P-Cis (solid red) and P-trans (solid blue) in heptane. Normalized steady state fluorescence spectra of P-Cis (dash red) and P-trans (dash blue) in heptane. Black arrows mark the excitation wavelengths used in TA experiments. (b) Comparison of P-cis (red) and M-cis (purple) steady state UV-vis spectra. (c) Comparison of P-trans (light blue) and M-trans (dark blue) UV-vis spectra.

Ultrafast UV-vis transient absorption (UV-vis TA) spectroscopy was the primary technique employed to carry out these studies. Other supporting experiments include polarized TA, steady state UV-vis absorption, low temperature photolysis, and steady state fluorescence. The cis/trans and trans/cis photoisomerization of P-trans and P-cis, was investigated in heptane and 2-butanol with a variety of excitation wavelengths, ranging from 269, 368, and 404 nm. The majority of the studies were carried out in heptane. Density functional theory (DFT) and time dependent density functional theory (TDDFT) calculations were used to calculate ground state energies, vibrational frequencies, vertical excitation energies and activation energies²⁹⁻³¹.

The steady state UV-vis spectra and steady state fluorescence spectra of P-cis and P-trans are shown in Figure 3.1 along with the corresponding structures. M-cis and M-trans, the unstable conformers of P-cis and P-trans, are featured in Figure 3.1b and 3.1c. The TA measurements featured in this chapter were obtained with a continuum probe spanning ~ 325 – 800 nm. The probe tracks the ground state bleach (GSB), stimulated emission (SE), and visible excited state absorption (ESA) transitions.

Sample handling

The P-cis and P-trans molecular motors samples were synthesized according to methods detailed in Chapter two. Heptane and 2-butanol were obtained from Sigma-Aldrich and used without further purification. All samples were sonicated to ensure complete dissolution of the samples in solvent. All samples were prepared in the dark to prevent unintended degradation. UV-vis spectra were collected every hour over the course of TA experiments to monitor the buildup of photoproducts. TA measurements were carried out with the instrument described in Chapter two.

Table 3.1. Typical time-points and step sizes used in a TA experiment

Region of interest (ps)	Step size (ps)
-25	-
-1.0	1.0
-0.5	0.1
2.5	0.025
5.5	0.075
11	0.125
22	0.250
55	0.500
110	1.0
330	2.0
550	5.0
900	10.0

The UV-vis TA spectra of the P-cis, P-trans, and M-trans isomers are presented below. Relative polarization between the pump and probe was either maintained at 54.7° (magic angle) or adjusted to examine the anisotropy of molecules in their excited states. The time points in Table 3.1 were typically used to collect the data.

The UV-vis spectra of the metastable M-helicity conformers were collected at low temperatures to trap the unstable species. The activation barriers for thermal helix inversion of

trans and cis isomers are ~ 19 kcal/mol and ~ 22 kcal/mol, giving half-lives of about 18 seconds and 74 minutes at room temperature³². Low temperature photolysis experiments were carried out in a dry ice/isopropanol bath at -30 °C to trap the M-helicity conformers. Dry nitrogen gas was continuously flowed over the sample to prevent accumulation of ice and condensation on the cuvettes. A 400 W mercury arc lamp served as the excitation source. Spectra were collected by an Avantes 2048 diode array UV-vis.

Results

P-cis transient absorption. The UV-vis TA spectra of the P-cis isomer in heptane and 2-butanol were measured after excitation with 404 nm or 269 nm. The TA spectra in heptane are shown in Figures 3.2 and 3.3. The data are characterized by an initial excited state, an intermediate state, and production of M-trans photoproduct. Upon formation of the M-trans photoproduct, the sample reaches a steady state where the TA signal does not change for the next $\gg 1$ ns.

The GSB appears within the instrument response (IRF, ~ 300 fs) of the experiment and is centered at 370 nm. Within the IRF of the experiment, ESA from $\sim 500 - 800$ nm appears as well. In the 404 nm excitation data a SE signal from $\sim 450 - 540$ nm appears within the IRF of the experiment. This SE signal agrees with the steady state fluorescence spectrum of P-cis shown in Figure 3.1. In the 269 nm excitation data, there is no net negative SE signal in the $\sim 450 - 540$ nm region. This net positive TA signal is likely due overlapping ESA.

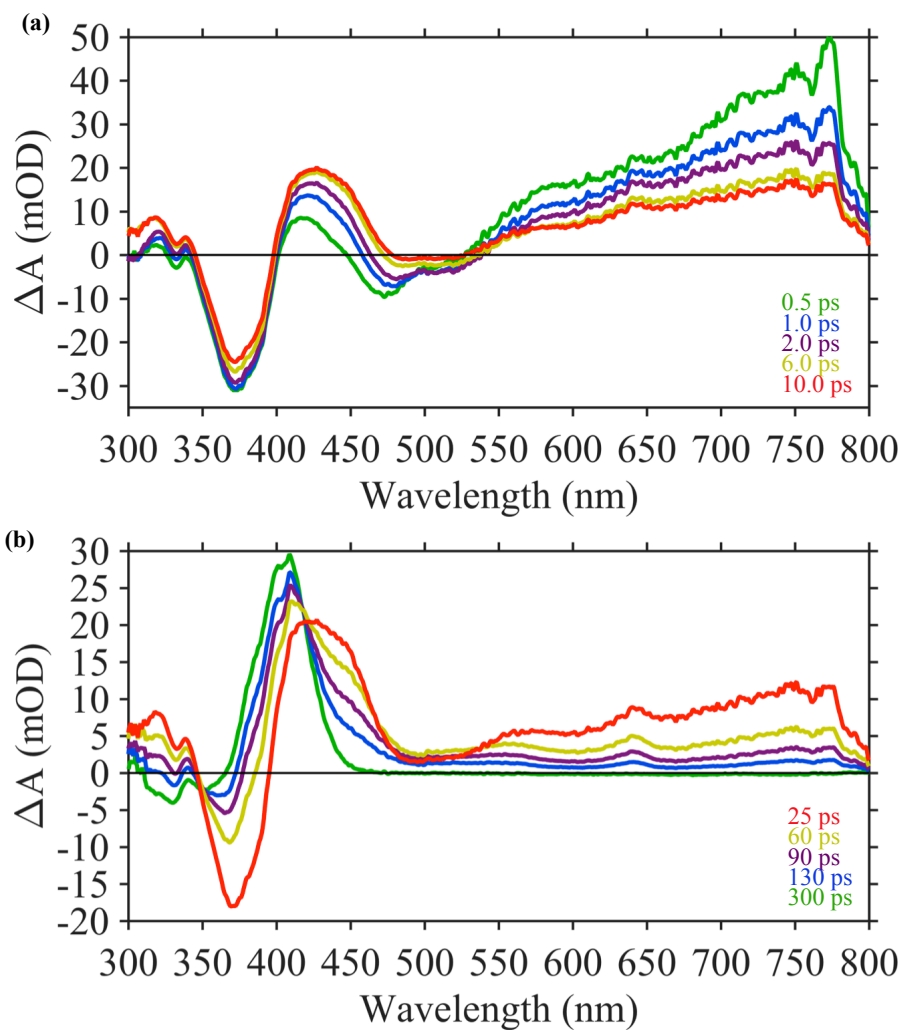


Figure 3.2. TA spectra of P-cis molecular motor excited with 404 nm. Early time spectra (a) at 0.5 ps (green), 1.0 ps (blue), 2.0 ps (purple), 6.0 ps (yellow) and 10 ps (red). Later time spectra (b) at 25 ps (red), 60 ps (yellow), 90 ps (purple), 130 ps (blue), and 300 ps (green)

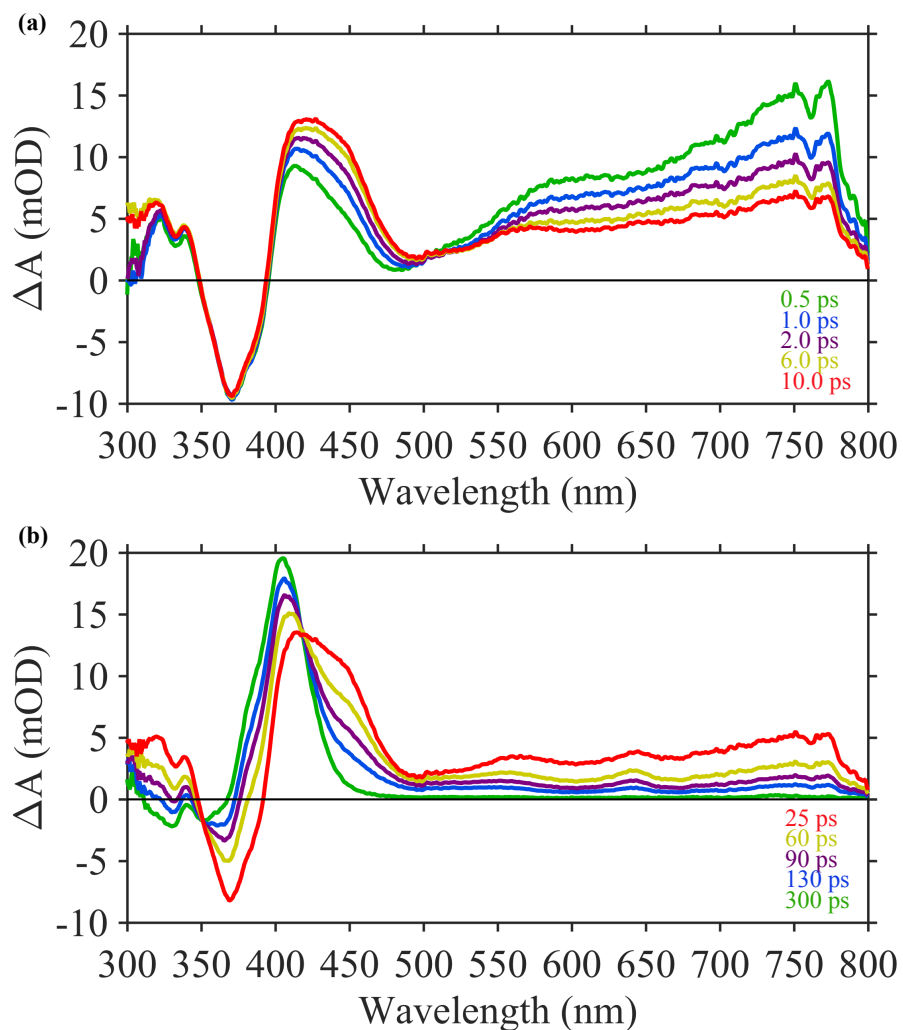


Figure 3.3. TA spectra of the P-cis molecular motor excited with 269 nm. Early time spectra (a) at 0.5 ps (green), 1.0 ps (blue), 2.0 ps (purple), 6.0 ps (yellow) and 10 ps (red). Later time spectra (b) at 25 ps (red), 60 ps (yellow), 90 ps (purple), 130 ps (blue), and 300 ps (green)

The early time ESA and SE signals decay quickly as an intermediate species grows in. The intermediate is characterized by a new ESA peak centered at ~ 425 nm. This intermediate ESA signal decays on a longer timescale than the initial species. In addition, ESA from $\sim 500 - 800$ nm decays on this longer time scale as well as shown in Figures 3.2 and 3.3. The intermediate species forms a steady state difference spectrum by 300 ps which persists for

>> 1 ns. The steady state difference spectrum is in excellent agreement with the difference between steady state UV-vis spectra of the P-cis and M-trans as shown in Figure 3.4.

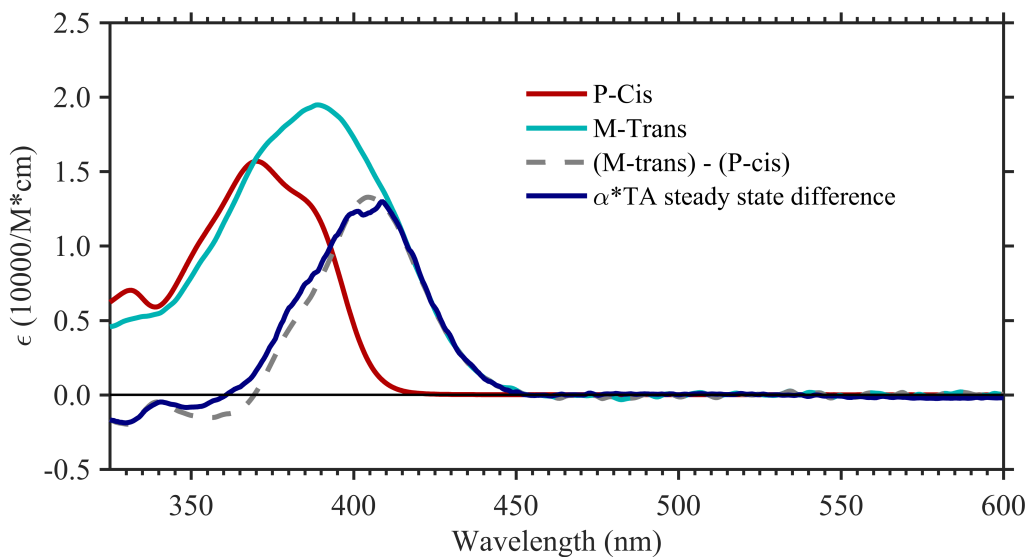


Figure 3.4. Comparison of steady state TA spectrum (dark blue) to P-cis (red), M-trans (light blue) UV-vis spectra, and the difference between M-trans and P-cis (grey dash). Steady state TA spectrum was scaled by a factor $\alpha = 43,000$.

Global analysis of P-cis data. The TA data are analyzed by globally fitting the dataset to the convolution of an IRF and a sum of exponential decays with associated amplitudes:

$$Data(\lambda, t) = IRF(t_0, fwhm) \otimes \sum_{i=1}^N A_i(\lambda) e^{-t/\tau_i}$$

Equation 3.1

where A_i are wavelength dependent amplitudes, τ_i are the time constants, and N is the number of components in the fit. The data are best fit by three exponential decays and a time independent amplitude to capture the steady difference spectrum at long times as shown in Figure 3.5. The fitting results for multiple trials of both excitation wavelength and both solvents (heptane and

2-butanol) are summarized in Table 3.2. The decay amplitudes, “Decay associated difference spectra (DADS)” obtained from the global analysis of the data are plotted in Figure 3.6.

Table 3.2. Rate constants obtained from global fits of P-cis TA data in heptane and 2-butanol, using 404 or 269 nm as pump wavelengths.

heptane experiments				
	τ_1 (ps)	τ_2 (ps)	τ_3 (ps)	τ_4 (ps)
404 nm excitation	0.53 ± 0.05	13 ± 3	71 ± 4	$\gg 1$ ns
269 nm excitation	0.85 ± 0.2	17 ± 4	71 ± 5	$\gg 1$ ns
2-butanol experiments				
	τ_1 (ps)	τ_2 (ps)	τ_3 (ps)	τ_4 (ps)
404 nm excitation	0.41 ± 0.02	4.5 ± 0.7	39 ± 0.7	$\gg 1$ ns
269 nm excitation	0.51 ± 0.2	5.4 ± 0.6	37 ± 0.7	$\gg 1$ ns

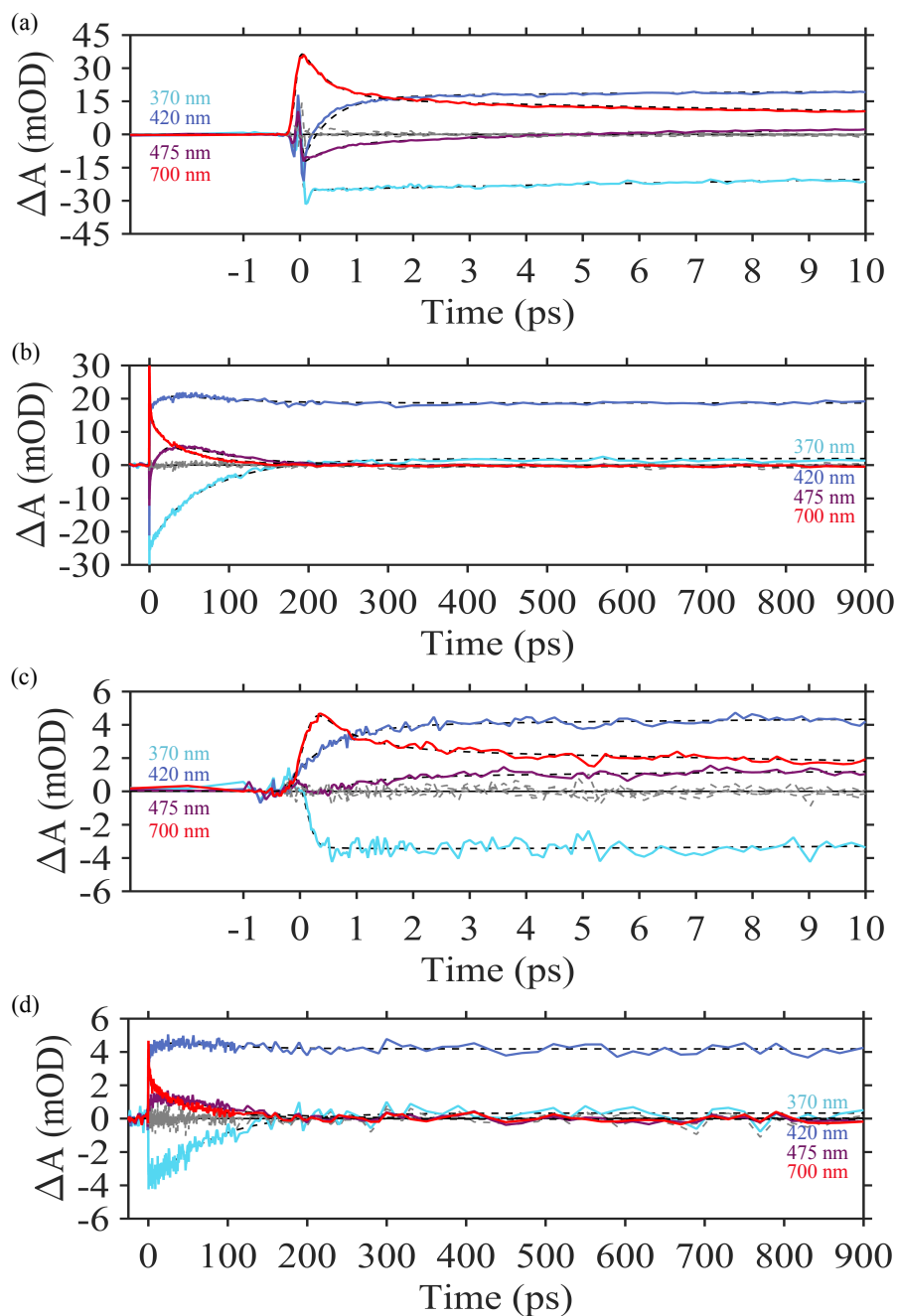


Figure 3.5. Kinetic lineouts from P-cis in heptane using either 404 nm as the pump (a and b) or 269 nm as the pump (c and d). Early times in the top panels (a and c) and late times in the bottom panels (b and d). 370 nm (light blue) tracks the GSB, 420 nm (dark blue) tracks the SE and the photoproduct, 475 nm (purple) tracks SE and the intermediate state, and 700 nm (red) tracks the early ESA.

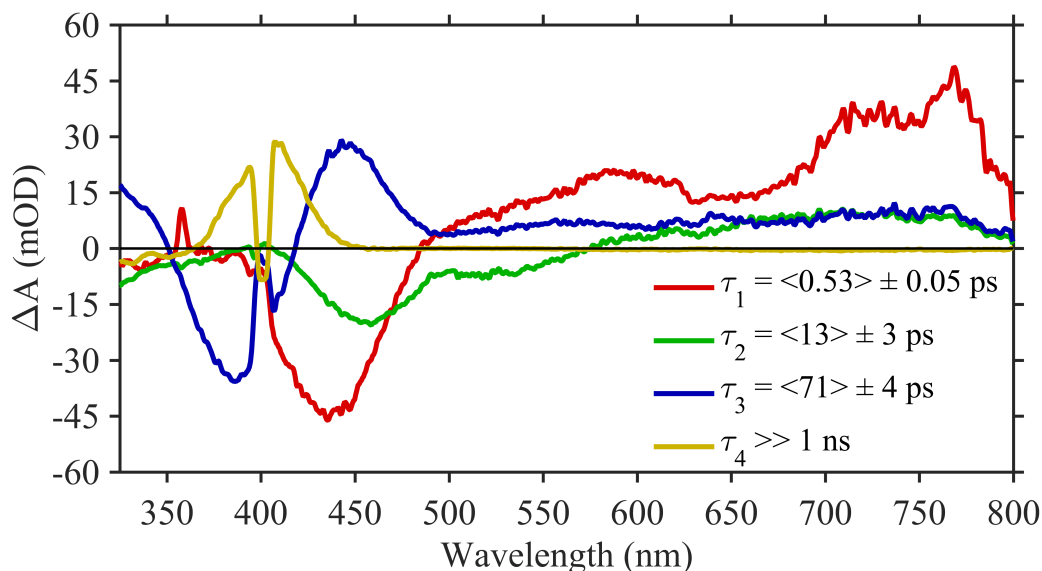


Figure 3.6. Decay associated difference spectra (DADS) of P-cis in heptane after 404 nm excitation.

DADS are the amplitudes at every wavelength of each decay term in the global fit.

P-cis transient absorption anisotropy. TA data of the P-cis in heptane were collected as a function of relative polarization between the pump and probe to examine the anisotropy of the molecule's excited states. The anisotropy signal, r , is given by the following equation:

$$r = \frac{I_{\parallel} - I_{\perp}}{I_{\parallel} - 2 * I_{\perp}}$$

Equation 3.2

Where I_{\parallel} and I_{\perp} are the ΔA signals when the pump is parallel or perpendicular to the probe. A tail-matching scale factor of 1.095 for 269 nm excitation and 1.092 for 404 nm excitation is applied to the perpendicular data in order to ensure $r(t = \infty) = 0$. The tail-matching scale factor accounts for differences between the parallel and perpendicular pump intensities resulting from reflection losses by the sample cell. The raw anisotropy data are complicated by overlapping signals coming from each species in the cascade through excited states. To simplify the data, the

parallel and perpendicular datasets were fit to the results of a global analysis of the magic angle data while holding the lifetimes constant. The amplitudes of the DADS are transformed into species associated difference spectra (SADS) assuming a sequential kinetic model ($A \rightarrow B \rightarrow C \rightarrow D$), according to the transformation procedure in Chapter two. Parallel and perpendicular SADS were constructed from the fit results and the anisotropy of each SADS was calculated by Equation 3.2 and shown in Figure 3.7.

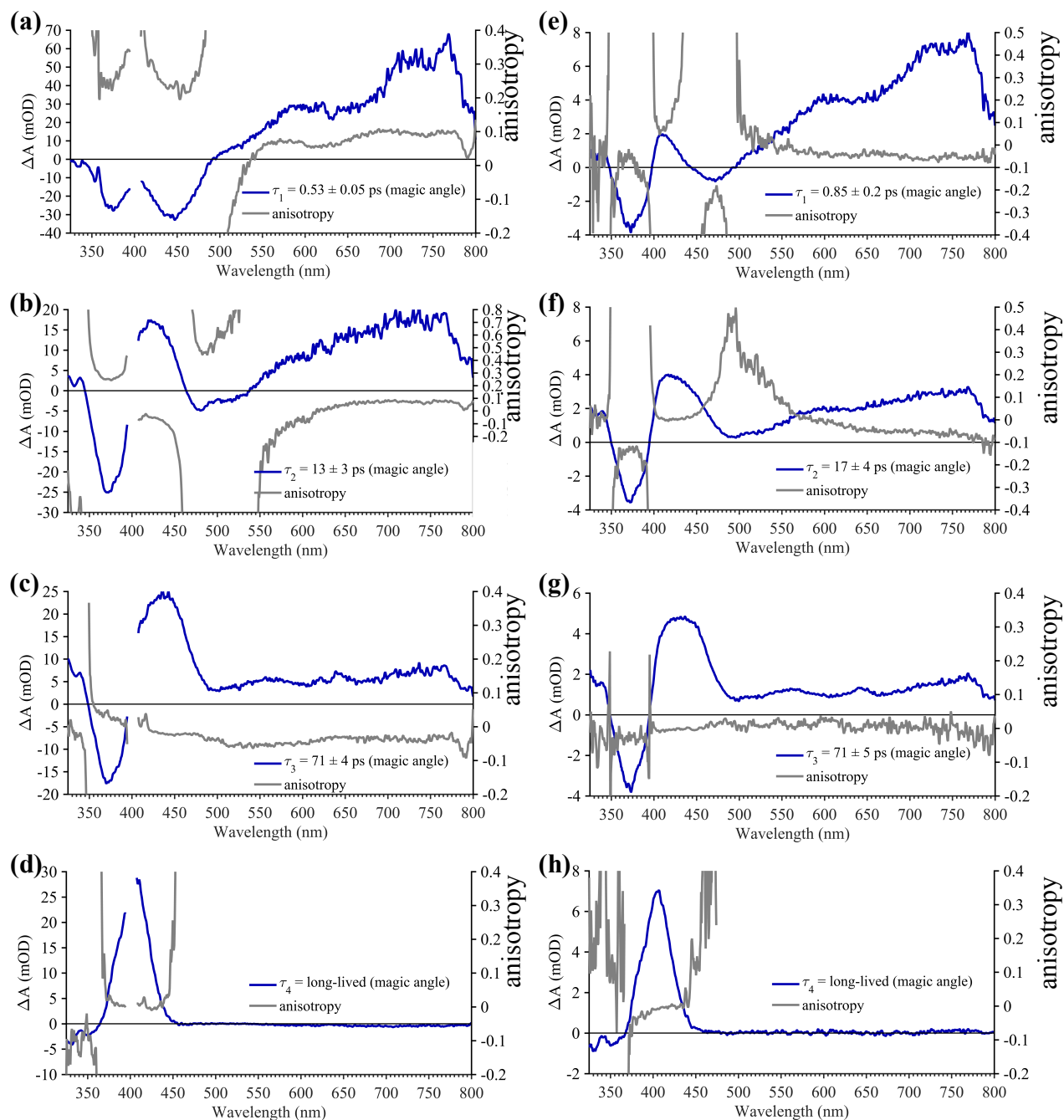


Figure 3.7. Anisotropy of P-cis in heptane SADS assuming a sequential kinetic model after excitation with 404 nm (a-d) or 269 nm (e-h).

P-trans transient absorption. The UV-vis TA of the P-trans isomer in heptane and 2-butanol was measured after excitation with 368 and 269 nm. The results in heptane are shown in

Figures 3.8 and 3.9. At early times the spectra show ESA from ~ 450 – 800 nm. This ESA decays to form intermediate ESA, which is more narrow and centered at ~ 450 nm. This intermediate ESA gives rise to the M-cis photoproduct, which is in good agreement with steady state P-trans/M-trans difference spectra. After formation of the M-cis photoproduct, the sample reaches steady a state that does not change for the remaining nanosecond of time sampled in our experiment.

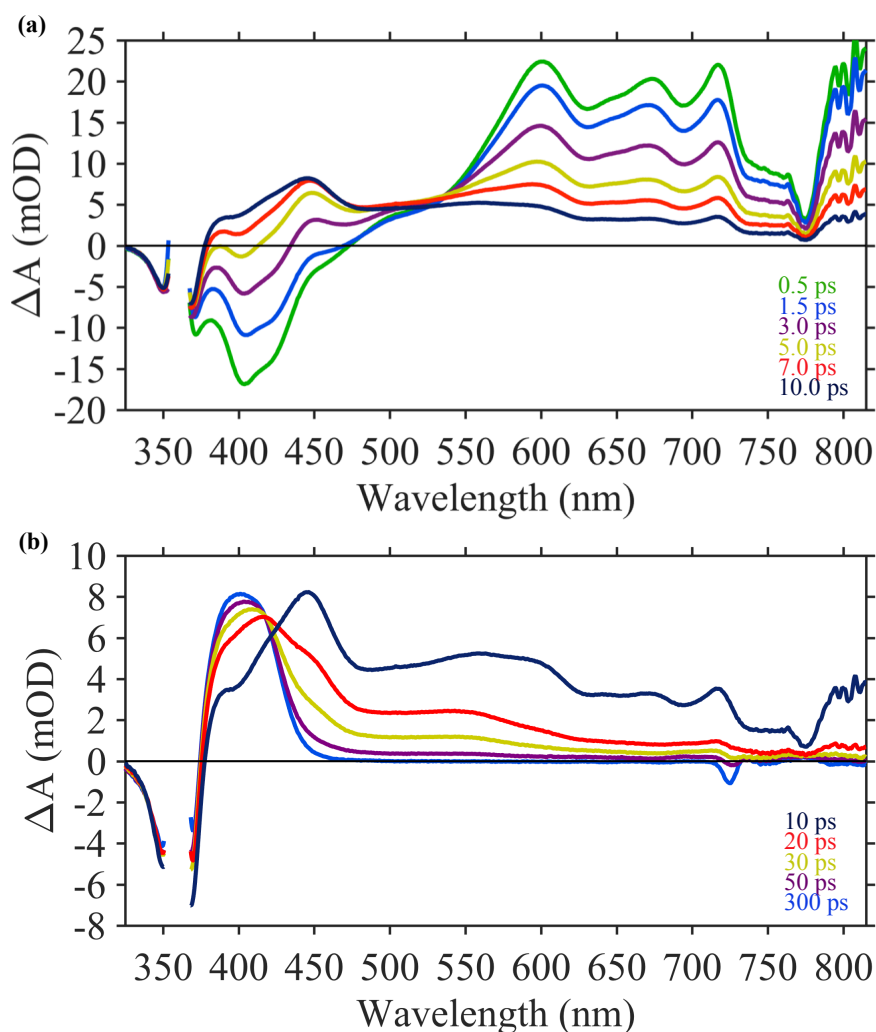


Figure 3.8. TA spectra of P-trans in heptane and excitation with 368 nm. Early times (a) 0.5 ps (green), 1.5 ps (blue), 3.0 ps (purple), 5.0 ps (yellow), 7.0 ps (red), and 10 ps (dark blue). Later times (b) 10 ps (dark blue), 20 ps (red), 30 ps (yellow), 50 ps (purple), and 300 ps (light blue).

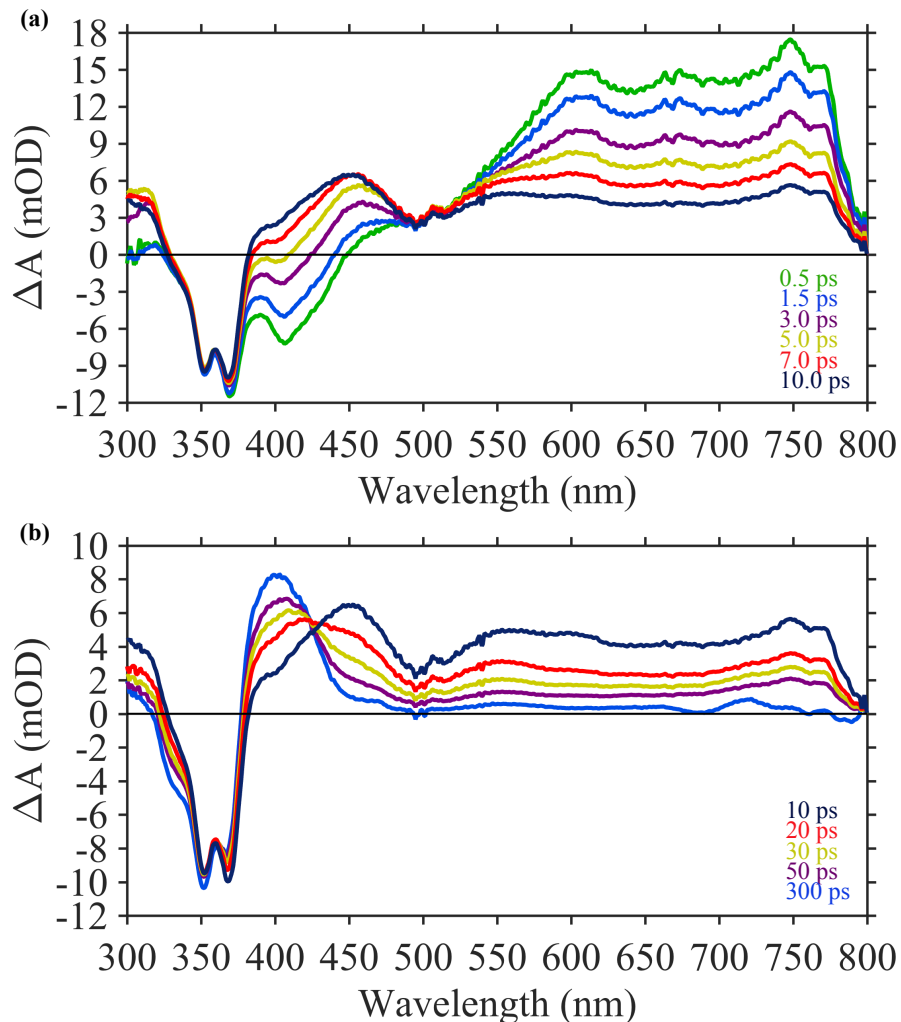


Figure 3.9. TA spectra of P-trans in heptane and excitation with 269 nm. Early times (a) 0.5 ps (green), 1.5 ps (blue), 3.0 ps (purple), 5.0 ps (yellow), 7.0 ps (red), and 10 ps (dark blue). Later times (b) 10 ps (dark blue), 20 ps (red), 30 ps (yellow), 50 ps (purple), and 300 ps (light blue).

The GSB appears within the IRF (~ 300 fs) of the experiment and is centered at 360 nm. The vibronic peaks of the UV-vis spectrum at 352 and 368 nm are easily visible in the GSB in Figure 3.9. At early times, ESA from $\sim 450 - 800$ nm appears within the IRF of the experiment. Both pump wavelengths show an SE signal from $\sim 380 - 450$ nm, which appears within the IRF of the experiment. This SE signal is in agreement with the steady state fluorescence spectrum of P-trans as shown in Figure 3.1a.

The early time ESA and SE signals decay quickly as an intermediate species grows in. The intermediate is characterized by a new ESA peak centered at ~ 450 nm. The intermediate species forms a steady state difference spectrum by 200 ps, which persists for up to a nanosecond. The steady state difference spectrum agrees with the difference between steady state UV-vis spectra of the M-trans and P-trans from $\sim 385 - 450$ nm, but does not agree in the $350 - 385$ nm region as shown in Figure 3.10. This is likely due to the presence of residual P-trans in the M-cis UV-vis spectrum as demonstrated by the P-trans vibronic peaks at 352 and 368 nm.

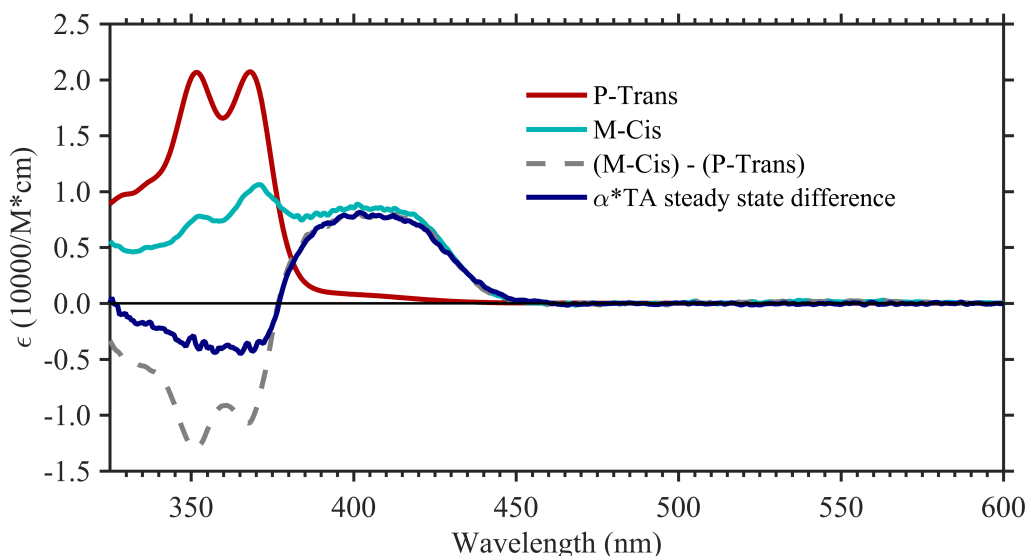


Figure 3.10. Comparison of steady state TA spectrum to P-trans and M-cis. Steady state TA spectrum was scaled by a factor $\alpha = 220,000$.

The TA data were globally fit to a sum of three exponential decays with associated amplitudes. Kinetic lineouts demonstrating the quality of the fit are shown in Figure 3.11. The fitting results for multiple trials of both excitation wavelength and both solvents (heptane and 2-butanol) are given in Table 3.3.

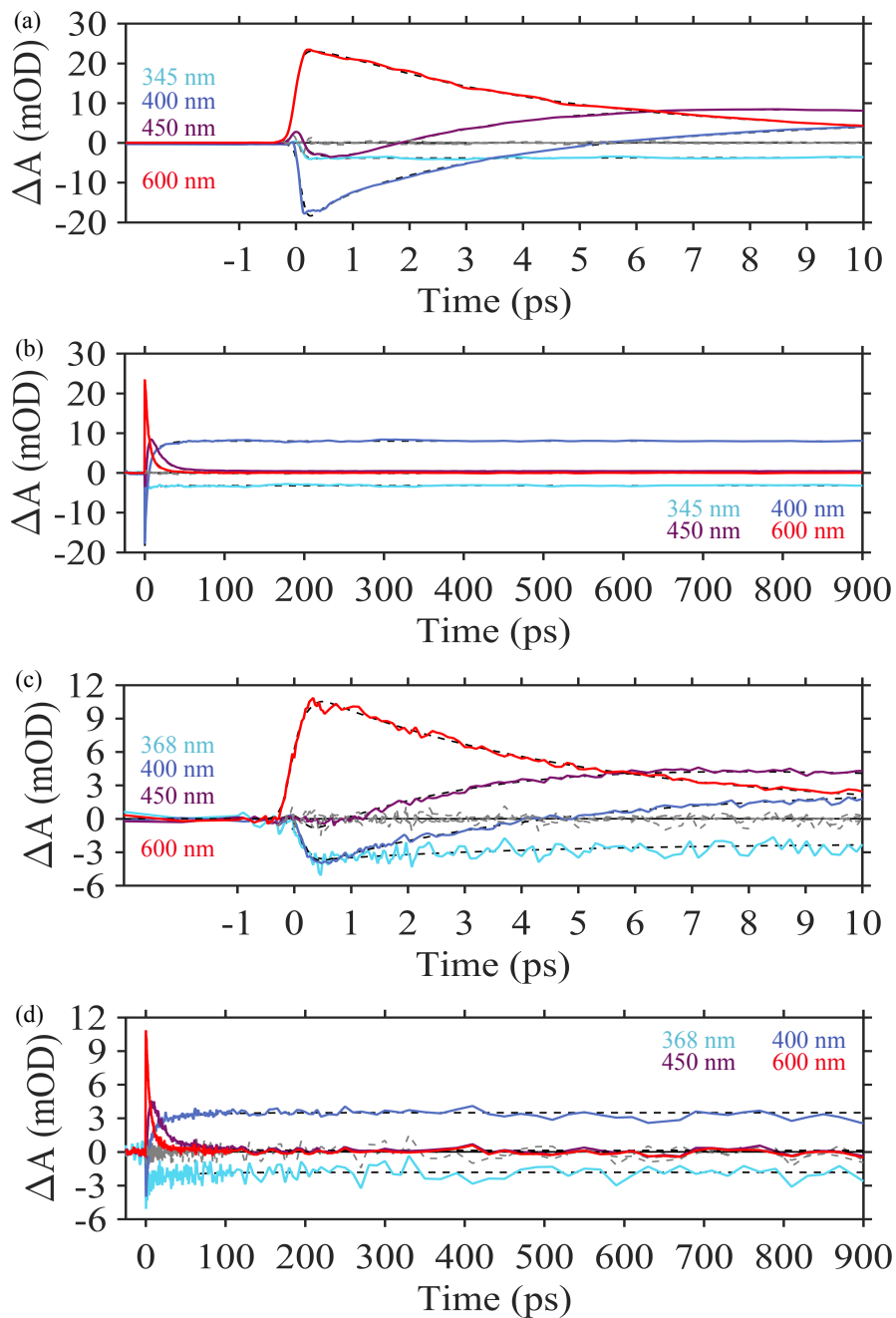


Figure 3.11. Kinetic lineouts from the P-trans in heptane TA data using either 368 nm as the pump (a and b) or 269 nm as the pump (c and d). Early times in the top panels (a and c) and late times in the bottom panels (b and d). 345 or 368 nm (light blue) tracks the GSB, 400 nm (dark blue) tracks the SE and the photoproduct, 450 nm (purple) tracks SE on and the intermediate state, and 600 nm (red) tracks the early ESA.

Table 3.3. Rate constants obtained from global fits of the P-trans TA data in heptane and 2-butanol, using either 368 or 269 nm as pump wavelengths.

heptane experiments	τ_1 (ps)	τ_2 (ps)	τ_3 (ps)	τ_4 (ps)	τ_5 (ns)
368 nm excitation	0.50	3.6	12	-	>> 1 ns
269 nm excitation	-	4.2 ± 0.2	11 ± 2	45 ± 4	>> 1 ns
2-butanol experiments	τ_1 (ps)	τ_2 (ps)	τ_3 (ps)	τ_4 (ps)	τ_5 (ns)
269 nm excitation	-	4.9 ± 0.1	12.7 ± 0.3	63 ± 2	>> 1 ns

P-trans transient absorption anisotropy. TA anisotropy data of the P-trans were collected using 368 and 269 nm excitation. In the 368 nm excitation data, a tail-matching scale factor of 1.175 is applied to the perpendicular data in order to ensure $r(t = \infty) = 0$ at long times, when the anisotropy has decayed to zero. In the 269 nm excitation data, a tail-matching scale factor of 1.215 was used.

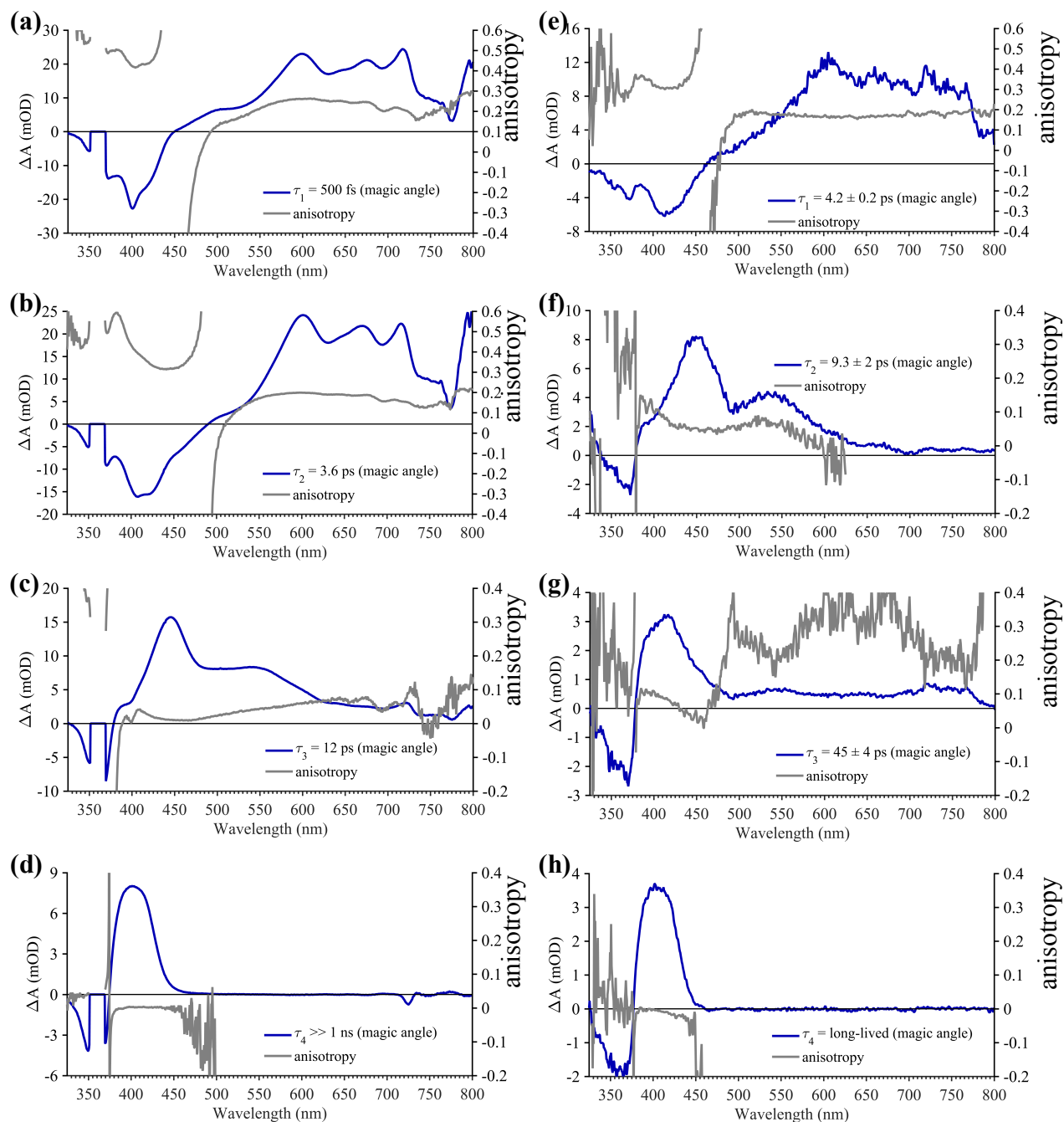


Figure 3.12. Anisotropy of P-trans in heptane SADS assuming a sequential kinetic model after excitation with 368 nm (a-d) or 269 nm (e-h).

The anisotropy signals are complicated by multiple overlapping signals. To simplify the data, the magic angle data were globally fit, and then the rates were held fixed in a fit of the parallel

and perpendicular data. The resultant DADS were transformed into SADS, assuming a sequential kinetic model, for the parallel and perpendicular data. These SADS were used to create the anisotropy of each species involved in the photochemical formation of M-cis and shown in Figure 3.12.

M-trans transient absorption. The UV-vis TA of the M-trans isomer in heptane was measured after excitation with 404 nm and shown in Figure 3.13. Samples of M-trans are prepared by dissolving P-trans in solution. The M-trans constitutes ~ 4.5% of the total concentration at room temperature. M-trans' UV-vis spectrum is red-shifted absorption with respect to P-trans such that excitation with 404 nm only excites M-trans. The data are characterized by an initial excited state, an intermediate state, and a return to the ground state with no measurable photoproduct formation. Notably, the M-trans isomer produces no photoproducts unlike the more thermodynamically stable P isomers.

The GSB is centered at 390 nm, a close match to the M-trans UV-vis as seen in Figure 3.1c. Sharp ESA centered at 645 nm and broad ESA peak from 650 – 800 nm appear within the IRF (~ 150 fs) of the experiment. An SE signal from ~ 490 – 610 nm appears within the IRF of the experiment as well.

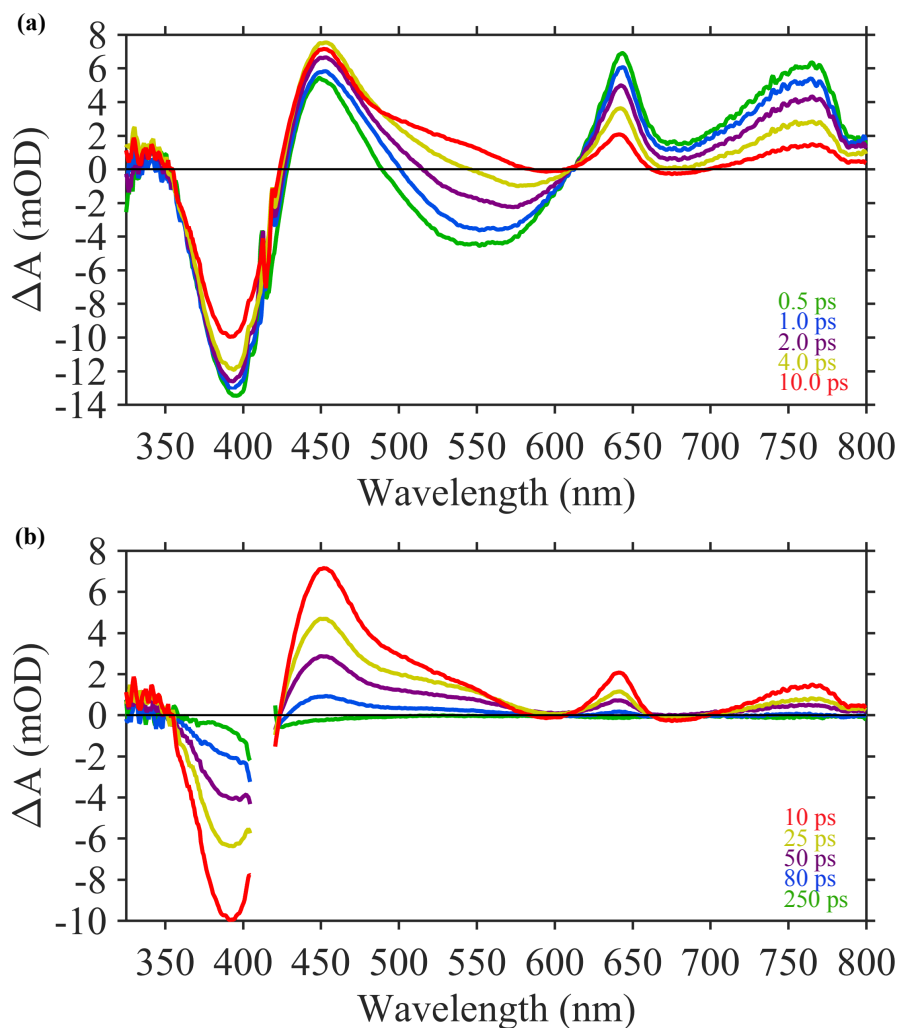


Figure 3.13. TA spectra of M-trans excited with 404 nm in heptane. (a) Early time spectra at 0.5 ps (green), 1.5 ps (blue), 2.0 ps (purple), 4.0 ps (yellow) and 10 ps (red). (b) Later time spectra at 10 ps (red), 25 ps (yellow), 50 ps (purple), 80 ps (blue), and 250 ps (green).

Table 3.4. M-trans global fitting results in heptane and 2-butanol, excitation wavelength is 404 nm

solvent	τ_1 (ps)	τ_2 (ps)
heptane	2.3 ± 0.1	40 ± 5
2-butanol	2.4 ± 0.1	20.4 ± 0.1

Global analysis of the M-trans gives two exponential decay components. A time independent component is not necessary in the fit since the M-trans isomer does not produce photoproducts. The fitting results for 404 nm excitation in heptane and 2-butanol are given in Table 3.4. Kinetic lineouts at selected wavelengths along with the fit results and residuals are shown in Figure 3.14.

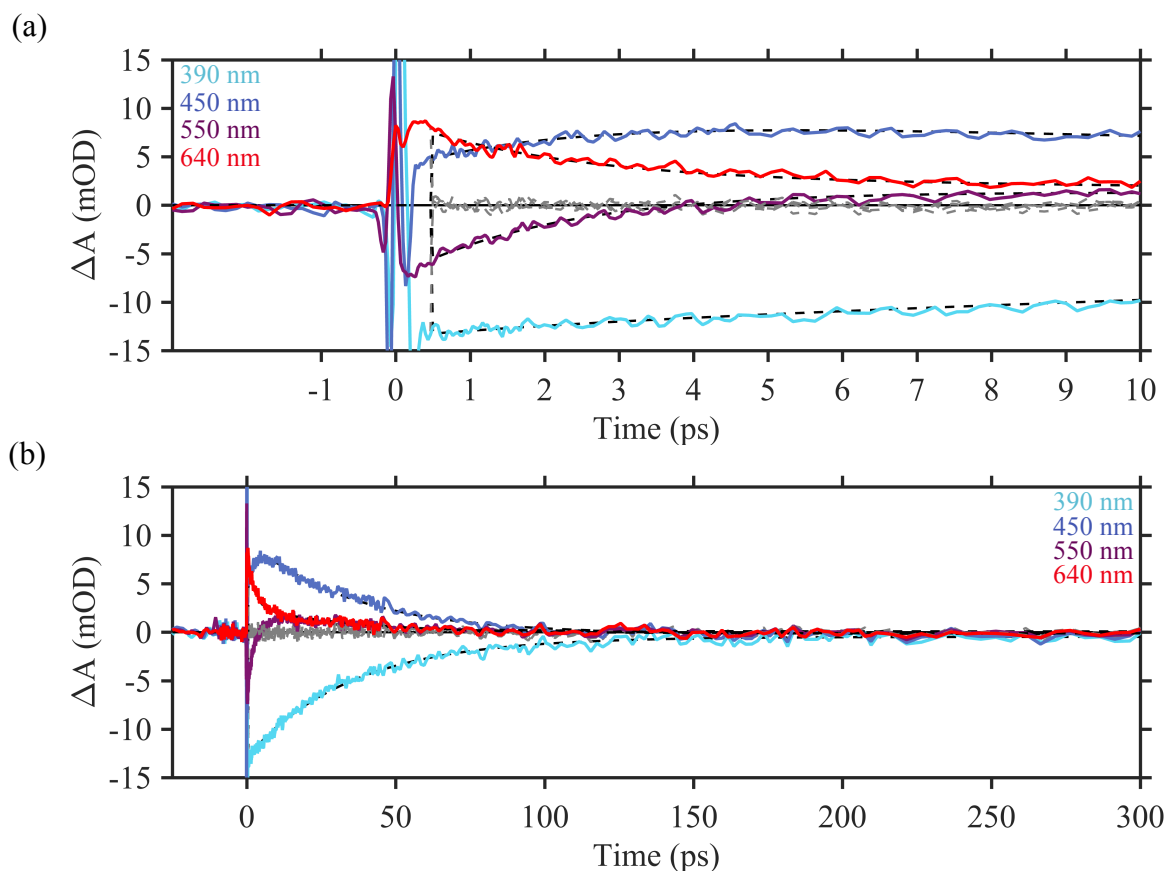


Figure 3.14. Kinetic lineouts from the M-trans in heptane TA data using 404 nm as the pump. Early times (a) and late times in the bottom panel (b). 390 nm (light blue) tracks the ground state bleach, 450 nm (dark blue) tracks the intermediate state, 550 nm (purple) tracks SE and the intermediate state, and 640 nm (red) tracks the early ESA

Density functional theory calculations. The PBE0 functional and the 6-31G** basis set were used to calculate the ground state geometries and energies of the P-cis, P-trans, M-cis, and M-trans in vacuum and in polarizable continuum models (PCM) heptane and 2-butanol. PBE0

was chosen because of its low computational cost and ability to accurately calculate energies of the A and B excited states of stilbene and stiff stilbene³⁰. Frequency calculations ensured true minimum energy geometries by inspecting for imaginary vibrational frequencies. The enthalpy and entropy of each structure were calculated in the frequencies calculations and the results are summarized in Table 3.5. The vertical excitation energies from the ground state minima of each conformer in vacuum and in PCM were calculated with Time Dependent DFT (TDDFT) and are shown in Table 3.6. The growing string method³¹ was used to search for the transition states and activation energies for thermal helix inversion between the M and P isomers shown in Table 3.7.

Table 3.5. Thermodynamic properties of all four conformations of the molecular motor. Quantities were obtained by frequency calculations in DFT, using PBE0/6-31G.**

Conformation	Enthalpy (kcal/mol)	Entropy (kcal/K*³mol)	Free energy, T=293K (kcal/mol)
P-cis	289.599	0.151006	244.5765611
M-cis	289.564	0.149492	244.9929602
P-trans	289.624	0.150478	244.7589843
M-trans	289.66	0.148996	245.2368426

Table 3.6. Vertical excitation energies of all four conformations of the molecular motor calculated using TDDFT with PBE0/6-31G** and are compared to the measured peaks in the UV-vis spectra. (*f* is the oscillator strength of the transition). Top value in each cell is calculated in vacuum, middle value is calculated with PCM in dielectric constant = 1.92 and refractive index = 1.39 (heptane) and bottom value is calculated with PCM in dielectric constant = 17.26 and refractive index = 1.40 (2-butanol).

Conformation	S_0/S_1 , (nm, <i>f</i>)	S_0/S_2 , (nm, <i>f</i>)	UV-vis
P-cis	367.1, 0.3713	345.1, 0.00004790	369 nm
	381.6, 0.2903	331.7, 0.0006853	
	382.7, 0.2853	334.1, 0.001618	
M-cis	394.3, 0.3835	328.2, 0.00003012	~400 nm
	420.0, 0.2787	349.3, 0.001495	
	416.9, 0.2726	352.8, 0.002951	
P-trans	352.0, 0.6188	316.8, 0.004492	359 nm
	365.3, 0.4796	320.8, 0.005806	
	365.3, 0.4764	321.1, 0.006005	
M-trans	385.0, 0.6676	333.7, 0.0001662	388 nm
	404.8, 0.4799	337.1, 0.00001643	
	405.3, 0.4732	337.9, 0.00001729	

Table 3.7. Activation energies for thermal helix inversion for both molecular isomers. Second column contains reported activation energies³².

Transition	Activation energy (kcal/mol)	Reported activation energy (kcal/mol)
M-cis → P-cis	32.1	22.2
M-trans → P-trans	26.4	19.1

Discussion

The goal of these TA experiments was to understand the excited state behavior of a first generation molecular motor. P-cis and P-trans cascade through multiple excited states prior to the formation of photoproducts, M-trans and M-cis. In short, the initial bright excited states internally convert to dark states, which then form photoproducts. The ground electronic state of P-trans and M-trans are in equilibrium with ~ 5% M-trans. Unlike P-trans, M-trans produces

little to no photoproducts. P-cis will also be in equilibrium with M-cis, but the percentage of M-cis is insignificant.

P-cis discussion. The photoisomerization of P-cis forming M-trans proceeds through three species with lifetimes of ~ 500 fs, ~ 13 ps and ~ 70 ps. The initial excited state relaxes on a ~ 500 fs timescale, forming a new excited state with ESA centered at 425 nm and a lifetime of ~ 13 ps. This second excited state is also a bright state because there are signatures of SE in the SADS from 460 to 535 nm shown in Figure 3.7b. In addition, parallel polarization pump/probe TA data show negative values for as long as 10 ps in Figure 3.15. This second excited state, whose spectrum is distinct from the initial state as shown in Figure 3.7a and 3.7b, produces SE since the initial excited state, whose lifetime is ~ 500 fs, has decayed to essentially zero percent population by 10 ps. The initial excited state is too short lived to account for such long-lived SE.

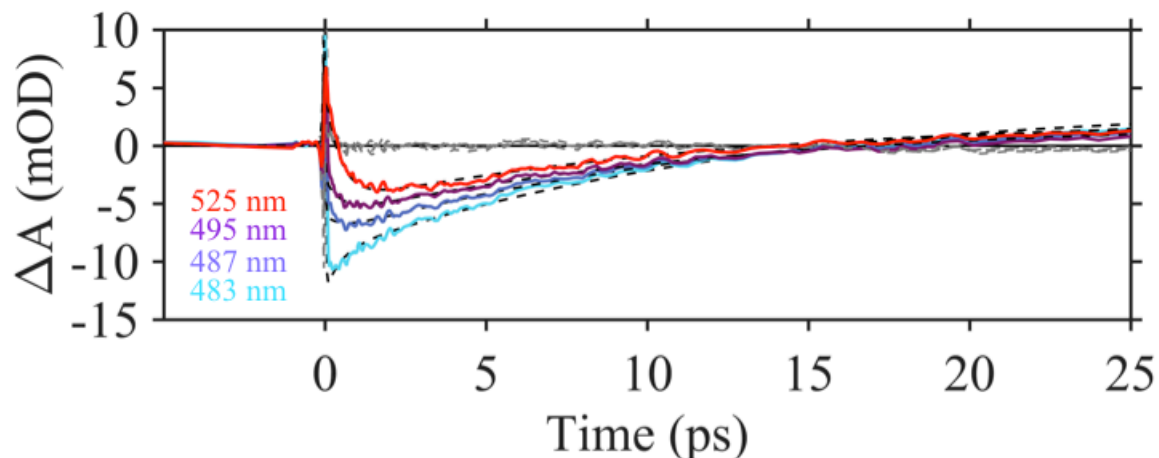


Figure 3.15. Kinetic lineouts of P-cis after being with *parallel* pump polarization 404 nm. 483 nm (light blue), 487 nm (dark blue), 495 nm (purple), 525 nm (red). SE signal continues for ≥ 10 ps.

The second excited state internally converts to a third species with a ~ 70 ps lifetime and ESA at ~ 435 nm. The signature of this species is complicated by a large amplitude, nearly flat,

positive signal across the visible spectrum, from 550 – 800 nm, similar to the P-trans data when excited with 269 nm. However, this ESA feature is likely not an background signal caused by 269 nm excitation. The DADS are large amplitude in the global fitting results, and the component is present in 269 nm and 404 nm excitation results as shown in Figures 3.6 and 3.7.

The third species forms the M-trans photoproduct on a ~ 70 ps timescale, which is stable for times much longer than the nanosecond accessed in our measurements. The TA spectrum at long times is in excellent agreement with the difference between the M-trans and P-cis steady state UV-vis spectra at -30 °C. The M-trans UV-vis spectrum acquired by low temperature photolysis contains no residual P-cis, indicating 100% conversion to M-trans by steady state photolysis. According to kinetic studies by Feringa et al.³², the barrier for thermal helix inversion is ~ 19.1 kcal/mol with a half-life of ~ 18 seconds at room temperature. The barrier deduced by the Feringa group is similar to transition state growing string calculations, 26.4 kcal/mol, as shown in Table 3.7. The M-trans UV-vis spectrum is in agreement with the low temperature photolysis spectrum published by Feringa et al.³² Finally, TDDFT calculations shown in Table 3.6 predict a red shift of ~ 20 nm for the M-trans conformer with respect to P-cis, in agreement with TA and steady state UV-vis measurements in Figure 3.4.

The pump-repump experiments in Chapter four utilize 269 nm as the pump pulse, and this choice was made out of practical concerns of signal to noise. The extinction coefficient of P-cis at 269 nm is $\sim 20,000$ 1/M*cm versus ~ 5000 1/M*cm at 404 as shown in Figure 3.1. However, the P-cis isomer's TA data excited with either 404 or 269 nm gives similar timescales and spectra.

P-trans discussion. The photoisomerization of P-trans proceeds through two species with three timescales, 500 fs, ~ 4 ps and ~ 10 ps. The initial excited state of P-trans shows SE centered at 400 nm and three ESA peaks (600, 670, and 715 nm). After excitation, relaxation from the Franck Condon region takes place on a ~ 500 fs timescale, which is demonstrated by a red-shift in the SE signal to ~ 420 nm as seen in Figure 3.12a and 3.12b. Following relaxation from the Franck-Condon region, the molecule undergoes internal conversion to a dark state on a ~ 4 ps timescale. The dark state's absorption spectrum is completely different, characterized by a sharp peak at 445 nm and a broad peak at 550 nm and no measurable SE signals. TDDFT calculations locate a low oscillator strength transition as the second lowest energy transition as shown in Table 3.6, indicating a dark state close in energy to the initial excited state. This is a common theme in polyene photochemistry supported by several experimental^{26,27,33-37} and theoretical studies^{7-9,38-40}. The lifetime of the dark state is ~ 10 ps which then forms the M-cis ground state conformer.

The steady state TA spectrum is assigned to the difference between the M-cis and P-trans conformers. TDDFT predicts a red-shift in the S_0/S_1 transition for M-cis relative to P-trans of ~ 20 nm as shown in Table 3.6. The TA signal only partially agrees with the difference between the P-trans and M-cis molecules' UV-vis spectra as shown in Figure 3.10. This is likely due to a photostationary state between P-trans and M-cis forming in steady state photolysis. M-cis is probably photoactive, and this will be tested in Chapter four with pump-repump TA.

The M-cis ground state conformer undergoes no further changes over the nanosecond measured in our experiment. Work by Feringa et al.^{23,32} indicates the M-cis conformer undergoes thermal helix inversion to form the P-cis conformer on a 74 minute timescale at room temperature in hexane, deducing a barrier of ~ 22.2 kcal/mol. Calculations of the thermal helix

inversion barrier to be 32.1 kcal/mol using the growing string method³¹ get reasonably close to Feringa et al.'s experimental measurement as shown in Table 3.7. It is also in agreement with the experimental observation that the barrier between M-cis and P-cis is larger than the barrier between M-trans and P-trans.

Much of the TA data on P-trans was collected using 269 nm as the excitation wavelength. Assuming Kasha's Rule holds⁴¹, excitation with 269 nm produces a higher energy excited state, which converts to the lower energy excited states, likely faster than the IRF (~ 300 fs) of our experiment. This wavelength was chosen out of practical purposes, since 368 nm is not achievable by the equipment available in the lab. However, there are only minor differences between the 269 nm excitation data and the 368 nm excitation data. First of all, the 500 fs lifetime measured in the 368 nm data cannot be resolved in the 269 nm data due to low signal to noise ratio and an insufficient IRF (~ 300 fs). The ~ 4 ps and ~ 10 ps SADS in each data set are similar as seen in Figures 3.8, 3.9, and 3.12. There is an additional 45 ps timescale in the 269 nm excitation data, which is not present in the 368 nm excitation data. This component is essentially featureless with small amplitude in the DADS as shown in Figure 3.16. It is likely to be a solvent signal or a minor ionization signal of the sample, which in either case plays a minor role in the dynamics of the data. Overall, exciting P-trans with 269 nm or 368 nm leads to the same cascade of excited electronic states to form M-cis.

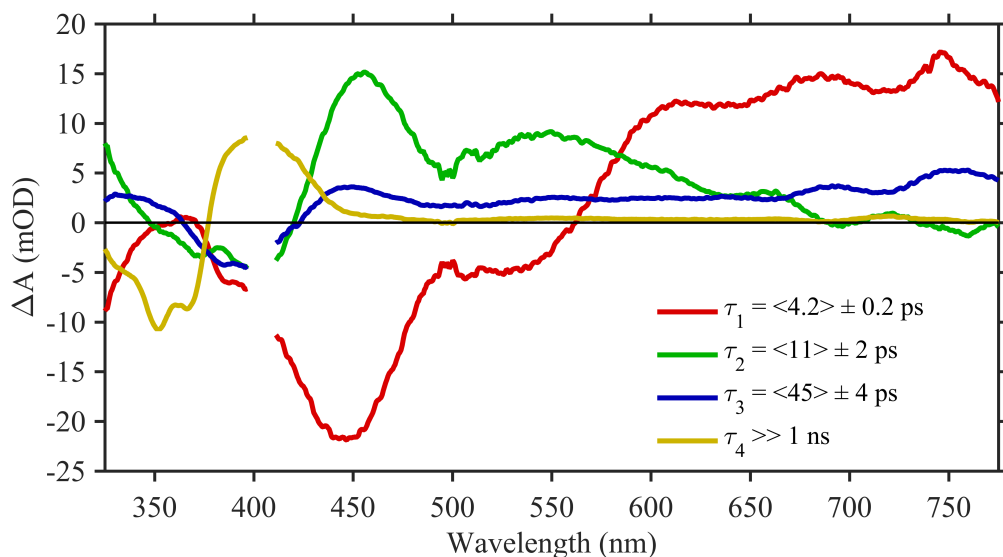


Figure 3.16. Decay associated difference spectra of P-trans dissolved in heptane and excited with 269 nm. Note the broad featureless amplitude associated with the 45 ps component. This is likely an artifact of using 269 nm, either coming from the solvent or multi-photon ionization of the sample.

M-trans discussion. The P-trans/M-trans free energy difference is small enough to allow a small population of M-trans at room temperature in solution. Calculation of the free energies obtained from DFT in vacuum and PCM, assign $\sim 70\%$ P-trans and 30% M-trans. This is an overestimate, UV-vis data suggest a $\sim 4.5\%$ M-trans present in solution at equilibrium as shown in Figure 3.17. The M-trans conformer's UV-vis absorption spectrum is ~ 20 nm red shifted with respect to the P-trans conformer's spectrum. This is observed in previously published work^{23,32}, our low temperature steady state photolysis data in Figure 3.1b, and TDDFT calculations as shown in Table 3.6. In addition, distinct steady state fluorescence spectra result if trans solutions are excited by 405 nm versus 370 nm as shown in Figures 3.1a and 3.18. The red shifted absorption of M-trans conformer ensures 404 nm pump/probe experiments only target the M-trans conformer.

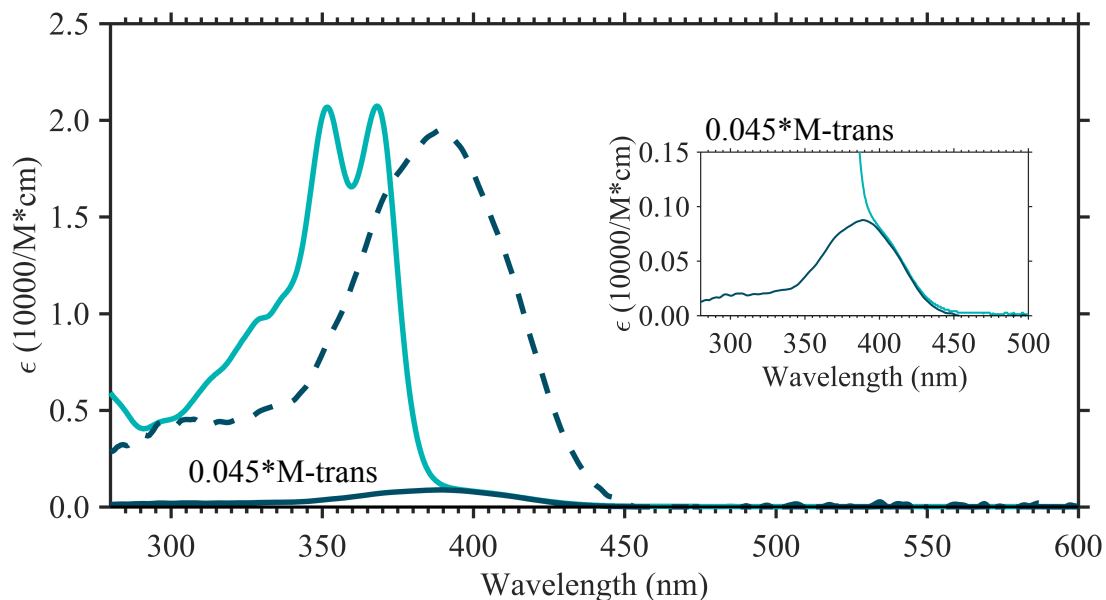


Figure 3.17. UV-vis spectra of P-trans (light blue), M-trans (dark blue dash), and 4.5% M-trans (dark blue). (Inset) Zooming in demonstrates the agreement between the shoulder of the P-trans (light blue) and the scaled amount of M-trans (dark blue).

The TA spectra and dynamics of the M-trans conformer are distinct from the P-trans conformer. The dynamics are characterized by two timescales, ~ 2 ps and ~ 40 ps and no measureable photoproduct formation. The initial excited state is a bright state with SE in agreement with the steady state fluorescence spectrum excited at 405 nm as shown in Figure 3.18. The GSB is in the same location at the peak of the steady UV-vis spectrum of M-trans as well. The initial ESA at ~ 645 nm appears to be sharp due to the overlapping profile of the SE. The initially excited bright state decays on a ~ 2 ps timescale to form a secondary excited state with no SE and a lifetime of ~ 40 ps. This excited state decays to the ground state M-trans isomer and displays no further change within our time window.

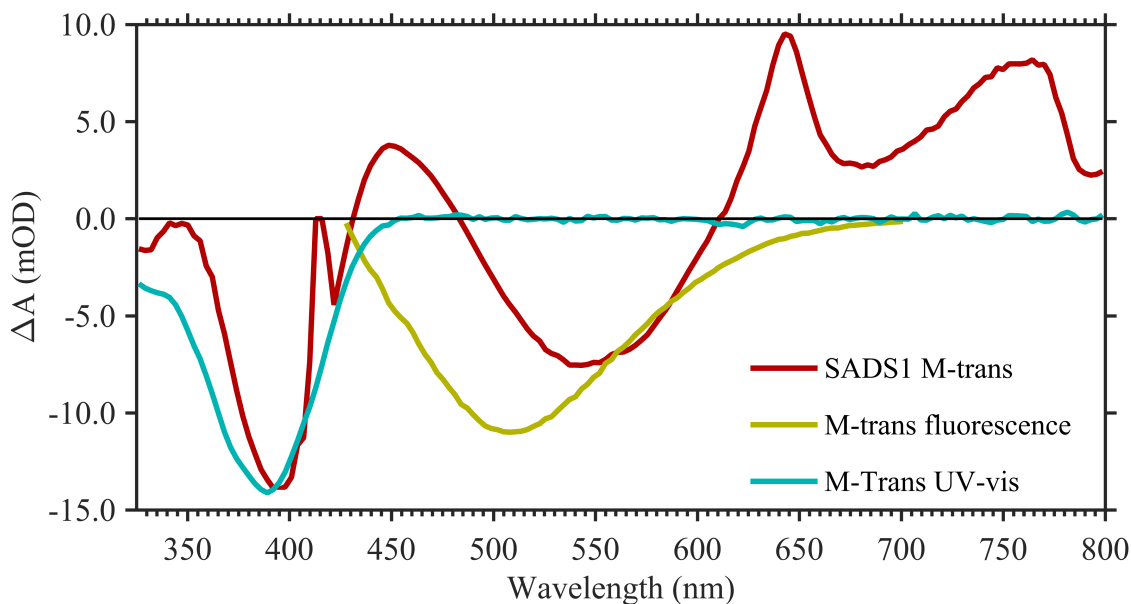


Figure 3.18. Comparison of M-trans UV-vis (teal blue), and M-trans steady state fluorescence excited by 405 nm (yellow), to the first SADS spectrum (red) from a global analysis of TA data on M-trans.

Conclusions

P-cis and P-trans isomers of the molecular motor go through two electronic states to form M-trans or P-cis, respectively. Whether excited with 269 or 404 nm, P-cis shows three timescales in the formation of M-trans: ~ 800 fs, ~ 15 ps, and ~ 70 ps. The initial excited species shows stimulated emission and broad excited state absorption. Stimulated emission from 480 – 530 nm from P-cis is observed for as long as 10 ps, indicating the second species is also a bright state. The third species is a dark state which forms M-trans on a ~ 70 ps timescale. M-trans shows no further changes for at least a nanosecond, which is supported by measured half-life of ~ 18 seconds^{22,23,32}. In the case of P-trans, excitation with 368 nm gives three timescales in the formation of M-cis: ~ 500 fs, ~ 4 ps, and ~ 12 ps. The initial excited state relaxes from the Franck-Condon region on a 500 fs timescale, and then internally converts to a dark state on a 4 ps timescale. The dark state decays to form M-cis on a 12 ps timescale. No further changes to

the M-cis product are observed for the next nanosecond. Again, this is expected based on the ~ 70 minute half-life of M-cis measured by Feringa et al.^{22,23,32} Minor differences are observed after 269 nm excitation of P-trans. For one, no ~ 500 fs component is observed because the IRF and signal to noise are unable to resolve that component. The 269 nm has ~ 4 ps and ~ 12 ps components in common with 368 nm excitation as shown in Figure 3.12. However, 269 nm excitation gives a low amplitude ~ 45 ps component not observed in 368 nm excitation.

P-trans appears to be in equilibrium with a small percentage of M-trans in solution. This is demonstrated by the excitation dependence of steady state fluorescence spectra as well as the unique transient absorption results when exciting P-trans solutions with 404 nm. The distinctive features in the M-trans data prove useful in analysis of the pump-repump data to be described in the Chapter four. These preliminary TA studies lay the groundwork for the pump-repump and pump-dump experiments in Chapter four.

Notes on Chapter 3

- (1) Chiang, P. T.; Mielke, J.; Godoy, J.; Guerrero, J. M.; Alemany, L. B.; Villagómez, C. J.; Saywell, A.; Grill, L.; Tour, J. M. *ACS Nano* **2012**, *6* (1), 592–597.
- (2) Chu, P. L. E.; Wang, L. Y.; Khatua, S.; Kolomeisky, A. B.; Link, S.; Tour, J. M. *ACS Nano* **2013**, *7* (1), 35–41.
- (3) Garcia-Lopez, V.; Chiang, P. T.; Chen, F.; Ruan, G.; Martin, A. A.; Kolomeisky, A. B.; Wang, G.; Tour, J. M. *Nano Lett.* **2015**, *15* (12), 8229–8239.
- (4) Garcia-Lopez, V.; Jeffet, J.; Kuwahara, S.; Martin, A. A.; Ebenstein, Y.; Tour, J. M. *Org. Lett.* **2016**, *18* (10), 2343–2346.
- (5) Saywell, A.; Bakker, A.; Mielke, J.; Kumagai, T.; Wolf, M.; García-López, V.; Chiang, P. T.; Tour, J. M.; Grill, L. *ACS Nano* **2016**, *10* (12), 10945–10952.
- (6) Repinec, S. T.; Sension, R. J.; Szarka, A. Z.; Hochstrasser, R. M. *J. Phys. Chem.* **1991**, *95* (8), 10380–10385.
- (7) Levine, B. G.; Martínez, T. J. *Annu. Rev. Phys. Chem.* **2007**, *58*, 613–634.
- (8) Liu, F.; Morokuma, K. *J. Am. Chem. Soc.* **2012**, *134* (10), 4864–4876.
- (9) Li, Y.; Liu, F.; Wang, B.; Su, Q.; Wang, W.; Morokuma, K. *J. Chem. Phys.* **2016**, *145* (24), 244311.
- (10) Kazaryan, A.; Filatov, M. *J. Phys. Chem. A* **2009**, *113* (43), 11630–11634.
- (11) Kazaryan, A.; Kistemaker, J. C. M.; Schäfer, L. V.; Browne, W. R.; Feringa, B. L.; Filatov, M. *J. Phys. Chem. A* **2010**, *114* (15), 5058–5067.
- (12) Kazaryan, A.; Lan, Z.; Schäfer, L. V.; Thiel, W.; Filatov, M. *J. Chem. Theory Comput.* **2011**, *7* (7), 2189–2199.
- (13) Filatov, M.; Olivucci, M. *J. Org. Chem.* **2014**, *79* (8), 3587–3600.
- (14) Koumura, N.; Geertsema, E. M.; Meetsma, A.; Feringa, B. L. *J. Am. Chem. Soc.* **2000**, *122* (48), 12005–12006.

- (15) Feringa, B. L. *J. Org. Chem.* **2007**, *72* (18), 6635–6652.
- (16) Lubbe, A. S.; Ruangsupapichat, N.; Caroli, G.; Feringa, B. L. *J. Org. Chem.* **2011**, *76* (21), 8599–8610.
- (17) Vicario, J.; Meetsma, A.; Feringa, B. L. *Chem. Commun.* **2005**, *116* (47), 5910–5912.
- (18) Browne, W. R.; Feringa, B. L. *Nat. Nanotechnol.* **2006**, *1* (1), 25–35.
- (19) Astumian, R.; Bier, M. *Phys. Rev. Lett.* **1994**, *72* (11), 1766–1769.
- (20) Astumian, R. D. *Science.* **1997**, *276* (5314), 917–922.
- (21) Astumian, R. D. *Nat. Nanotechnol.* **2012**, *7* (11), 684–688.
- (22) Klok, M.; Boyle, N.; Pryce, M. T.; Meetsma, A.; Browne, W. R.; Feringa, B. L. *J. Am. Chem. Soc.* **2008**, *130* (32), 10484–10485.
- (23) Klok, M.; Browne, W. R.; Feringa, B. L. *Phys. Chem. Chem. Phys.* **2009**, *11* (40), 9124–9131.
- (24) Augulis, R.; Klok, M.; Feringa, B. L.; Van Loosdrecht, P. H. M. *Phys. Status Solidi Curr. Top. Solid State Phys.* **2009**, *6* (1), 181–184.
- (25) Conyard, J.; Addison, K.; Heisler, I.; Cnossen, A.; Browne, W. R.; Feringa, B. L.; Meech, S. R. *Nat. Chem.* **2012**, *4* (7), 547–551.
- (26) Conyard, J.; Cnossen, A.; Browne, W. R.; Feringa, B. L.; Meech, S. R. *J. Am. Chem. Soc.* **2014**, *136* (27), 9692–9700.
- (27) Amirjalayer, S.; Cnossen, A.; Browne, W. R.; Feringa, B. L.; Buma, W. J.; Woutersen, S. *J. Phys. Chem. A* **2016**, *120* (43), 8606–8612.
- (28) Conyard, J.; Stacko, P.; Chen, J.; McDonagh, S.; Hall, C. R.; Laptinok, S. P.; Browne, W. R.; Feringa, B. L.; Meech, S. R. *J. Phys. Chem. A* **2017**, *121* (10), 2138–2150.
- (29) Jacquemin, D.; Perpte, E. A.; Scuseria, G. E.; Ciofini, I.; Adamo, C. *J. Chem. Theory Comput.* **2008**, *4* (1), 123–135.
- (30) Angeli, C.; Improta, R.; Santoro, F. *J. Chem. Phys.* **2009**, *130* (17).
- (31) Zimmerman, P. *J. Chem. Theory Comput.* **2013**, *9*, 3043–3050.
- (32) Ter Wiel, M. K. J.; Van Delden, R. A.; Meetsma, A.; Feringa, B. L. *J. Am. Chem. Soc.* **2003**, *125* (49), 15076–15086.

- (33) Pang, X.; Cui, X.; Hu, D.; Jiang, C.; Zhao, D.; Lan, Z.; Li, F. *J. Phys. Chem. A* **2017**, *121* (6), 1240–1249.
- (34) Quick, M.; Berndt, F.; Dobryakov, A. L.; Ioffe, I. N.; Granovsky, A. A.; Knie, C.; Mahrwald, R.; Lenoir, D.; Ernsting, N. P.; Kovalenko, S. A. *J. Phys. Chem. B* **2014**, *118* (5), 1389–1402.
- (35) Fuß, W.; Lochbrunner, S.; Müller, A. M.; Schikarski, T.; Schmid, W. E.; Trushin, S. A. *Chem. Phys.* **1998**, *232* (1–2), 161–174.
- (36) Anderson, N. A.; Pullen, S. H.; Walker II, L. A.; Shiang, J. J.; Sension, R. J. *J. Phys. Chem. A* **1998**, *102* (52), 10588–10598.
- (37) Fuß, W.; Kosmidis, C.; Schmid, W. E.; Trushin, S. A. *Angew. Chemie - Int. Ed.* **2004**, *43* (32), 4178–4182.
- (38) Quenneville, J.; Martinez, T. J. *J. Phys. Chem. A* **2003**, *107* (6), 829–837.
- (39) Yarkony, D. R. *J. Phys. Chem. A* **2001**, *105* (26), 6277–6293.
- (40) Yarkony, D. R. *Rev. Mod. Phys.* **1996**, *68* (4), 985–1013.
- (41) Kasha, B. Y. M. *Discuss. Faraday Soc.* **1950**, *9*, 14–19.